A TENSED PATHWAY TO VESICLE CLUSTERING

BY

ANTHONY FAN

DISSERTATION

Submitted in partial fulfillment of the requirements
for the degree of Doctor of Philosophy in Mechanical Engineering
in the Graduate College of the
University of Illinois at Urbana-Champaign, 2018

Urbana, Illinois

Doctoral Committee:

Professor Taher Saif, Chair and Director of Research
Professor Rhanor Gillette
Professor Gabriel Popescu
Assistant Professor Gabriel Juarez

Abstract

Synaptic vesicles play a central role in the functionality and adaptability of the nervous system. They carry inside them molecules called neurotransmitters which allow information to be transmitted from one neuron to another cell. This transmission process can only happen if the vesicles are tightly clustered at the cell junctions, known as synapses, such that a supply of neurotransmitters can be maintained.

The mechanism of vesicle clustering had always been considered as mainly biochemistry driven. About a decade ago, newer evidence surprisingly demonstrated that mechanical tension can influence vesicle clustering as well. However, what allowed tension to influence clustering was not understood, and will be explored in this dissertation.

The first part of this work explores whether neurons maintain internal tension, and identifies the origin of the tension generators. The existence of internal tension generators allows neurons to regulate their tension state independent of their surrounding tissues, providing a potential pathway for neuronal tension to regulate clustering. Towards this goal, we inhibited multiple proteins in *in vivo drosophila* motor neurons and subsequently studied their contractility in both the axial and circumferential directions. Contractility was hampered in both directions when either F-actin or myosin motors were inhibited, revealing that there exist internal tension generators that consist of acto-myosin machinery. Our results also showed that this acto-myosin driven contractility is coupled in the axial and circumferential direction, pointing to a misaligned network architecture of the tension generators.

The second part describes 2 new enabling methods. The first method is a microfluidic setup that allows partial perfusion of an insuspendable tissue sample. Preexisting partial treatment methodologies can only be applied to suspendable samples. By extending this capability to insuspendable samples, I would be able to perform partial treatment on *in vivo drosophila* neurons to study neuronal tension. The second method was developed to support the assembly process of the microfluidic setup, which relies on natural adhesion

between a soft polymeric material and a stiff substrate. This method uses the delamination induced by a trapped bead at the soft-stiff interface to quantify the adhesion energy at the interface. Both methodologies were verified by experimental results.

The final part of this work attempts to explain the relationship between tension and vesicle clustering. By disrupting the tension generators (myosin motors) identified in the first part, I observed the declustering of vesicles after the disassembly of F-actin. I further used the microfluidic device described in the second part to demonstrate that a partial inhibition led to the same result. The microfluidic experiments isolated the treatment region from the synapse such that myosin motors disruption would only hamper neuronal tension but nothing else. It also showed that tension was generated in series along the entire length of the neuron; any failure along the length would lead to a total tension loss. I further accounted for the dynamics of vesicle clustering and declustering by photobleaching the fluorescence proteins fused to the vesicles and subsequently observing the recovery due to other vesicles migrating into the bleached area. Based on all of these experimental observations and results, it appears that F-actin and myosin motors form an in-series network along the neuron to generate tension. This tension is responsible for sustaining the F-actin network at the synapse. The synaptic F-actin is then able to serve as a scaffold for vesicles, such that vesicles can stay clustered. This pathway allows tension to influence, and potentially regulate, vesicle clustering.

To my parents and grandparents.

Acknowledgments

First and foremost, I would like to thank my family for their endless love. They have encouraged me to follow my own curiosity in my pursuit of meaning in life. They made sacrifices, so that I do not have to; I am forever indebted to them. I wish I have made them—especially my grandmothers in heaven, who passed away respectively when I was in graduate school—proud, although I know that they would have loved me unconditionally regardless.

My labmates and friends are some of the most inspiring people I know. Graduate school was, for the most part, a lone journey. But because of their unassuming kindness and support, I rarely felt lonely. I will forever cherish our memories in Chicago, Hong Kong, Smoky Mountain, Mammoth Cave, Grand Canyon, Yellowstone, various conferences, and of course in Champaign-Urbana and in the Saif Lab.

I had the pleasure to mentor 8 extremely bright undergraduate students, funded by ISUR, MUSE, and other programs meticulously ran by Tasha, Rhonda, and their colleagues. Mentoring students was truly one of the special experiences in graduate school. I hope I have not failed my students miserably, and I am proud to have produced publishable work with some of them. I wish them success and happiness. Most of all, I hope, regardless of their pursuit, they stay forever curious about the world that we live in.

Being mentored is arguably the most significant part of graduate school. I would like to thank these world-class mentors of mine in no particular order for their expertise and guidance: my doctoral committee members, Prof. Gillette, Prof. Popescu, and Prof. Juarez, and their students; Prof. Hilgenfeldt and his students and collaborators; Prof. Llano and his students; Prof. Spatz and his postdoctoral researchers, Andrew and Jennifer in MPI; MechSE staffs Kathy, Jeff, Robbie, and others; MRL Staffs, Zhiyu, Kathy, Julio, and others; IGB Staffs, Austin, Kingsley, Shiv, and others.

Most importantly, I must thank my advisor, Prof. Saif. Thank you for tolerating my inadequacy, for your role in our achievements together, and for giving freedom and guidance in my research. You have shown me what it takes to do independent research in the ways you ask broadly, think critically, and work diligently. Not only that, you have also shown by example how to be a good son, husband, and father. Thank you for being my role model.

There are many people to thank, and my words and memory might fail me in appropriately addressing them. So I will end this in the most general way possible: the mentors and friends that I have met in these 5 years of graduate schools are some of the most important people in my life. Thank you all for your patience and wisdom.

Table of Contents

Chapter 1

Introduction

1.1   Background

In multi-cellular multi-organ animals, it is essential to have a system to coordinate the activities of different parts of the body. The nervous system serves this purpose by facilitating internal communications. Many different cell types work together to allow the diverse functionality of the nervous system [1]. Among them, cells called neurons specialize in transmitting signals and information. They adopt a polarized shape by making branches—dendrites to receive signal and axons to send signal. To further propagate the signal, axons form connections with other cells or dendrites of other neurons; the connections are known as synapses. A synapse can be broadly categorized into 3 sections, the presynaptic terminal (part of the axon), the synaptic cleft (the gap between the communicating cells), and the postsynaptic terminal (part of the target cell). The signal transmitted by axons is an electrical signal called action potential, which initiates at the beginning segment of the axon conduit and terminates at the synapse. When an action potential arrives at the synapse, it triggers the release of neurotransmitters. Neurotransmitters move across the synaptic cleft and interact with the target cell. Information is thus transmitted.

These neurotransmitters are packed inside lipid bilayer vesicles. Neurotransmitter molecules are released when the vesicles fused with the axon membrane at the synaptic cleft. To facilitate neurotransmission, especially in long axons, a mechanism is needed to accumulate vesicles at the presynaptic terminal—diffusion is simply too slow and cannot keep up with the amount of vesicles needed during frequent stimulation. Yet, simply accumulating them would lead to a constant dispersion driven by brownian motion. They need something that they can stay attached to to remain clustered.

Previous work has shown that mechanical tension, among other physical and chemical processes, plays an important role in sustaining vesicle clustering [2]. The exact mechanism of how tension and vesicle clustering—two seemingly unrelated processes—are related is the main subject of interest in this dissertation.

To achieve that, I will first establish that axons do indeed maintain a tension intrinsically, demonstrating that there exists a molecular pathways which a neuron can use to regulate axonal tension, and eventually the degree of vesicle clustering. Further studying the organization of the tension generators would reveal how tension could be regulated. Next, enabling devices that make some of our experiments possible will be described and discussed. With the enabling devices explained, I will then describe the experiments performed and the obtained results. Finally, I will conclude with a mechanistic model illustrating the pathway which tension uses to influence vesicle clustering.

1.2 Organization of the dissertation

This dissertation can be broadly categorized into 3 themes, with each theme containing 2 chapters. The first theme explore the origin of tension in axons. I will provide evidence that shows that actin cytoskeleton and myosin motors are essential in generating axonal tension. I will further show that this tension has a component in the axial direction (chapter 2), and a component in the circumferential direction (chapter 3). The 2 components are likely coupled (chapter 3).

The second theme describes 2 enabling methods. Chapter 4 is dedicated to a microfluidic method that allows the selective perfusion of a portion of a tissue sample. The method allows a single axon to be perfused partially. It is used in the studies described in chapter 6 & 7, which aim to explore the role and nature of axonal tension. Chapter 5 is dedicated to a method that quantifies adhesion energy at the interface between a soft material sample and a stiff substrate, such as that in our microfluidic setup. I will describe the thoery, simulations, and experiments performed to develop and verify this method.

The third theme contains a chapter (chapter 6) exploring a potential role of axonal tension in regulating a biological phenomenon known as vesicle clustering. Vesicle clustering is an important process in neural communication and learning and memory. I will provide evidence demonstrating that tension from actin and myosin can influence the density of vesicles at where the clustering happens. Our results also point to a model that can integrate mechanical tension into our understanding of vesicle clustering.

The third theme also contains a chapter (chapter 7) in exploring the nature of the tension generators: are they in series or in parallel? Our results point to an in-series model where actin and myosin interleave to

form a network along the axon. This model explain both the observed axial-circumferential coupling shown in chapter 3, and the total tension loss under partial tension inhibition shown in this chapter.

I will end the dissertation by discussing the key take-aways. I will also discuss some possible future avenues that will allow us to understand more about the role and nature of tension/force in the nervous system.

Chapter 2

The origin of axial axonal tension

This chapter is adapted from a previous publication[1].

2.1   Motivation

Numerous studies have shown that neurites actively respond to tensile forces by growing. Bray [3] demonstrated that neurites grow in length when towed at a controlled rate. Similarly, Pfister et al. [4] showed that axons are able to elongate to a thousand times of their original length when simply subjected to a mechanical tension. The elongated axons retain their electrophysiological functions [5]. These results are not surprising given the fact that neurites are coupled to the peripheral system, which can sometimes grow at a rapid rate (about 3.45 cm per day in the case of blue whale [6]) during early development. Recent experiments have shown that unperturbed neurons are also tensed (rest tension > 0) *in vitro* [7] and *in vivo* [2], further supporting the stretch-growth theory.

Neurons also actively regulate and maintain their rest tension [8]. For instance, chick sensory neurons subjected to slackening undergo shortening and restore their tension, in most cases to a level greater than the initial value within 60-90 min [9]. Similar behaviors are observed in chick forebrain neurites but to a lesser degree [10]. Likewise, contractile behavior is observed in axons that are previously subjected to a fairly large sustained strain. For example, upon removal of external forces, stretch-grown dorsal root ganglion neurons in rat pups contract at rates up to 6.1 μm/sec and a rest tension is slowly restored within 20 min [11]. We have also previously observed that *Drosophila* axons actively maintain a rest tension of 1-13nN and axons that are made slackened become taut and restore a rest tension of similar magnitude in 10-30 minutes [12]. Contraction is also observed in neurites that are surgically severed. Earlier, Shaw et al. [13] described how isolated axon segments *in vitro* often shorten after they are resected. A number of *in vitro* studies have also demonstrated similar shortening behavior of axons upon surgical incision

---

[14, 15, 16]. These results suggest that maintaining an intrinsic tension is an integral part of neural activities.

One study suggests that vesicle clustering in the presynaptic terminal of neuromuscular junctions in embryonic *Drosophila* is dependent on mechanical tension in the axons [2]. Clustering decreases upon surgically severing the axon (intrinsic tension is compromised), but clustering is restored upon simply restoring the tension by stretching the severed axon. Further stretching the axon increase clustering by as much as 200% in 30 minutes [2]. In addition, it has also been shown that mechanical tension modulates local and global vesicle dynamics in *Drosophila* neurons [17]; and that acute brain slices "remember" the previously prescribed mechanical stretch and respond by showing hyperexcitability [18].

In this study we address the question: what is the origin of tension in motor neuron axons? A surgically cleaned single-axon system in *Drosophila* enables us to simply bring the neuromuscular junctions closer to the central nervous system (CNS). Typically, in the absence of any drug, the axons shorten, become taut, and regain tension. This cycle of slackening and straightening can be repeated multiple times, resulting axons to shorten up to 40% of their original length in some embryos. The magnitude and rate of shortening are used as measures of contractility. We find that contractility decreases dramatically after myosin II knockdown and inhibition, and in the presence of actin disrupting drugs. The rate of contractility however is faster when microtubules are disrupted. These observations suggest that the mechanical tension in *Drosophila* motor neurons is primarily generated by the acto-myosin machinery.

2.2   Materials & Methods

Culture and Dissection of *Drosophila* embryos

Transgenic Drosophila (elav0-GAL4,UAS-gap::GFP) expressing green fluorescent protein (GFP) in neuronal membranes were used for the experiments. These flies were also crossed with homozygous UAS-zipRNAi flies (37480; Bloomington Stock Center, Bloomington, IN) to knockdown zipper in neurons [19]. Repo-GAL4 and UAS-mCD8::GFP flies (7415 & 32184; Bloomington Stock Center) were crossed to visualize glial membrane. Drosophila was cultured on standard grape agar plates at room temperature (23 °C). For harvesting, the embryos were dechorionated with a 50/50 bleach and water solution for 2 minutes and then rinsed with deionized water [20]. Embryos of stage 15–16—identified by gut morphology, CNS condensation, and time elapsed after egg laying—were placed on a double-sided tape attached to a glass cover slide. They were then incubated under insect saline solution before being devitellinized. The embryos were oriented such that

the ventral nerve cord was closest to the glass surface, and a glass dissection needle was used to make a dorsal incision. The dissection was made from posterior to anterior along the embryo to remove the guts and lay the body walls down flat. Then the axons of the aCC motor neuron and the RP2 motor neuron, which comprise the intersegmental nerve, were isolated by gently removing other nearby sensory and motor neurons as well as fat cells and muscle fibers around them. The neuromuscular junctions (NMJs) of the aCC and RP2 neurons were not damaged during this process. In some cases, the axon of the RP2 neurons was also excised, leaving only the axon of the aCC neuron intact. In most cases, both axons were intact and we measured their combined response. Glass microneedles were fabricated using a Sutter Instruments (Novota, CA) laser-based micropipette/fiber puller.

Micromanipulator and Imaging

Actuation of the microneedle (Fig. 2.1A) was powered and controlled by an x-y-z piezo-actuator (NanoPZ PZC200; Newport, Irvine, CA). Live imaging of the axon under the applied deformation was carried out on an inverted microscope (IX81; Olympus, Nashua, NH). An Andor Neo sCMOS camera cooled to -30 °C was used to record images (Andor Technology, Belfast, UK) at 2 frames/second. Imaging parameters (e.g., light intensity, exposure time, gain, etc.) were kept constant during all experiments.

Axon compression and contraction measurement

In order to relax the axonal shaft, a microneedle tip was gently placed on the tissue embedding the NMJs (Fig. 2.1A). The tissue was then pushed towards the central nervous system (CNS) by 10-15% of initial axon length. We traced the profile of the axon (Fig. 2.1C) by getting the intensity centroid along the x-axis for every position of y:

$$C(y) = \sum_{x=x_{min}}^{x_{max}} xI[x,y] / \sum_{x=x_{min}}^{x_{max}} I[x,y] \tag{2.1}$$

The obtained C in Eq. 1 was then smoothed by its moving average over one-tenth of its total length. Path length was obtained by summing the euclidean distances between each point after smoothing. The symbols used for measuring axon contraction are listed in Table 2.1.

Drug Treatments

Drugs used include 2Deoxyglucose and Sodium Azide for ATP depletion [21], ML-7 to inhibit myosin light chain kinase MLCK [14], Y-27632 to inhibit myosin rho kinase ROCK [22], Latrunculin A [23, 24] and

Table 2.1: List of symbols in the axon compression experiment.

L_0	Measured arc length of axon from point a to b (Fig. 2.1B) immediately after push.
L_f	Measured arc length of axon from point a to b 5 minutes after push.
L_s	Straight-line distance between point a and b: ideal length of taut axon.
C_r	Contraction factor $\frac{\Delta L_f}{\Delta L_0} = \frac{L_0 - L_f}{L_0 - L_s}$ represents normalized magnitude of axonal contraction.
τ	Time constant of axonal contraction by assuming a first-order decay.
ΔT	The time interval between each compression cycle.

Cytochalasin D [25] for disruption of actin filaments, Nocodazole and Colchicine to disrupt microtubules [26]; all stocks from Sigma-Aldrich (St. Louis, MO). DMSO (4-X; ATCC, Manassas, VA) was used as a solvent, tested to have no observable effect at low concentration. All drugs were diluted in Ca^{2+}/Mg^{2+}–free PBS.

Immunofluorescence Staining

The prepared embryos were fixed with 4% formaldehyde (28908; Fisher Scientific, Rockford, IL) for 15 minutes; permeabilized with 0.5% Triton X-100 (X100; Sigma-Aldrich, St. Louis, MO) for 10 minutes; blocked in 5% Bovine Serum Albumin (A9647; Sigma-Aldrich, St. Louis, MO) for 10 minutes; conjugated with mouse anti-α-tubulin (1:100; A11126; Fisher Scientific, Rockford, IL) or mouse anti-repo (1:20; 8D12; DSHB, Iowa City, IA) for 60 minutes; tagged with Alexa 568 goat anti-mouse (1:200; A-11004; Fisher Scientific, Rockford, IL) for 30 minutes; and imaged with a scanning confocal microscope (LSM700; Carl Zeiss, Peabody, MA) afterwards. Samples were rinsed with PBST (PBS–0.1% Triton X-100) after each step. All steps were performed at room temperature. A brief extraction step was added before fixation in a portion of microtubules staining experiments to distinguish polymerized microtubules from the soluble tubulin pool. Permeabilization was skipped in these instances.

2.3 Results

Axons have robust contraction ability upon sustained loss of tension

We investigate 1) whether embryonic *Drosophila* axons are capable of generating contractile force after they undergo mechanically induced loss of tension, and 2) the dynamics of such contraction due to multiple successive compression cycles.
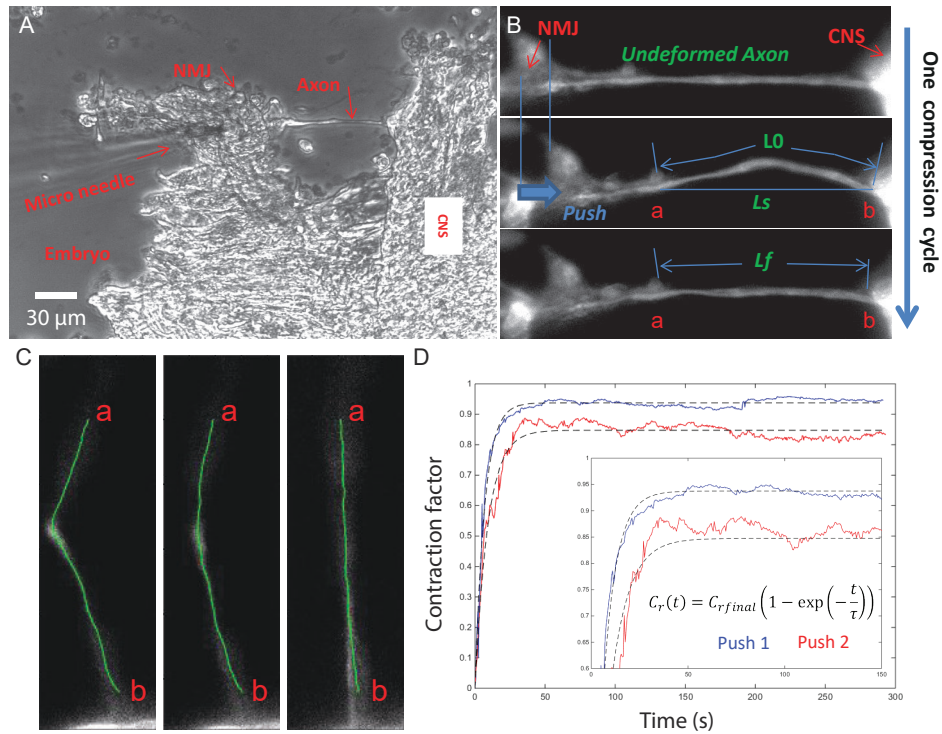
Figure 2.1: Experimental setup and data analysis methods. (A) Phase contrast image of dissected embryo. The axon is being pushed with the microneedle from its NMJ end. (B) The geometrical parameters are labeled on the fluorescent image of an axon undergoing a complete slackening cycle. (C) Path length computation achieved by tracing intensity centroid along the length of axons at different time points. (D) Contraction factor vs time plot of an axon pushed twice. Dotted lines are least-square fits of the inset equation to the raw data. Inset plot provides an expanded look at the transient region.

To remove tensile force in axonal shaft, the axon was compressed from the NMJ side (Fig. 2.1A), which caused the axon to buckle and become slack (Fig. 2.1B). However, the axon exhibited gradual self-shortening (Fig. 2.1B & C) and ultimately reached a stable straight configuration (Fig. 2.1D) within 2-3 min (end of compression cycle 1/push 1). The degree of contraction for each axon in a cycle was characterized by the contraction factor C_r defined as,

$$C_r = \frac{\Delta L_f}{\Delta L_s} = \frac{L_0 - L_f}{L_0 - L_s}. \tag{2.2}$$

Here $0 \leq Cr \leq 1$. $C_r = 0$ indicates no contraction ($L_0 = L_f$); $C_r = 1$ indicates full contraction ($L_f = L_s$, for nomenclature see Fig. 2.4A and Table 2.1). All embryos showed high degree of contraction, with C_r = 0.90–0.95 in cycle 1. In order to investigate whether the shortened axons could further contract when subjected to another round of slackening, we examined the same axon for a 2nd compression cycle (push 2) after one hour ($\Delta T_1 = 1hr$). The axon reached a steady state and became fairly straight within 2–4 minutes with $C_r = 0.80$–0.90. Finally, the same axon was pushed for the 3rd cycle (push 3) after half an hour ($\Delta T_2 = 0.5hr$, Fig. 2.2A & 2.4B). Again, shortening occurred within 2–4 minutes with a C_r close to those in previous cycles. This was consistent among all six embryos examined (Fig. 2.2B). Note that because the axon length decreased at the end of each compression cycle, the values of L_0, L_f and L_s vary among compression cycles. It is also worth noting that the total compressive strain (based on L_0 in cycle 1 and L_f in cycle 3) exceeded 40% in some embryos, although axon length varied from 70 μm to 105 μm from embryo to embryo.

These results show the rapidity and robustness of axon shortening in response to multiple occasions of loss of tension. Results here will also serve as our control data for the latter sections where embryos were subjected to various pharmaceutical treatments.

Axon contraction shows exponential decay over time with less shortening rate in 2nd compression cycle

To study the dynamics of *Drosophila* axon contraction, we monitored time lapsed images of axons and measured their instantaneous change of length over time (Fig. 2.1C) during both the 1st and 2nd compression

cycles. The time-dependent contraction can be fitted to a first order exponential equation as:

$$C_r(t) = C_{r_{final}}(1 - e^{-\frac{t}{\tau}})$$

(2.3)

where experimentally $C_r(t) = \frac{L_0 - L(t)}{L_0 - L_s}$; $L(t)$ is the instantaneous length; τ is the characteristic time constant (Fig. 2.1D).

$C_{r_{final}}$ (reported simply as C_r in the previous section, Eq. 2.2) and τ represent the two independent parameters characterizing the magnitude and rate of axon contraction respectively in a given compression cycle.

We found that all axons exhibited a generic exponential decay in shortening over time in both cycles (Fig. 2.1D). We further analyzed the behavior by plotting $\ln(1 - \frac{C_r(t)}{C_{r_{final}}})$ as a function of time. Data from six randomly chosen axons show a linear dependence (Fig. 2.3). However, contractions in the 1st cycle, performed either immediately (n=6) or one-hour after (n=6) embryo preparation, had a faster rate of contraction (consistently among embryos) compared to the 2nd cycle (n=6, Fig. 2.2C). The one-hour-delay experiment was done to assess any saline incubation effect. Note that C_r was similar in both cycles and seemed to be largely independent of τ.

Contraction is distributed along the length of axon

The magnitude (C_r) and rate (τ) of contraction quantify bulk response of the axons. In order to gain insight on the source of contraction, such as which cyto-machinery is involved, we quantify local dynamics of the axons along their lengths. First, we overlaid the profiles of the same axon at different time points during contraction (Fig. 2.2D), and traced the positions of a few markers along the length (red arrows). If the contractile units are localized to a specific region, for an example the NMJ, all the fluorescence markers will move towards the NMJ when tensed—with displacement magnitude decreasing as we move away from the NMJ. The different markers did not move towards the same end of the axon. This implies that the source of contraction is distributed and is not localized to the NMJ or CNS side.

Contraction Behavior of Axons Subject to Drugs Treatment

In order to explore the mechanism of axonal contraction, we investigated contraction response of axons subjected to various pharmaceutical drugs. Each drug has potent ability to impair/disrupt specific cellular activity/structure in axons as discussed in the following sections. Results from the previous sections (Fig.
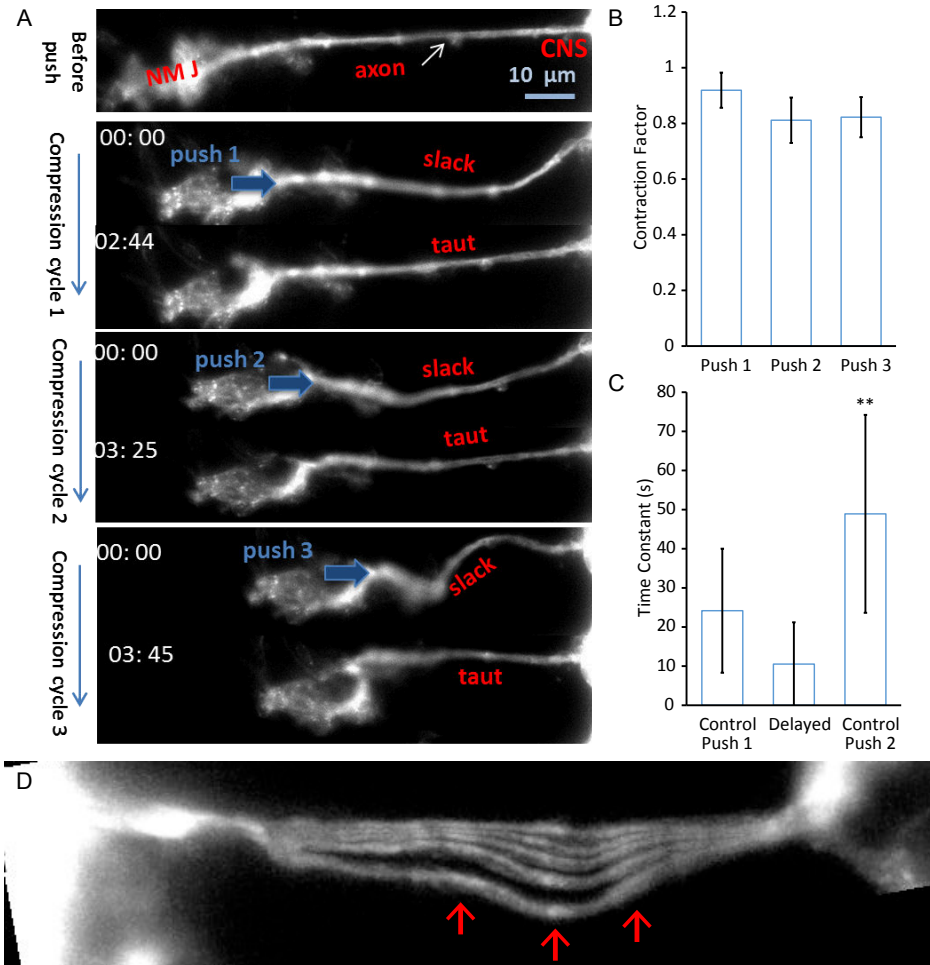
Figure 2.2: Axon shows robustness and nonlocalization in contraction. (A) Experimental images showing an axon contract during three consecutive slackening cycles. The contraction strain in each cycle is 10–15% of initial length (L_0 in each cycle). Note that axon contracts and becomes taut upon each push within 2–4 minutes. Total shortening is about 40% of original length (L_0 in cycle 1). (B) C_r for each compression cycle demonstrating robust axonal contractility (n=6 in all groups). (C) Time constants of contraction for axons pushed (1st time) immediately after surgical preparation, pushed (1st time) 1 hr after surgery, and pushed the 2nd time 1 hr after the first push (n=6 in all groups). (D) The same axon overlaid at different time points: 0, 10, 20, 30, 50 seconds after push. Movements of fluorescence intensity features (marked by red arrows) reveal a change in forcing direction along the length. All error bars in standard deviation.
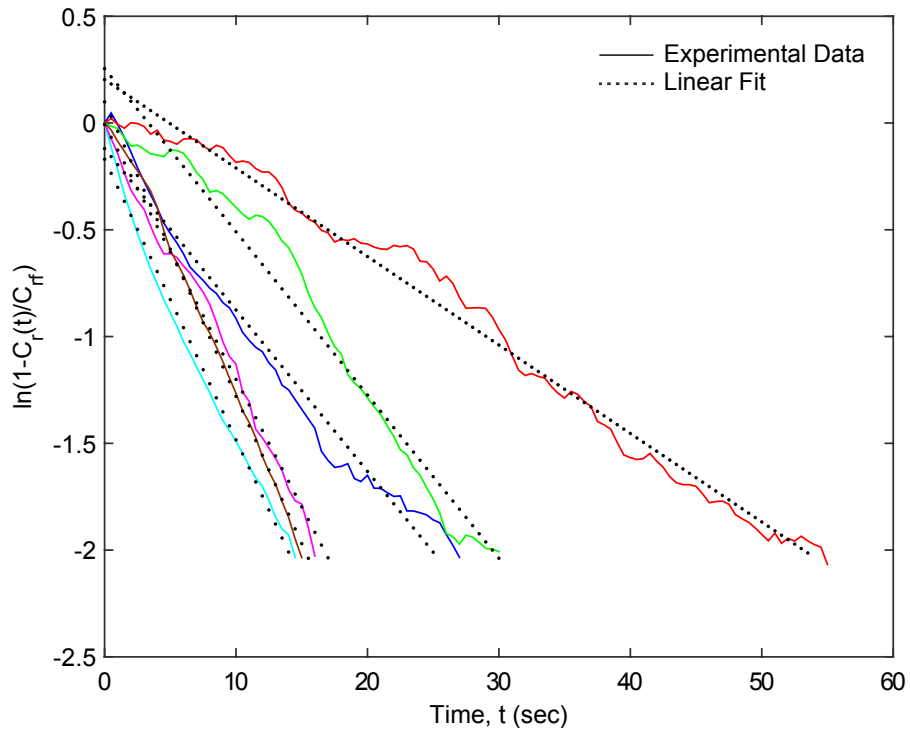
Figure 2.3: Log-linear plot of contraction dynamics of six randomly chosen axons. Sets of experimental data are colored in solid lines. Corresponding best linear fits are graphed in dotted lines.
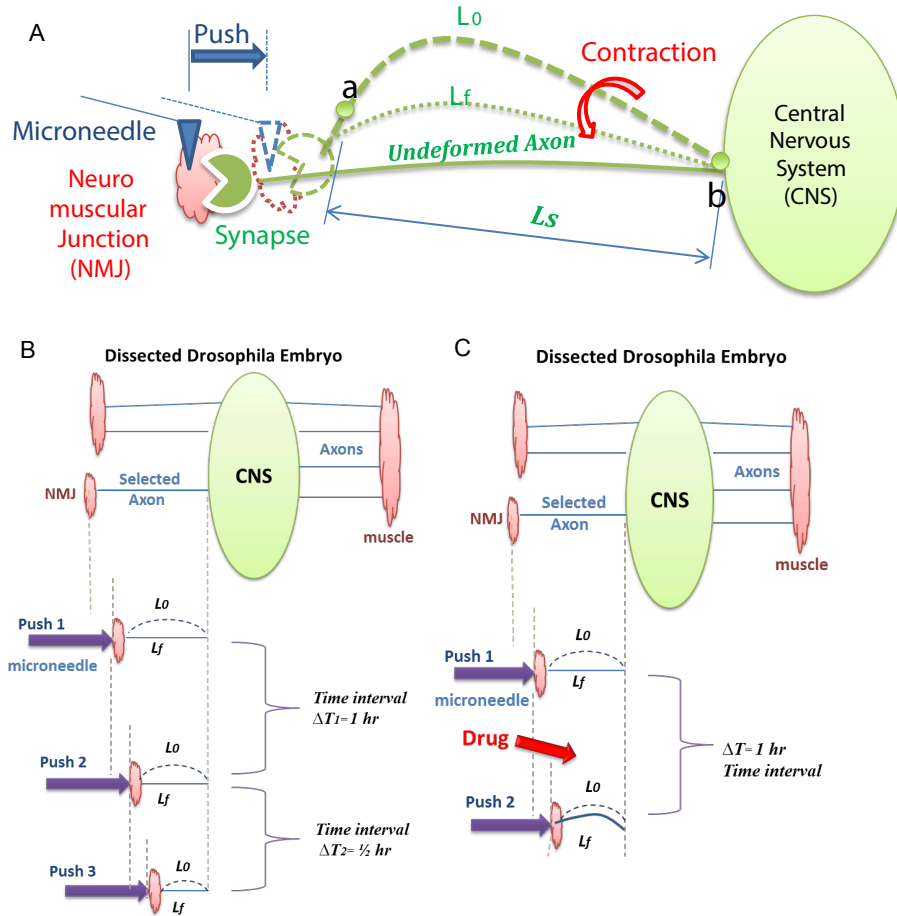
Figure 2.4: Cartoon Schematics. (A) Graphical representation of various notation used. (B) Procedures of control experiments. (C) Procedures of pharmaceutical experiments.

2.2B & 2.4B) serve as the control group. Fig. 2.4C provides a detail schematic of the procedures. Briefly, all drugs were added immediately after the completion of push 1 and let sit for $\Delta T = 1$ hour, similar to that in control, before push 2 is commenced.

Axons contraction is active and requires metabolic energy for contraction

To investigate whether the process of axon contraction is active and hence requires metabolic energy, the embryos were treated (n=6) with combined 2Deoxyglucose (60 mM, 1 hr) and Sodium Azide (20 mM) to deplete ATP [21]. As expected in the first compression cycle, the axon contracted with $C_r = 0.80 \pm 0.10$, while in the second compression cycle, the contraction factor noticeably dropped to $C_r = 0.13 \pm 0.09$ (Fig. 2.2A). Thus ATP inhibitory reagent significantly impaired axon contraction suggesting that axonal contractility is an active process supported by metabolic energy. We note that ATP depletion may lead to impairment of

myosin II motors and major actin filaments depolymerization, both verified in the following sections to lead to loss of tension and contractility of the axon.

Myosin II contributes to force generation in axons through MLCK and ROCK pathways

In the first set of experiments, we used transgenic embryos that expressed UASzipRNAi in neurons to knock-down zipper [19], the gene encoding non-musecle mysoin II in *Drosophila* (n=7). We observed significant inhibition of axon contraction ($C_r = 0.31 \pm 0.13$), indicating that Myosin II mediates axons contraction (Fig. 2.5B).

To further identify the molecular pathways by which Myosin II is activated in axons, we separately treated the embryos with reagents ML-7, an inhibitor of Myosin light chain kinase MLCK [14] (n=6, 225 μM, 1 hr), and Y-27632, an inhibitor of Rho-dependent kinase [22] (n=6, 110 μM, 1 hr). Both ML-7 and Y-27632 reduced axon contraction in the 2nd cycle, with $C_r = 0.36 \pm 0.20$ and 0.33 ± 0.17 respectively (Fig. 2.5C & D). Drugs effects have saturated at the concentration reported here (Fig. 2.6). Contraction was also significantly reduced at lower concentrations (70 μM & 35 μM for ML-7 and Y-27632 respectively, Fig. 2.6) [27, 28]. These results together indicate that both MLCK and ROCK pathways contribute to Myosin-based contraction and force-generating machinery in live *Drosophila* axons (Fig. 2.5E).

Axon contraction stops upon disruption of F-action/cortical actin

Myosin motors employ actin filaments to generate intracellular tension. Therefore, if myosin II is indeed involved in axonal contractility, then disruption of actin filaments should also result in loss of contractility. To examine this hypothesis, embryos were separately treated with Cytochalasin D (50 μg/mL, n=6) and Latrunculin A (31 μM, n=6), potent reagents that disrupt actin filaments [25, 23, 24]. As it is evident in Fig. 2.7A, both Cytochalasin D and Latrunculin A significantly impaired the ability of axons to contract, characterized by the reduced values of $C_r = 0.18 \pm 0.12$ and $C_r = 0.16 \pm 0.13$ in the 2nd cycle respectively.

Disruption of microtubules accelerates contraction dynamics

Since the axonal shaft is abundant with microtubule filament (MT), we ask whether MT has any direct role in axonal contraction. To address this question, the embryos were treated separately and simultaneously with Nocodazole (15 μg/mL) and Colchicine (200 μM), potent drugs to destabilize microtubules [16, 29]. After drug treatments, axons maintained a high $Cr = 0.87 \pm 0.11$ (n=4, Nocodazole), 0.89 ± 0.05 (n=4,
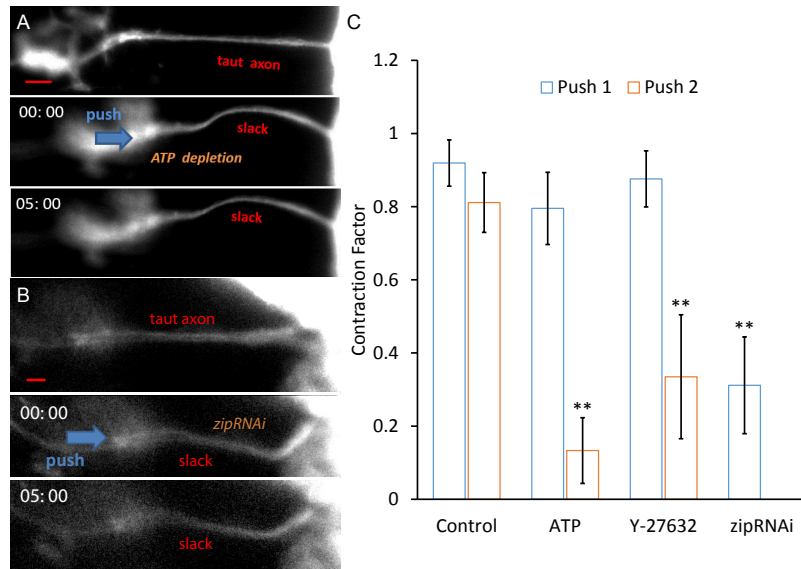
Figure 2.5: Effect of pharmaceutical and genetic NMMII disruption. (A) Axon contraction stops when ATP is depleted by treating embryos with 2Deoxyglucose and Sodium Azide. This indicates that axon contraction is active and needs metabolic energy (n=6). Similarly, axons stops to contract when non-muscle Myosin II is knockdown by (B) zipRNAi (n=7), and inhibited by (C) ML-7 (MLCK pathway, n=6) and (D) Y-27632 (ROCK pathway, n=6). (E) Summary of results suggesting that myosin II is involved in active force generation in *Drosophila* axons. Note that no drugs are used in control cases. Scale bar $= 10\ \mu$m. All error bars in standard deviation.

Figure 2.6: Effect of ML-7 (A) and Y-27632 (B) at approximately 67% & 33% of the concentration reported in the main text. N=6 in all cases. All error bars in standard deviation.
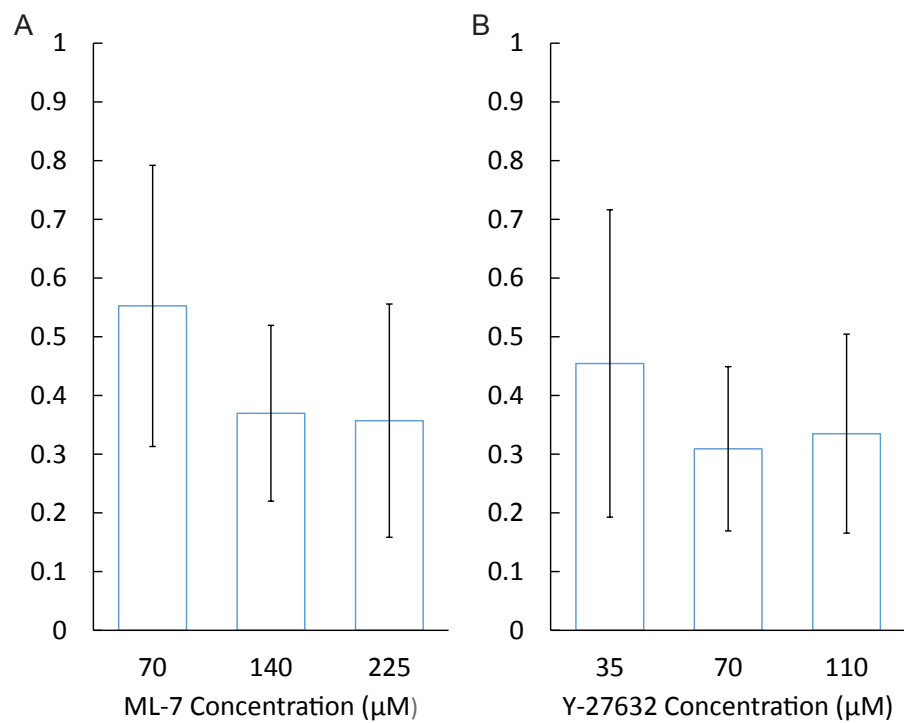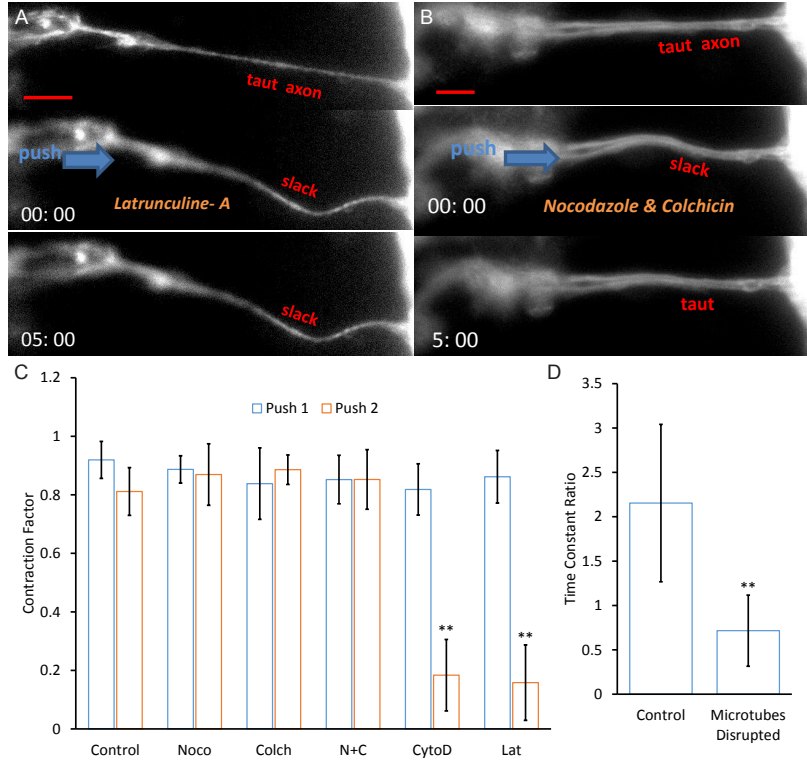
Figure 2.7: Effect of pharmaceutical cytoskeleton disruption. (A) Axon contraction is significantly inhibited when embryo is treated with Cyto D (n=6) and Latrunculine A (n=6). (B) Axon contraction factor remains unaffected, as compared to control cases, when embryos are treated with Nocodazole (n=4) and Colchicin (n=4) independently and combined (n=6). (C) Summary of results shows a significant decrease in axon contraction when actin structures are disrupted while axon contraction factor remains insensitive to disruption of microtubule filaments. (D) Time constant ratio (τ_2/τ_1) significantly reduced (n=5), indicating that contraction is happening at a faster rate, when microtubules are disrupted. No drugs are used in control cases. Scale bar = 10 μm. All error bars in standard deviation.

Colchicine), and 0.85 ± 0.10 (n=6, Nocodazole + Colchicine) in the 2nd cycle—similar to the control data, indicating that axon contraction factor alone is insensitive to MT disruption (Fig. 2.7B & C). Disruption of microtubules resulted in tubulin beading along the axon and a reduction in α-tubulin intensity (Fig. 2.8), as typically observed in microtubule disruption experiments [29]. Time constants comparison reveals that the microtubule disruption expedites the contraction, i.e. the axon contracts faster and this is reflected in τ. The ratio of the time constants (contraction time constant of push 2 divided by that of push 1, $R\tau = \frac{\tau_2}{\tau_1}$) with and without microtubule disruption is $\frac{R\tau_{(\mu T-)}}{R\tau} \simeq \frac{1}{3}$ (Fig. 2.7D), suggesting that microtubules act as resistive and dissipative elements in axonal contraction.
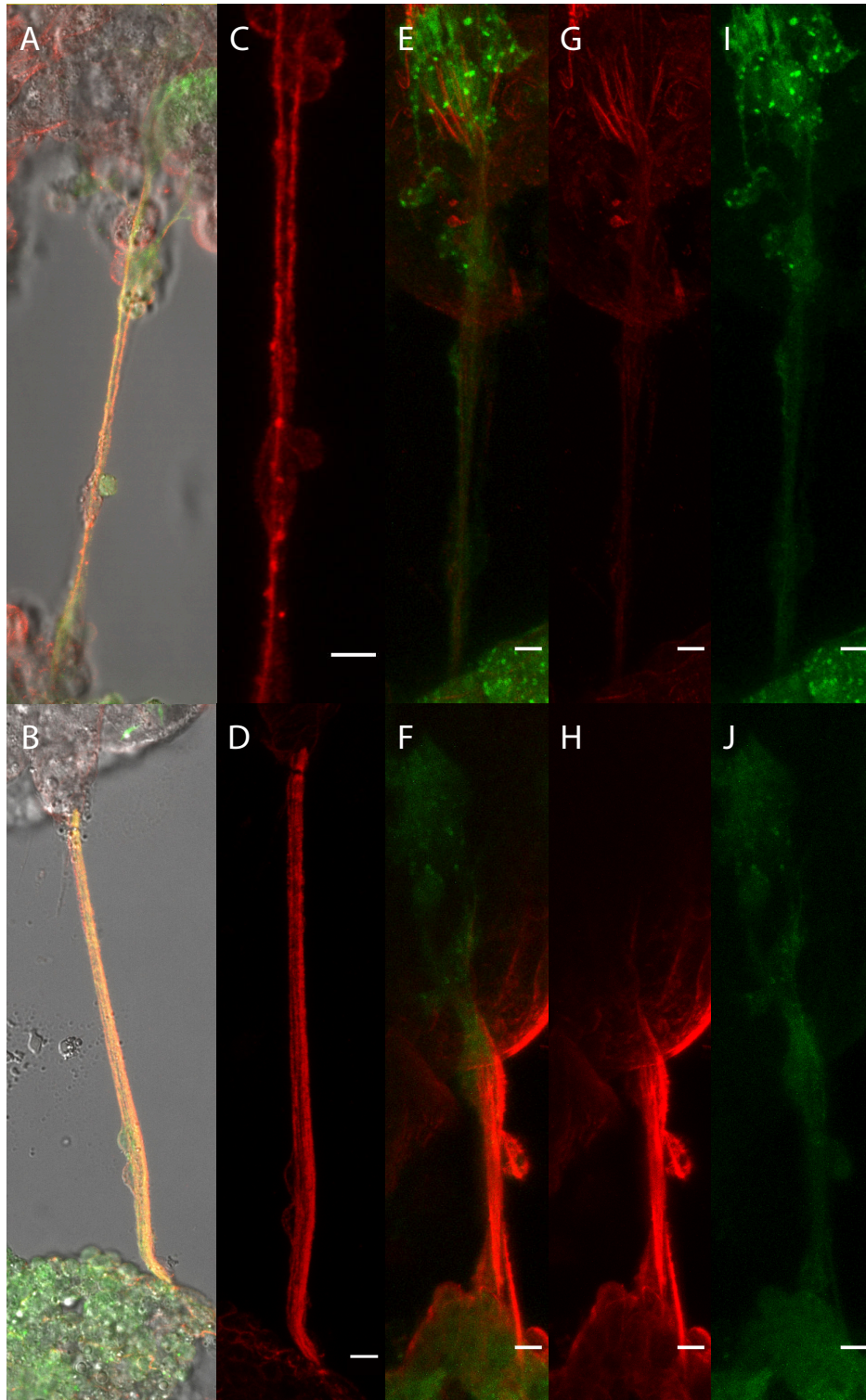
Figure 2.8: DIC, anti-α-tubulin, and neuronal-membrane-bound-GFP composite images with (A) and without (B) drug. Expanded images of microtubules morphology with (C) and without (D, reduced image gain by one-eighth due to saturation) drug. (E-J) Images obtained with a brief extraction step before fixation. Anti-α-tubulin and neuronal-membrane-bound-GFP composite images with (E, G, & I) and without (F, H, & J) drug. The composite images are separated into the two channels indicating the presence of polymerized microtubules (G & H) and neuronal membrane (I & J). Same imaging conditions applied unless otherwise noted.

2.4   Discussion

It has long been known that neurons cultured on petri dishes generate tension. Recent studies show that *in vivo* axons of embryonic *Drosophila* also generate tension [2]. More importantly, this tension seems to play critical roles in clustering neurotransmitter vesicles at the presynaptic terminal. Such clustering is essential for neurotransmission. Here we seek for the origin of tension in neurons in embryonic flies by applying a series of cytoskeletal disruptive drugs. Our key conclusion is that acto-myosin machinery is primarily involved in the contractility of axons of embryonic motor neurons. This contractility results in tension in the axons. We have the following remarks.

Glial cells possibly influence axon contraction

Physiology studies [30] have shown that glial ensheathment, continuous along the nerve, is complete at stage 17. The embryos that we worked with (stage 15–16) also showed a high degree of glial ensheathment, as evident by immunofluorescence staining targeting repo, a gene that expresses only in glial cells (Fig. 2.9). However, possibly because of the immature coupling between glial cells and axons, all of our cleaned preparations showed minimal ensheathment along the shaft of the axons (Fig. 2.9). The axons were still able to contract and generate tension in the absence of glial cells along their length. It is therefore unlikely for the glial populations to influence the rest tension and the contraction factors reported in this work. However, it is possible that glial cells also contribute to axon contractility locally providing more resistance to buckling, which in turn influences the bulk time constant (Fig. 2.2C) and the profile after deformation and during the contraction process (Fig. 2.2D).

Acto-myosin machinery is important in generating axon rest tension *in vitro* and *in vivo*

In vitro studies revealed the role of cytoskeletal structure and motor protein activity in contractility of axon in different types of neurons. For instance, disruption of F-actin eliminates retraction of neurites [14, 31]; depolymerization of actin network leads to a significant reduction in the rest tension in axons [32]. The role of actin in axonal contractility in embryonic *Drosophila*, in which actin was observed to actively participate in contraction dynamics (Fig. 2.7A & C), seems to be consistent with the *in vitro* studies.

Motor protein also have significant role in force generation and motility of axon. For example, it is shown that retractions in chick sensory neurons [31], Neuro–2A neurites [22], and DRG neurons [14] are
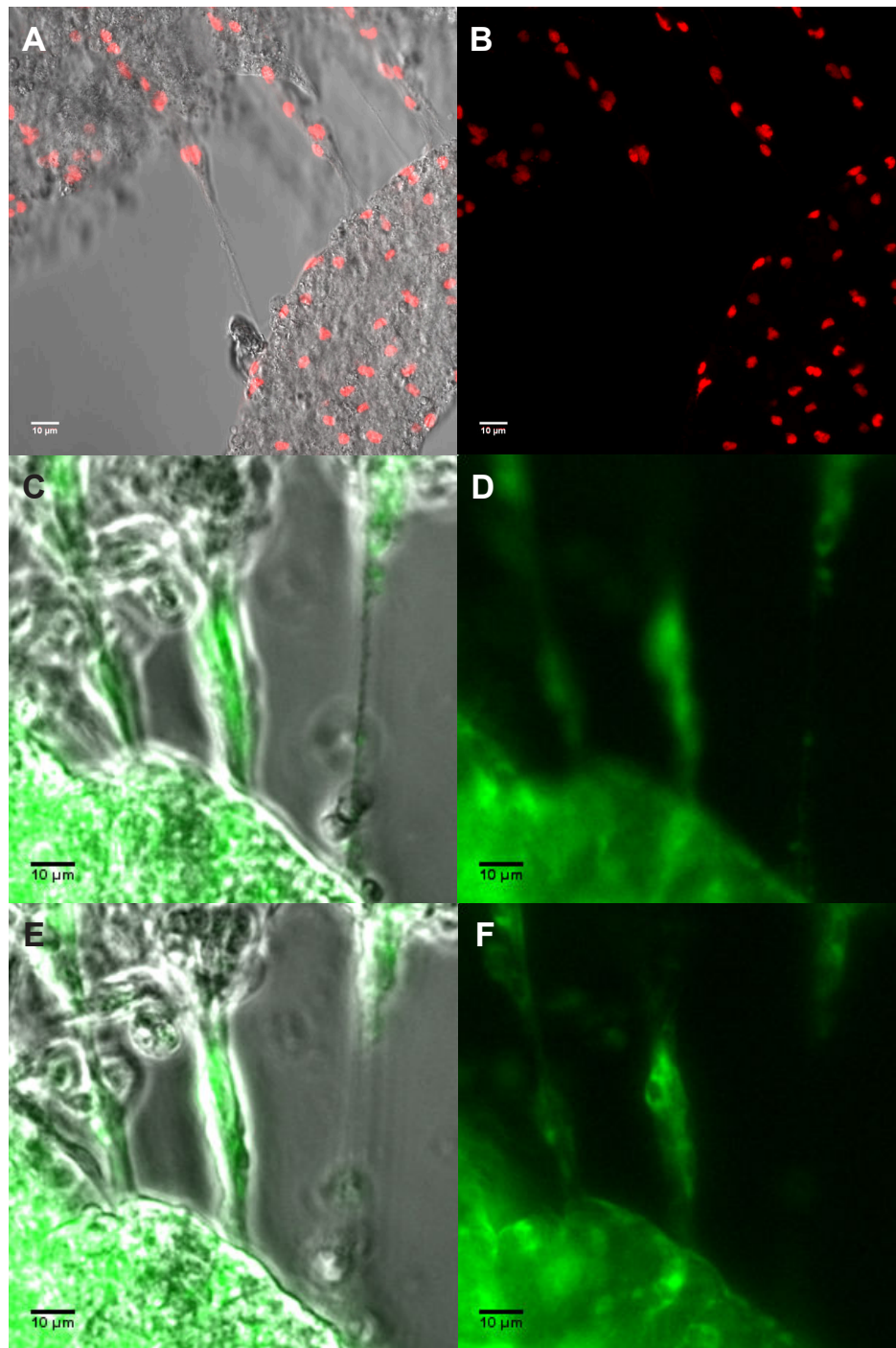
Figure 2.9: Glial cells visualizations, through staining (A-B) and crossing (C-F), show high degree of glial ensheatment of uncleaned axon, and minimal ensheathment along the axon shaft of cleaned axon. (A) DIC and anti-repo composite image of preparation. Cleaned axon on the left. (B) Anti-repo channel of A. (C & E) Phase and glial-membrane-bound-GFP composite images at 2 different focal planes. Cleaned axon on the right. (D & F) Glial-membrane-bound-GFP channel of C & E respectively.

significantly dependent on Myosin II. These agree with our observations that Myosin II plays a major role in contraction dynamics: axon contraction was significantly impaired when Myosin II was downregulated by RNAi and inhibited using pharmaceutical reagents (Fig. 2.5). This, combined with our results on actin disruption, strongly suggests that the interplay of acto-myosin machinery drives the fast active contraction of slackened axons. It is also conceivable that actin network serves as force conduit along the axonal shaft. They can sustain and transmit both external force [32] and internally generated tension (by Myosin motors, current work); and hence, once disrupted, contractility significantly dropped in axons.

Microtubules participate by sliding, breaking, and densifying

The profile of buckling in our experiments was rarely of mode I, and was usually a combination of multiple modes. This leads us to believe the observed deformation profile is driven by the microtubules, known to couple with surrounding cytoskeleton to buckle at higher modes for withstanding compressive load [33]. Under acto-myosin contraction, the buckled microtubules are thought to slide against each other, possibly influenced by tau proteins [34], leading to axon shortening. This allows the slackened axon to straighten and build up tension [12]. Dynein motors might also be actively resisting the contraction [35]. The time evolution of axon contraction in each cycle is analogous to that of a system modeled by a first order decay equation (Fig. 2.1D), suggesting the presence of resistive/dissipative elements [36], supporting the hypothesis of microtubules sliding [37]. Breaking of microtubules might occur at high compression rate/magnitude as well [26]. The rate at which they reassemble may influence the contraction dynamics. It is worth noting that such reassembling processes usually occur over a much longer time scale of axonal shortening, i.e. 40 minutes, than what we observe here [26]. The subsequent reorganization and reassembling of microtubules can further lead to a formation of a denser filamentous network upon axon shortening, which could explain the slower dynamics (higher time constant) in push 2 in our experiment. We showed that the time constant increase was reverted, i.e. shortening was expedited, when microtubules were disrupted, supporting the hypothesis. Others have also shown that microtubules counterbalance tensile forces along the F-actin *in vitro*. For instance, disruption of microtubules in axons leads to an increase in rest tension [16, 32]; and destabilization or stabilization of microtubules resulted in enhanced or retarded recovery rate of dynamically-stretched axons respectively [26].

Force can mediate actin polymerization to scaffold synaptic vesicles

Contraction of slack axons along their entire length (Fig. 2.2D), and the exponential time dependence of contraction (Fig. 2.1D & 2.3) lead us to believe that axonal contractility results from a continuous network of
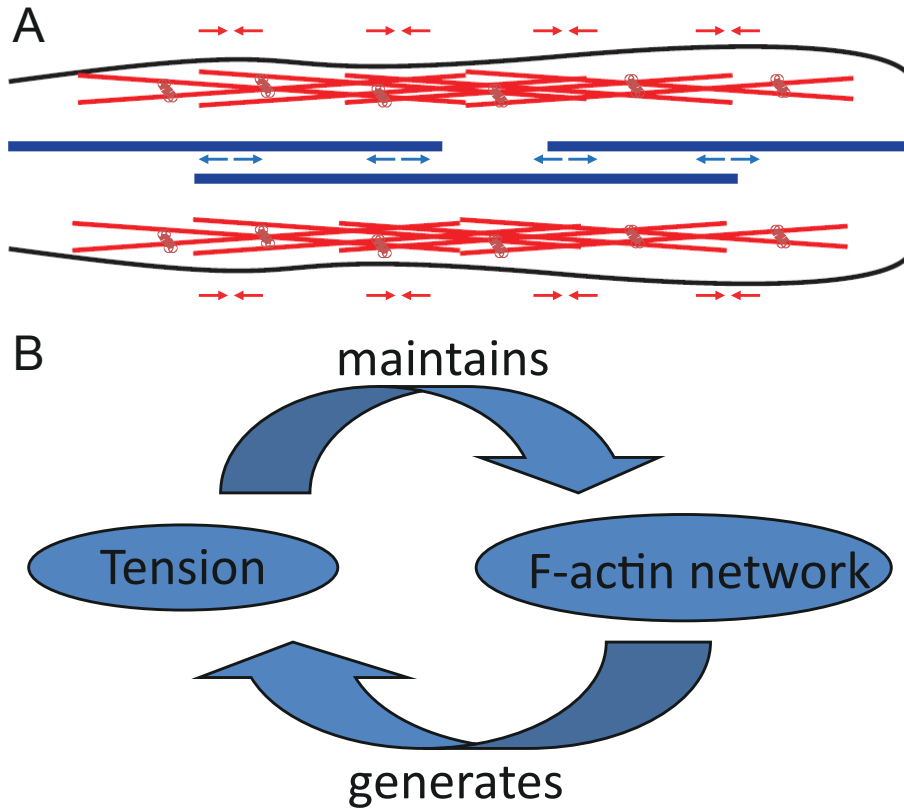
Figure 2.10: Schematic of a possible mechanism in force generation and contraction. (A) Cartoon schematic of a possible cytoskeleton configuration with cortical acto-myosin network (red network) generating tension along the axon, and microtubules (blue strands) resisting the contraction and providing support actively through molecular motors and/or passively through crosslinking proteins. (B) A possible loop mechanism in which actin network is stabilized by the tension it generates. Such stable network may facilitate neurotransmitter vesicle clustering at the synapse, as well as other biological processes.

cortical actin filaments [38] rich in myosin motors, but the contraction is hindered by a frictional component originating from the central network of other cytoskeleton filaments, dominated by microtubules. This is summarized in Fig. 2.10A.

Tension is known to facilitate actin polymerization [39], and a loss of tension could lead to actin disassembly. It is thus possible that the self-generated tension sustains the actin network, especially further downstream in the actin rich presynaptic terminal—to provide a scaffold for synaptic vesicles clustering, shown to be sensitive to all actin [40], myosin [19], and tension [2] disruption.

Tension can influence stretch sensitive ion channels

Maintaining tension might be vital for the functionalities of ion channels. It has been argued that all ion channels are mechanosensitive—a large enough stress will induce conformational change in ion channels which would lead to an increase/decrease in their activation energy barrier for conductance [41]. Thus, it is conceivable that the tension generated by acto-myosin machinery might serve as a signal for the ion channels. The latter in turn may influence polymerization of cytoskeletal components and motor activity by regulating their ion transport. Thus, the channels and the acto-myosin machinery may act as a feedback loop system maintaining the rest tension and resulting in an optimal condition for neuronal functions.

Tension can promote efficient wiring

It has been suggested that cortical folding in cerebral cortex of large mammals could be driven by intrinsic axonal tension aiming to pack the most neurons in a confined space, i.e. efficient wiring [42]. Several efforts have been attempted to (dis)prove this hypothesis [43, 44]. Most experimental results suggest that intrinsic tension does not cause cortical folding, but no evidence has so far been presented against its role in efficient wiring.

As is evident from some previous experiments [2, 45], neurons respond to mechanical stimuli. However, a neuron, like any long wire, can only sense mechanical signal efficiently when it is tensed. The ultimate role of tension homeostasis in neurons may not merely be limited to growth as is conventionally understood, but might be related to various neuronal functions, including axonal transport and synaptic transmission and excitability.

Chapter 3

The origin of circumferential axonal tension

This chapter is adapted from a previous publication[1].

3.1 Motivation

Neurons compute by integrating upstream signal inputs and propagating a single output. This signal integration and propagation requires the neuronal cell to take a specialized shape—usually in the form of many dendrites and an extended axon [1]. Microtubules (MT) has been thought to give axons their tubular structure [46], and actin, in the form of a mesh network, was proposed to link the cytosolic MT to the axolemma [47]. The recent discovery of periodic subcortical actin rings and associated proteins in axons [38] (and dendrites [48]) adds new insights to the cytoskeleton architecture. This highly regular actin network has been suggested [49, 50] and demonstrated [51] to maintain structural integrity. How such is achieved, however, remains largely speculative.

The contractility of actin network, driven by myosin motors, is well-established to help shape cell morphology [52, 53]. In axons, the acto-myosin machinery maintains an intrinsic axial tension *in vitro* [54, 32] and *in vivo* [2, 44, 55]. This tension can influence axonal processes such as growth [3, 56, 5, 57, 37, 58], synaptic plasticity [2, 18], and vesicle transport [17] and release [45]. We speculate that tension could also exist in the circumferential direction, creating a hoop stress, as suggested by the ring-like actin network.

Here we use confocal microscopy and spatial light interference microscopy (SLIM) [59] to infer circumferential tension by monitoring the diameter of single axons in embryonic *drosophila in vivo*. We report observations that suggest that this circumferential tension is coupled with the axial tension. It appears that axons regulate their diameter, and hence structure, through this coupled contractile tension.

---

[1]Fan A, Tofangchi A, Kandel M, Popescu G, Saif MT. Coupled circumferential and axial tension driven by actin and myosin influences in vivo axon diameter. Sci Rep. 2017

3.2 Materials & Methods

Drosophila Culture

Transgenic embryonic *drosophila* (P(elav-GAL4)[iii] P(UAS-gap::GFP, w+)[6iii]) with neuronal membranes tagged by green fluorescent protein (GFP) were used for the experiments. To harvest the embryo for dissection, flies were cultured on standard grape agar plates at room temperature (23 °C) for 18 hrs. The new embryos laid (0-18 hours old) were treated with 50% bleach for 1 minute for dechorionation, and subsequently rinsed with deionized water. We then visually inspected the embryos to select the ones with morphologies corresponding to those of stage 16. This protocol was adapted from Budnik et al. [20].

Dissection and Manipulation

Selected embryos were then transferred onto a double-sided tape (Scotch; 3M, St. Paul, MN) attached to a large glass cover slip (12-545H; Fisher Scientific, Hampton, NH). We positioned the embryo specifically with the dorsal side, where the CNS was, touching the tape. A glass needle (World Precision Instrument, Sarasota, FL), pulled by a micro-electrode puller (Sutter Instruments, Novota, CA), of 1 μm tip size and a 20° taper was used to cut open the embryo from the posterior end to the anterior end. The fly, now free from all its cuticle, naturally adhered to the glass needle. We transferred it onto the cover slip glass surface, covered it with 500 mL of PBS (the volume is important for later drug concentration), and subsequently removed the inner organs until the body wall could be laid unrolled with the CNS exposed for further manipulations.

Intersegmental nerves, aCC motor neuron (MN) and RP2 MN, were identified from one section of the flat body wall. We gently excised the surrounding fat cells, muscle fibers, and nearby neuron while leaving the entire connection—CNS→aCC+RP2→NMJ—intact.

A different glass needle of similar specifications was then brought close and made adhere to the muscle side of the NMJ using a piezoelectric micro-actuator (NanoPZ PZC200; Newport, Irvine, CA) that provided nanometer resolution.

Pharmaceutical Drug

Cytochalasin D (50 μg/mL) was used for the disruption of F-actin. Nocodazole (15 μg/mL) and Colchicine (200 μM) were used for the disruption of MT. Y-27632 (110 μM) and ML-7 (225 μM) were used to inhibit the ROCK and MLCK pathways respectively. All chemicals were purchased from Sigma-Aldrich (St. Louis,

MO). DMSO was added as a solvent and was maintained at a final concentration of less than 1%, tested to have no observable effect [55]. All drugs were diluted in Ca^{2+}/Mg^{2+} free PBS. Drugs were added to the samples 3 minutes before the onset of measurements.

Microtubules Staining

The prepared embryos were extracted with BRB80-4mM EGTA-0.5% TX-100 (chemicals from Sigma, St Louis, MO) for 30 seconds to distinguish polymerized MT and fixed with 4% formaldehyde (28908; Fisher Scientific, Rockford, IL) for 15 minutes; blocked in 5% Bovine Serum Albumin (A9647; Sigma-Aldrich, St. Louis, MO) for 10 minutes; conjugated with mouse anti-α-tubulin (1:10; 12G10; DSHB, Iowa City, IA) for 60 minutes; tagged with Alexa 647 goat anti-mouse (1:200; A-21236; Fisher Scientific, Rockford, IL) for 30 minutes; and imaged with a scanning confocal microscope (LSM700; Carl Zeiss, Peabody, MA) afterwards. Samples were rinsed with PBST (PBS-0.1% Triton X-100) after each step. All steps were performed at room temperature.

Confocal Imaging

The embryos were inspected using a confocal microscope (LSM700; Zeiss, Oberkochen, Germany). The 488-nm laser was used to excite the GFP and emission light with wavelength larger than 488 nm was collected. Pinhole size was set to 1 a.u.. A z-stack distance of 0.41 μm was maintained. A 40x/1.3 objective was used. We note that the number of images (ranges from 15-50) for any axon depends on its degree of out of plane tilt. We discarded samples with too much tilting that needed more than 50 images in the stack. The scan speed was sometimes adjusted so that an image stack could be obtained in around 80 seconds. The settings were kept consistent across all independent experiments. Image stacks were taken every 5 minutes. We found that this minimized photobleaching while allowing images to have adequate spatial and temporal resolution for our analysis.

Image Analysis

The collected images were post-processed first using ImageJ (U.S. National Institutes of Health, Bethesda, MD). The z-stacks were collapsed to single images by maximum intensity projection. The images were cropped to only the axon of interest which were then transferred to MATLAB (MathWorks, Natick, MA). A batch-enabled script was used to detect the edge of the axons, and subsequently performed diameter and area calculations (Fig. 3.1). The edge was traced by fitting a Gaussian profile to the intensity profile along the x-axis for every y (axial direction of axon). The 2 locations with maximum slope ($\frac{d^2 I(x)}{dx^2} = 0$)
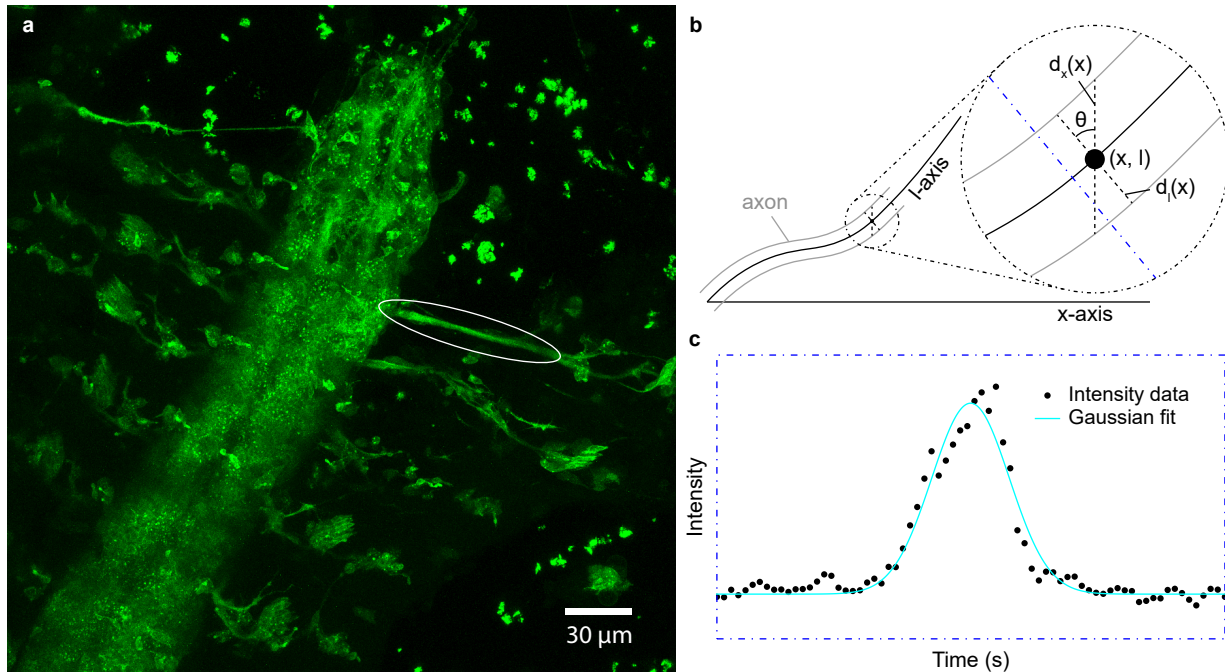
Figure 3.1: Approach to diameter calculation. (a) Maximum intensity projected fluorescence image of a dissected fly embryo. Signals are from neural membrane bound GFP. The white ellipse indicates a cleaned axon. (b) Schematics of an axon that has move away from its original axis (from x-axis to l-axis). Values of average diameter computed along the 2 axes separately are different by a factor of $cos\theta$. (c) Gaussian curve (G) fitted to maximum fluorescence intensity data along the cross-section (blue dotted line in b) of a randomly-selected axon. Points where $G'' = 0$ is defined as the boundary.

were reported for each y-coordinate. Connecting those points for all y-coordinates provided a discretized edge with axial resolution of a single pixel and lateral resolution of at least half a pixel. 3D images were generated by ImageJ to ensure that the distance between the 2 projected edges was representative of the diameter. Using the edge values, average diameters were computed over the same visible axonal length for each condition among different time points.

Spatial Light Interference Microscopy (SLIM)

SLIM was also used to examine the diameter and axonal mass transport. The sample preparation is similar to that previously described with slight modification to facilitate phase imaging. Specifically, we added a top cover slip above a PDMS spacer to seal off the sample and prevent evaporation. In addition, the space between the two cover slips (one supporting the embryo and the top cover) was filled with PBS. This offered flat interfaces for PBS to avoid any bias in the phase values during light transmission. Because of the top cover slip, no stretching manipulation was done to the samples imaged with SLIM.

In short, SLIM is a quantitative phase imaging [60] technique that measures optical path length shifts in a phase contrast geometry [59]. In our implementation (CellVista SLIM, Phi Optics, Inc.), the pupil plane of a Zeiss Z1 is projected onto a spatial light modulator (SLM) that is then cycled in $\pi/2$ increments, essentially modulating the phase ring internal to the objective. Four such images are combined [61] to produce a full-field phase-map, with a radian value at each pixel. All SLIM images used in this work were acquired with a 63x/1.4 objective (PN 420781-9910) and an sCMOS camera (Andor Zyla 5.5).

Each stack was used to reconstruct a single image to facilitate analysis (Fig. 3.2). The stack was first cropped to a region that only the axon of interest was visualized. Then, for each 5-pixel-times-width region along the axial direction of the axon, we found the stack plane with maximum gradient magnitude and defined the plane as the focal plane. The obtained plane numbers were then smoothed using the robust linear method and subsequently interpolated for every pixel along the longitudinal direction of the axon. These values were then rounded and used to obtained a reconstructed image from the image stack.

To evaluate diameter, we made use of the negative phase region at the boundaries of the axon (Fig. 3.3). Similar to the Gaussian fitting previously described, we obtained a profile, this time in phase values, for every pixel along the axial direction. We smoothed the profile and computed its difference function. The 2 maximum peaks (locations with maximum slope) in the difference function bound by the negative regions were defined as the boundary.

3.3   Results

In order to image axon diameter continuously, invasive surgery was performed on *drosophila* embryo to clean the tissues (including glial cells [55]) surrounding the axon until single axons could be observed. The neural membrane was genetically labeled with GFP for visualization purposes. Two imaging methods were used— confocal microscopy and SLIM. The preparations were similar with SLIM samples having a top cover slip to facilitate phase imaging (Fig. 3.4a). Fluorescence signal from the neural-membrane-bound GFP provided contrast in the confocal system, while phase changes provided contrast in SLIM. Methods unique to each imaging modality were used to 1) reconstruct an image stack into a single image, and 2) compute the diameter (and average phase for SLIM) from the reconstructed image (Fig. 3.4b). See materials and methods for detailed description. Axons were subjected to a series of stretching manipulations as depicted in Fig. 3.5.
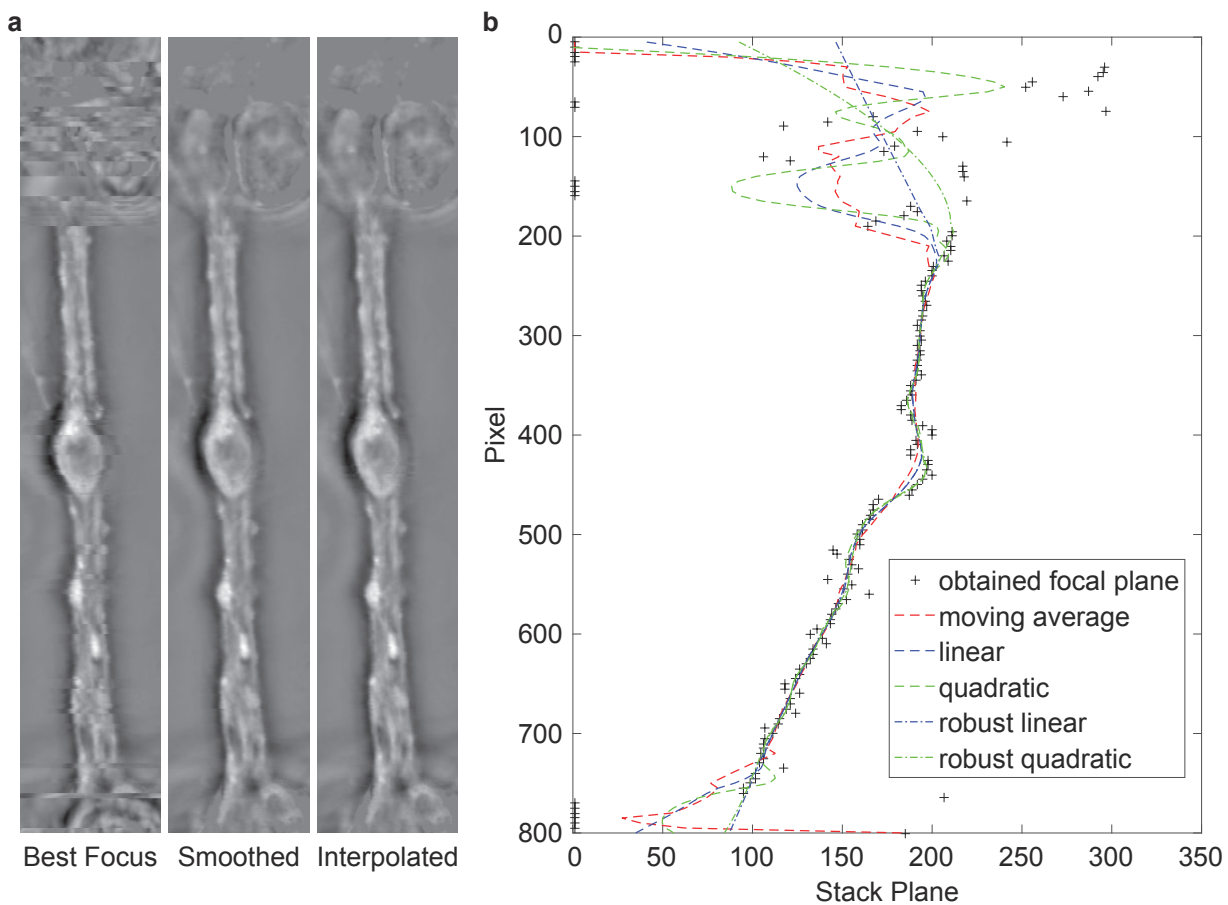
Figure 3.2: Reconstruction of SLIM stacks into a single image. (a) A computer-determined focal plane among the stack planes is obtained for every "5 pixel × width" section along the y-direction using the maximum gradient method. The reconstructed image (left) is grainy because of the discretized approach. The resulting pixel vs focal plane data is smoothed using the robust linear method. The reconstructed image (center) after smoothing shows significant improvements. This can be further improved (right) by linear interpolation of the 5-pixel data for every pixel. (b) We attempted multiple smoothing algorithm before we finalized on the robust linear method as it preserves feature at the extreme ends of the axon.
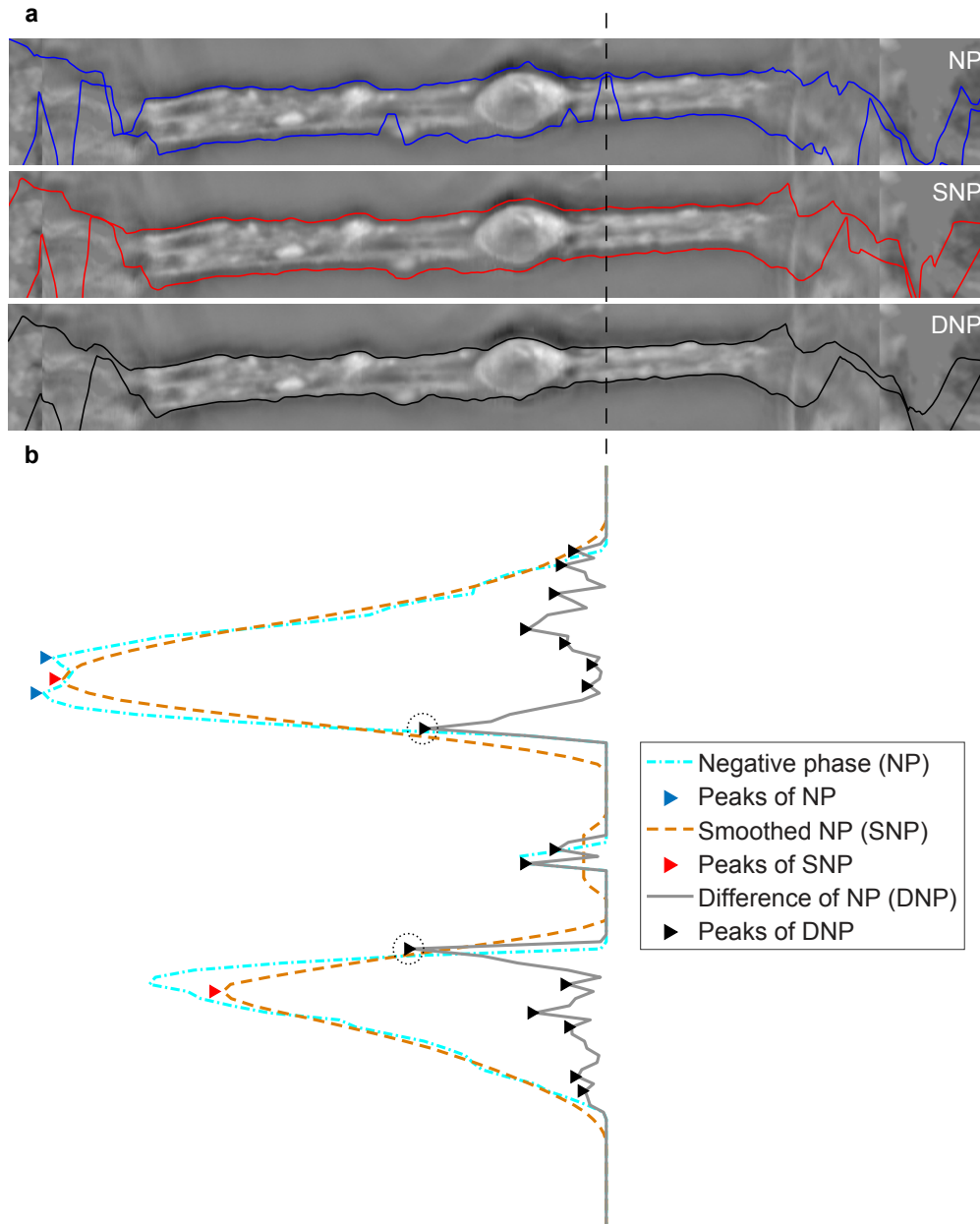
Figure 3.3: Determination of axon boundary in reconstructed SLIM images. (a) A negative phase region can be observed from the SLIM data at the 2 boundaries of the axon, which we can use to our advantage for diameter determination. We first look for the 2 maximum negative peaks (NP). However, there are local peaks that can bias the results. A moving average smoothing (SNP) takes care of that. The difference curve (DNP) of the smoothed data is obtained to locate the point of maximum slope (similar to taking a 2nd derivative with a continuous function), which we defined as the boundary points. (b) Plot of the negative phase data along the dotted line drawn in (a) to better illustrate the process. The peaks are pointed out in triangles. The final boundary points are circled in dotted line. Note that the phase values reported in the main text was never smoothed; the smoothing is done only during boundary determination.
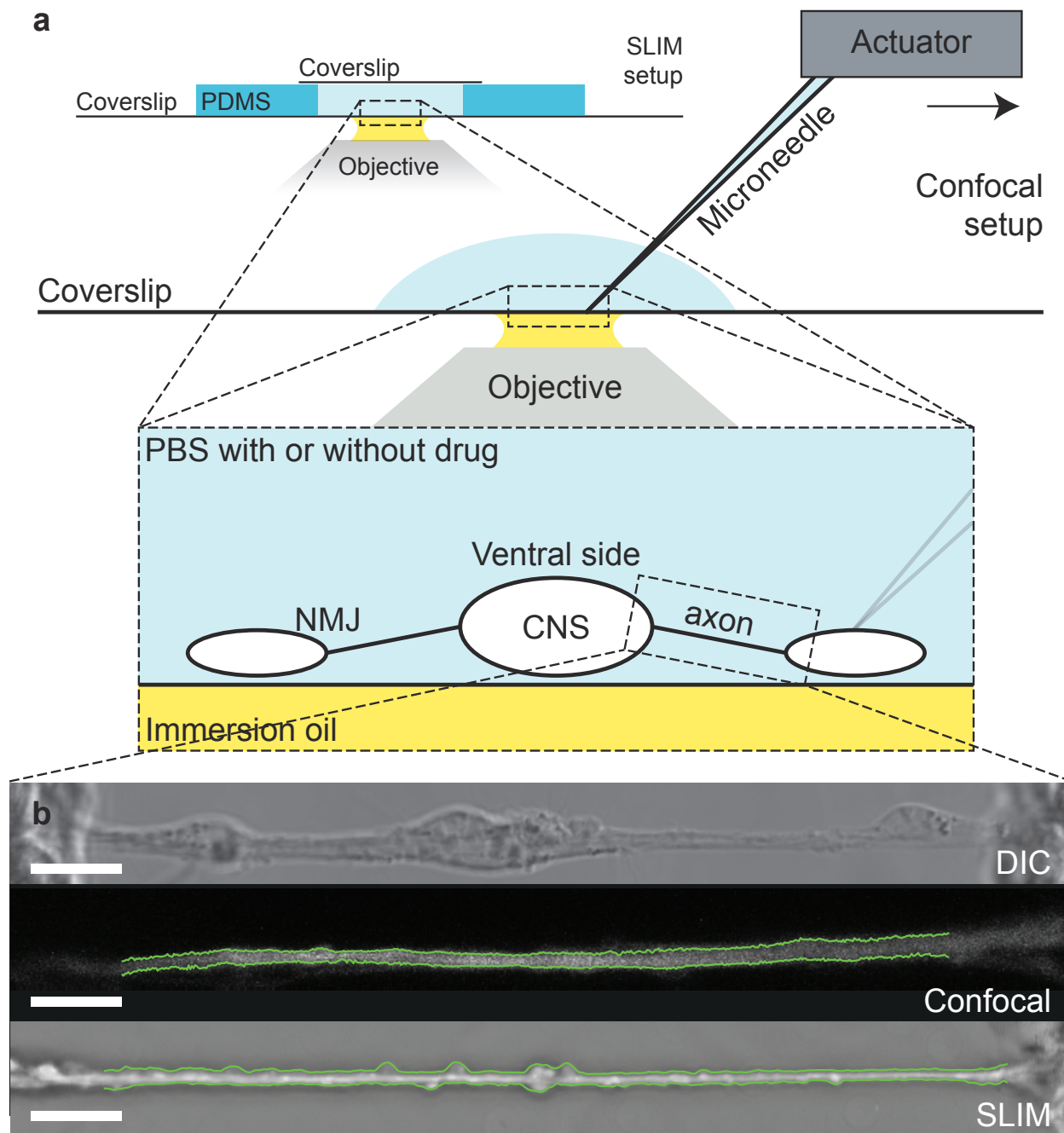
Figure 3.4: Sample preparation and representative images. (a) Cartoon schematic of the experimental setup with both imaging methods. Note that no stretch experiment was carried out in the SLIM set-up due to the top cover slip; stretching manipulations were done exclusively using the confocal setup. (b) (top) DIC image of an axon before cleaning is completed. (center) Maximum-intensity-projected confocal image of a cleaned axon. Green lines labeled the boundaries determined by the analysis algorithm. (bottom) Reconstructed SLIM image of another cleaned axon. Green lines labeled the boundaries determined by the analysis algorithm. All scale bars at 10 microns.

Figure 3.5: Continuous sample plot of diameter data and stretching manipulations. Phase 1: PBS (or drug) treatment of 60 minutes (Fig. 3.7). Phase 2: Stretch to 15-25% strain in less than 1 minute. Drop in diameter due to volume conservation (Fig. 3.10b). Diameter is not monitored. Phase 3: Stretch is held and diameter is traced for 30 minutes (Fig. 3.10c). Phase 4: Unstretch the sample to its original configuration. Axon would first buckle and then contract to a straigh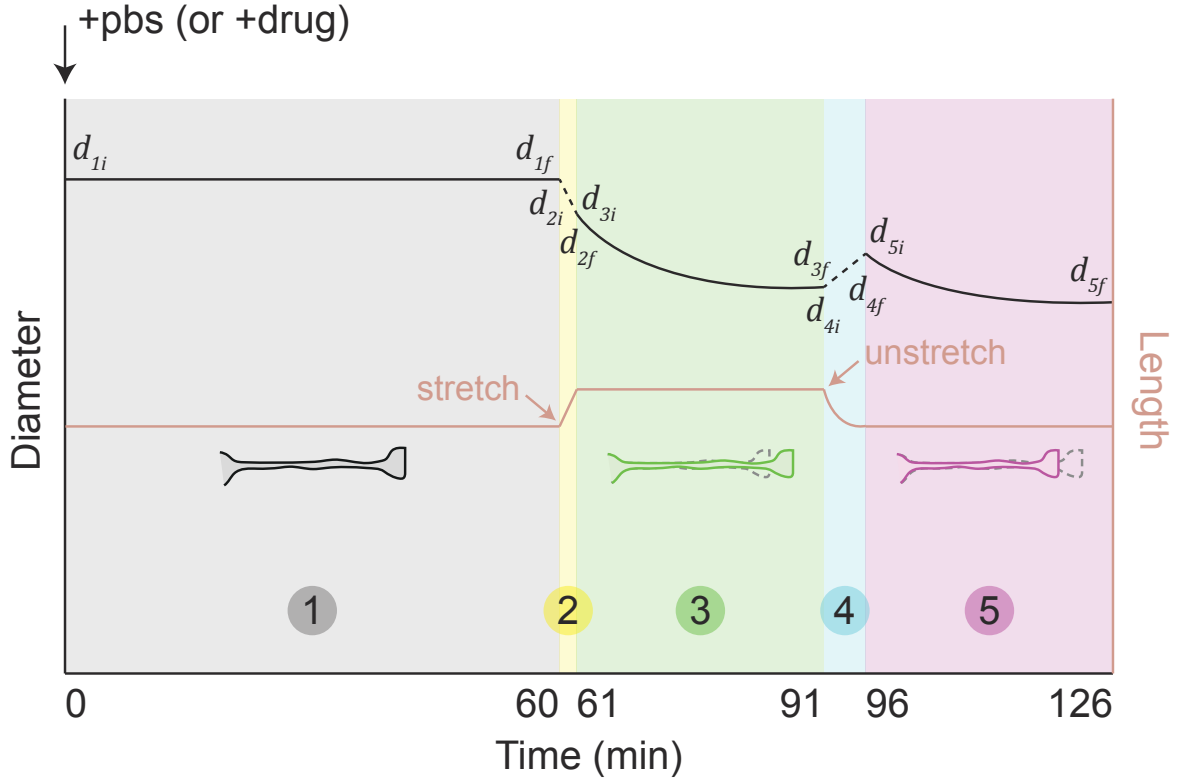t configuration again in 5 minutes. Gain in diameter due to volume conservation (Fig. 3.11c). Diameter is not monitored. Phase 5: Axon rebuilds its rest tension and diameter is traced for another 30 minutes (Fig. 3.11b). Experiements (Fig. 3.10e & 3.11a in main text) not subjected to phase 1 follow identical phases 2 - 5.

Actin maintains a circumferential tension resisted by microtubules

Drugs with known specificity to actin filaments (cytochalasin D, cytoD) and MT (nocodazole and colchicine, noco/colch) were applied to the preparations 3 minutes before imaging commenced. The preparations were monitored under the two imaging modalities for 60 minutes (phase 1 in Fig. 3.5). We measure initial diameter at $d_{1i} = 2.34 \pm 0.44 \ \mu m$ (confocal, N=6) & $3.31 \pm 0.49 \ \mu m$ (SLIM, N=6). This corresponds to at least 20 pixels across the width of an axon (Fig. 3.6). We estimated that our gaussian fitting measurements should be accurate for at least 0.5 pixels. This gives a resolution of around 2.5%. The diameter changes were largely consistent between the two modalities (confocal imaging and SLIM). Disrupting actin

filaments (Fig. 3.7a & b, red) led to an increase in average diameter (confocal: $d_{1f}/d_{1i} = 1.11 \pm 0.02$, $N = 8$; SLIM: $d_{1f}/d_{1i} = 1.12 \pm 0.04$, $N = 3$), and disrupting MT (Fig. 3.7a & b, blue) led to a decrease in average diameter after 60 minutes of drug treatment (confocal: $d_{1f}/d_{1i} = 0.87 \pm 0.05$, $N = 6$; SLIM: $d_{1f}/d_{1i} = 0.92 \pm 0.02$, $N = 3$). Control cases with PBS incubation (Fig. 3.7a & b, grey) showed a small increase (confocal: $d_{1f}/d_{1i} = 1.01 \pm 0.02$, $N = 6$; SLIM: $d_{1f}/d_{1i} = 1.04 \pm 0.01$, $N = 3$) and slight fluctuations within our estimated accuracy of 2.5%. Spatial examination also revealed that diameter increase caused by actin disruption was consistent along the entire length of each axon (Fig. 3.8).

To test whether contractile forces are involved in diameter regulation, we treated the axons with myosin II disrupting drugs, Y-27632 and ML-7. These drugs were found to reduce contractility of axons along the longitudinal direction [55]. We observed diameter increase when axons were treated with Y-27632 (confocal: $d_{1f}/d_{1i} = 1.12 \pm 0.05$, $N = 3$; SLIM: $d_{1f}/d_{1i} = 1.16 \pm 0.08$, $N = 3$) and ML-7 ($d_{1f}/d_{1i} = 1.12 \pm 0.06$, $N = 3$) respectively (Fig. 3.7b & c). This implies that relaxation of tension results in increase in diameter.

Although the final magnitude of diameter increase (under cytoD or Y-27632 treatment) is similar between the 2 modalities, the time constant is not. We believe this can be attributed to the imaging and analysis methods used. In confocal imaging, the GFP signal comes from a membrane bound protein expressed only in neurons. While in SLIM, the contrast is derived from the content of the axons. Furthermore, we used a curve fitting algorithm in analyzing the data from confocal imaging to minimize noise, and such was difficult to realize in SLIM because of the many local intensity peaks. Previous work suggests that actin filaments are sensitive to cytoD treamtent in less than 10 minutes [62], which is what we observed in confocal imaging.

These observations can be explained by contractility of actomyosin machinery along the circumferential direction of axons (Fig. 3.7d). When actin filaments/myosin II are disrupted, the circumferential tension is diminished. This leads to an imbalance of cell pressure and membrane tension, and, as a result, an inflation in diameter (and volume). On the other hand, when MT are disrupted, the polarity of the imbalance switches since there are now less restoring force against contractile actin leading to reduction in diameter. This proposition is interestingly similar to the case of axial axonal tension [55], leading to our speculation that tension could be coupled in the axial and circumferential directions.

SLIM imaging revealed that the average phase (p) increased ($p_f/p_i = 1.19 \pm 0.20$, $N = 3$) when actin was disrupted (Fig. 3.7e, red). Average phase remained unchanged (colch: $p_f/p_i = 0.97 \pm 0.11$, $N = 3$; Y-27632:
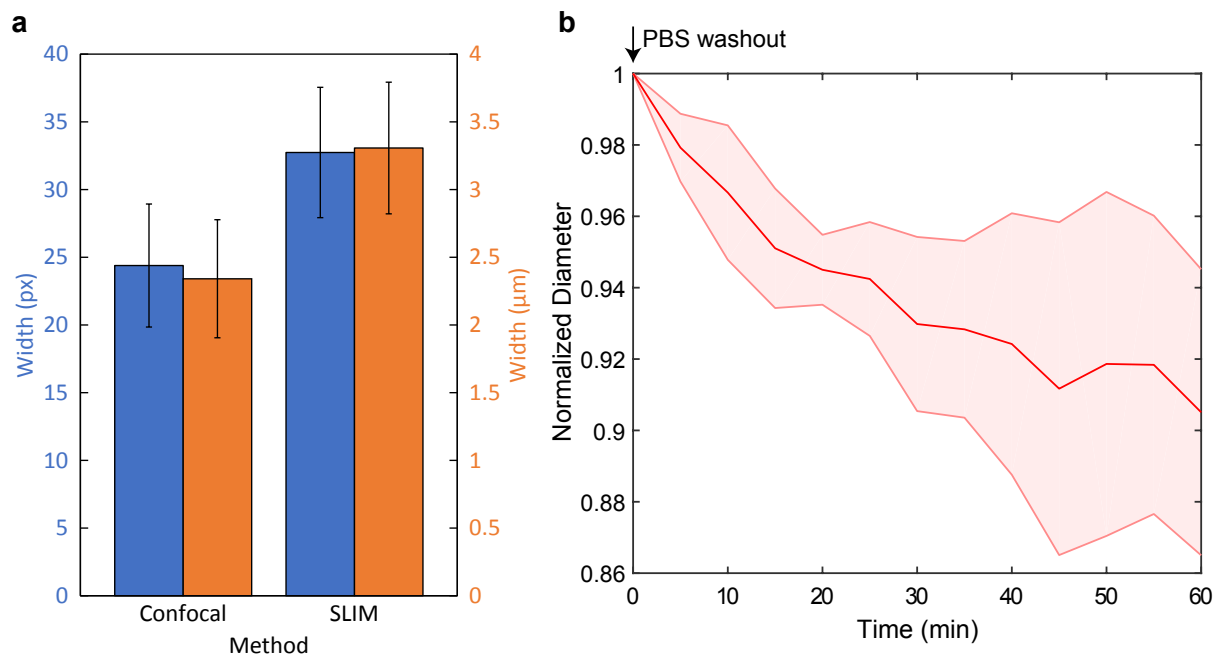
Figure 3.6: (a) Axon diameter in microns and pixels as measured by confocal and SLIM respectively. (b) Axons incubated under cytoD for 60 minutes before subjected to a pbs washout. Data depict diameter immediately after the washout. All shaded regions indicate error bar in standard deviation.

$p_f/p_i = 0.95 \pm 0.08$, $N = 3$) upon MT disruption (Fig. 3.7e, blue) or Y-27632 treatment (Fig. 3.7e, cyan). As phase correlates with mass density [63], this suggests that the content that left upon MT disruption had similar density on average to the remaining content in the axon, while the new mass that had come in due to the inflation in diameter upon actin disruption was denser on average. Increase in diameter caused by Y-27632 did not lead to an influx of denser mass. This suggests that an inflation in diameter alone is not sufficient to cause the influx of denser mass; actin depolymerization is necessary.

The increase in phase upon actin disruption led us to investigate any side effects that CytoD itself might have caused. Upon a subsequent washout, axons that were treated with CytoD revert back to their original diameter (Fig. 3.6b). This suggests that CytoD did not cause any detrimental effect on axons permanently.

We further perform an analysis to understand the nature of the heavier mass coming in upon diameter inflation. We compared the normalized phase distribution of axons before and after cytoD treatment and identified a continuous range that led to the reported increase in average phase (Fig. 3.9a). The pixels that fell within the identified range show structures that resemble vesicles (Fig. 3.9b).
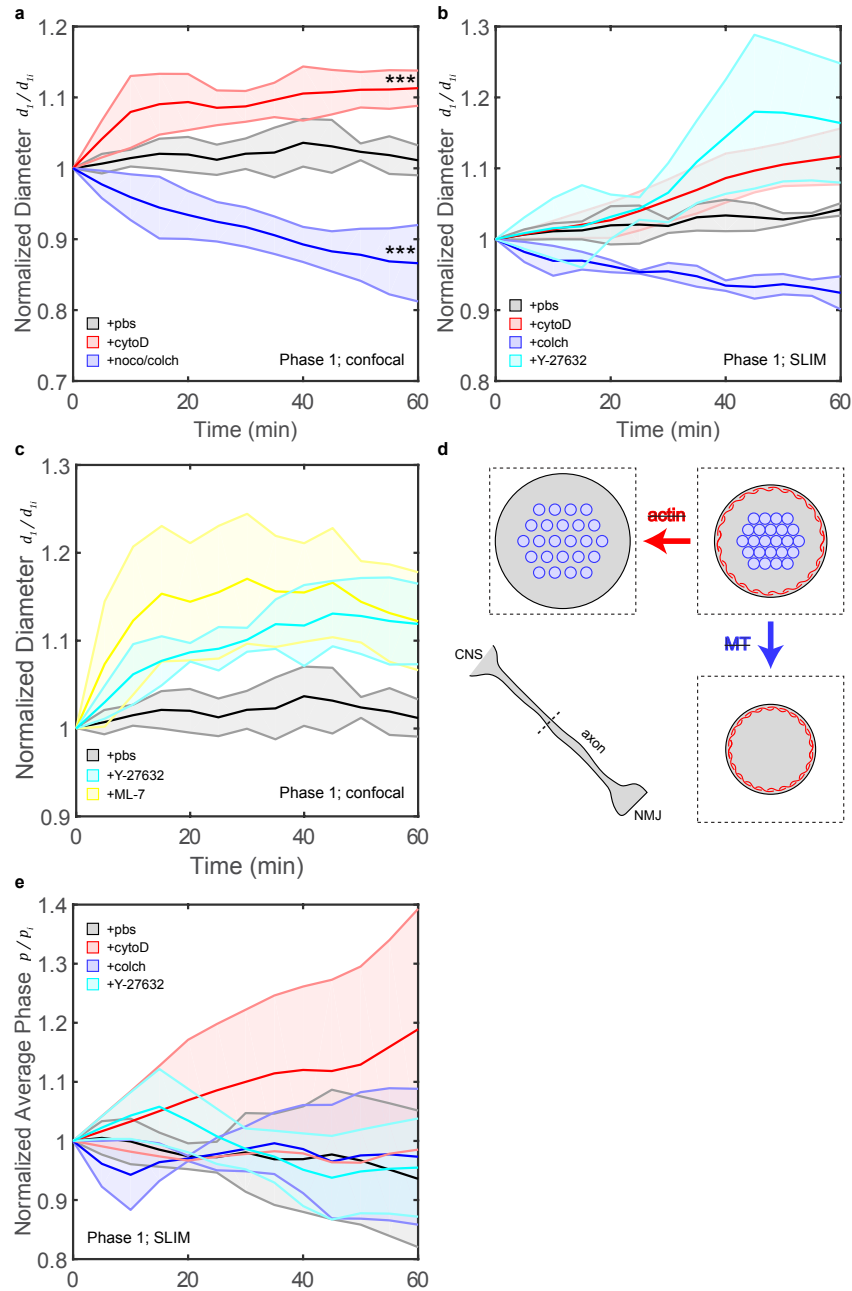
Figure 3.7: Diameter changes under drug treatment. (a) Confocal and (b) SLIM measurements of average diameter over time of axons treated with PBS (grey), cytoD (red), noco/colch (blue), and Y-27632 (cyan). (c) Confocal measurements of average diameter over time of axons treated with PBS (grey), Y-27632 (cyan), and ML-7 (yellow). (d) Cartoon schematic of the proposed explanation. Figures (in dotted boxes) depict cross-section, as indicated by the dotted line in the bottom left figure, of axons under different conditions. Red network represents actin filaments, and blue circles indicates MT. When actin filaments, and therefore circumferential tension, are disrupted, a dilation in diameter (and volume) occurs. This can potentially cause MT to become less compact. When MT are disrupted, actin filaments have less resistance to compact resulting in a smaller diameter (and volume). (e) Average phase measured by SLIM of axons treated with pbs (grey), cytoD (red), colch (blue), and Y-27632 (cyan). The average density of the cytoplasm and the cytoskeletal components increase with time with disruption of actin, but not with MT. All shaded regions indicate error bar in standard deviation. Unpaired two-sample t-test used to obtain p-values.

a   axon with decreasing diameter

0.2 μm

5 μm

smoothed

b   axon with increasing diameter

0.2 μm

5 μm

smoothed

— Just after manipulation
— 15 minutes after manipulation
— 30 minutes after manipulation
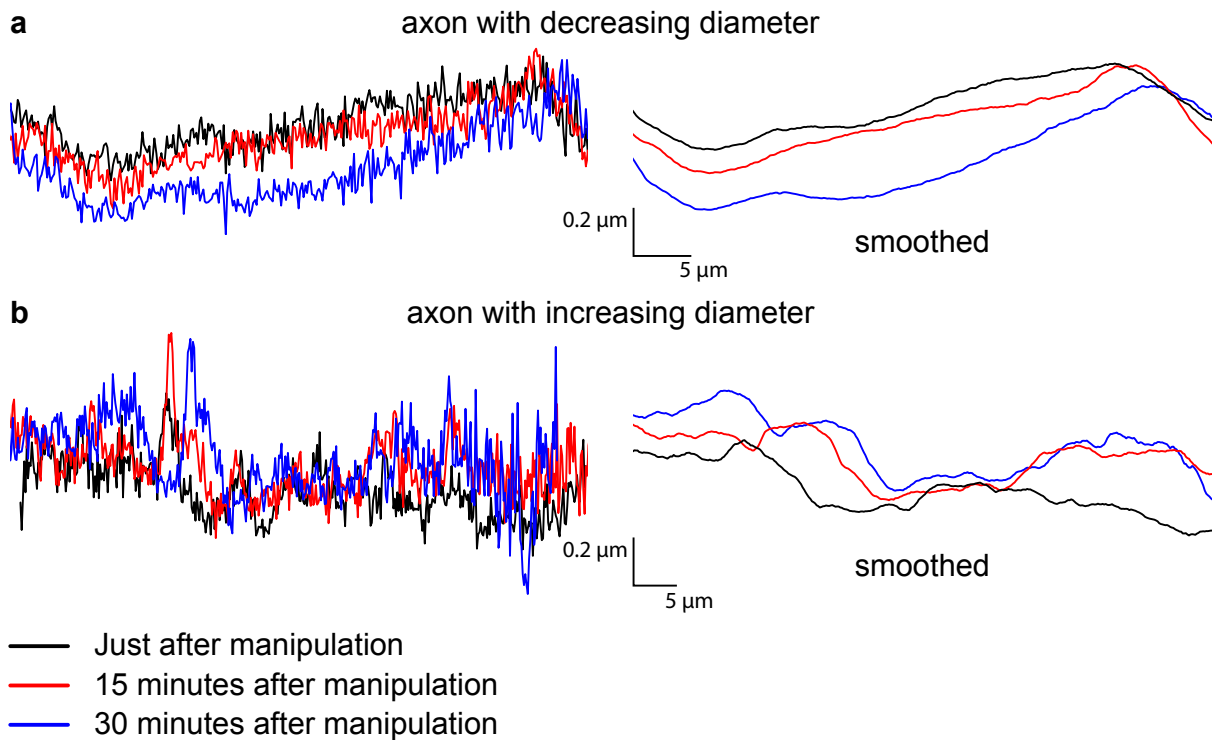
Figure 3.8: Spatial changes of axon diameter. Sample confocal diameter data of an axon (a) with decreasing diameter and an axon (b) with increasing diameter due to mechanical stretch and cytoD treatment respectively. The plots are colored (given in the legend) according to the time (0, 15, 30 minutes) after the manipulation. Diameter changes in either direction happen along the entire length of the axon. This is better visualized when the raw data is smoothed (right, 50 points moving average). Both axes have units in microns.
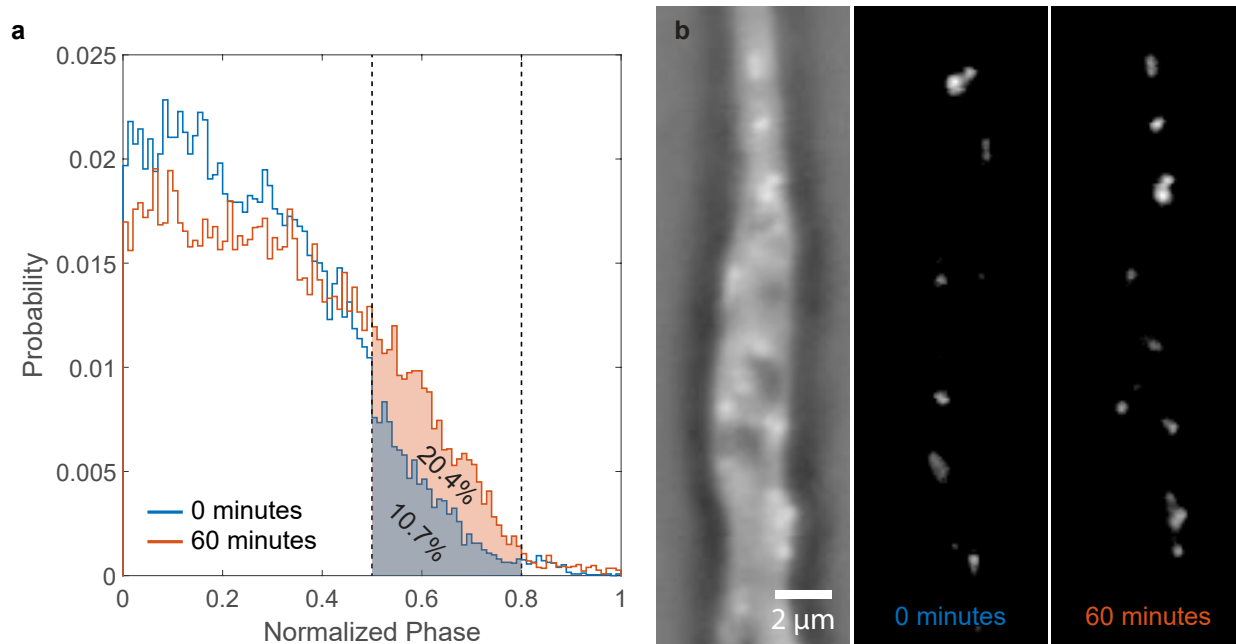
Figure 3.9: Analysis of axons with phase increase. (a) Phase histogram of axons before (blue) and after (red) cytoD incubation. Pixels are sorted into 100 equal bins according to their normalized phase values $\hat{p} = \frac{p}{p_{max}}$. The y-axis is reported in probability instead of frequency for comparison purposes. Sum of probabilities is equal to 1 in both blue and red curves. Only pixels determined to be inside the axons by the algorithm previously described are used. The 2 dotted lines at $\hat{p} = 0.5$ and 0.8 respectively indicate the range of phase values of the new mass coming in. The total probability of phase values that fall inside the region of interest is reported for both time points. (b) An axon among the group was selected randomly, and only pixels with $0.5 \leq \hat{p} \leq 0.8$ are shown. The resulting structures have vesicle-like morphology.

Table 3.1: Comparison of local strain, global strain and d_{2f}/d_{2i} in Phase 2

Sample	Global Strain	$(1+\epsilon_{2,glo})^{-\frac{1}{2}}$	Local Strain	$(1+\epsilon_{2,loc})^{-\frac{1}{2}}$	d_{2f}/d_{2i}
1	25.8%	0.891	24.0%	0.898	0.888
2	21.2%	0.908	19.2%	0.916	0.912
3	13.1%	0.940	13.3%	0.939	0.945

Axonal volume is conserved under fast stretch

To further examine whether axial and circumferential tension are coupled, we applied extra tension to the axon by stretching it (15-25% strain) from the NMJ side using a micro-pipette tip connected to a piezo-actuator (phase 2 in Fig. 3.5).

During initial fast stretch, mass flow in or out of axons is limited and volume should be conserved. We verified such conservation of volume during initial stretching by comparing theoretical diameter ratios to experimental values. Given the definition of strain (ϵ) as $\frac{\Delta l}{l}$, the stretch ratio (λ) is defined as:

$$\lambda = \frac{l}{l_0} = \frac{l_0 + \Delta l}{l_0} = 1 + \epsilon. \tag{3.1}$$

The volume ratio for an axon modeled as a cylindrical rod is then:

$$\frac{V_{2f}}{V_{2i}} = \frac{d_{2f}^2 l_{2f}}{d_{2i}^2 l_{2i}} = \frac{d_{2f}^2}{d_{2i}^2}\lambda. \tag{3.2}$$

If volume is conserved, then volume ratio ($\frac{V_{2f}}{V_{2i}}$) is 1. The diameter ratio (d_{2f}/d_{2i}) is then:

$$\frac{d_{2f}}{d_{2i}} = \frac{1}{\sqrt{\lambda}} = (1 + \epsilon)^{-\frac{1}{2}}. \tag{3.3}$$

Using Eq. 3, we can test volume conservation by comparing diameter and strain. Two strain measurements were used. One, termed global strain, traced the two ends of the axon. The other, termed local strain, traced two clearly identifiable points along the axon (Fig. 3.10a). The results for one axon are shown in Fig. 3.10b. We find, the diameter ratio is almost equal to $(1 + \epsilon)^{-\frac{1}{2}}$ for both local and global strains. Thus Eq. 3 is satisfied experimentally, implying volume conservation. The close agreement between local strain and global strain suggests that the axonal strain is uniform along its length. In addition, it suggests that mechanical elastic properties of the axon is also uniform along its length. Data from three samples are shown in Table 3.1.

Circumferential tension from actin filaments reduces axon diameter overtime when a mechanical stretch is held

We monitor diameter changes for 30 minutes with the stretch held fixed (phase 3 in Fig. 3.5). The diameter continued to decrease ($d_{3f}/d_{3i} = 0.88 \pm 0.06$, $N = 6$) for axons treated with PBS (Fig. 3.10c, green). This trend was not observed ($d_{3f}/d_{3i} = 1.00 \pm 0.04$, $N = 6$) in axons with actin filaments disrupted (Fig. 3.10c, red). A smaller decrease was observed ($d_{3f}/d_{3i} = 0.93 \pm 0.03$, $N = 6$) in axons with MT disrupted (Fig. 3.10c, blue). The reduction of diameter upon a sustained stretch, again, occurred along the entire length (Fig. 3.6). Thus volume of the axon under sustained stretch reduced in PBS and with MT disruption, but not with actin disruption.

Previous studies have shown that upon fast stretching, axial tension increases instantaneously, and then slowly relaxes (due to viscoelastic response to the applied tension) to a state that is more tensed (around 3-fold at 60 % strain) than that prior to any stretch (rest tension) [12]; i.e., axial tension increases after stretch. This, together with our results that stretching led to diameter reduction (circumferential tension increases) driven by actin filaments, again suggests that axial tension and circumferential tension could be coupled.

We hypothesized that the actomyosin-driven reduction in diameter under sustained stretch was mainly due to the breakage of MT upon sudden mechanical stretch [26], creating space for actin filaments to contract further. This is supported by the similar diameter reduction in MT-disrupted unstretched axons in phase 1 and untreated stretched axons in phase 3 (Fig. 3.7a, blue vs. Fig. 3.10c, green). In addition, the smaller reduction in diameter in stretched axons with MT previously disrupted (Fig. 3.10c, blue) compared to untreated ones (Fig. 3.10c, green) further supports the argument; in these cases, MT had been disrupted and already resulted in a diameter reduction in phase 1. To test this hypothesis, staining experiments were performed to show the reduction of polymerized tubulin upon stretching (Fig. 3.10d).

Furthermore, as a control against prolonged saline incubation during phase 1, we performed stretching manipulations on a few axons immediately after embryo surgery. The observed diameter reduction showed no significant differences compared to that after 60 minutes of PBS incubation (Fig. 3.10c & e, green). Diameter reduction was not observed in axons not subjected to any stretch (Fig. 3.10e, grey) similar to results in Fig 3.7a & b.
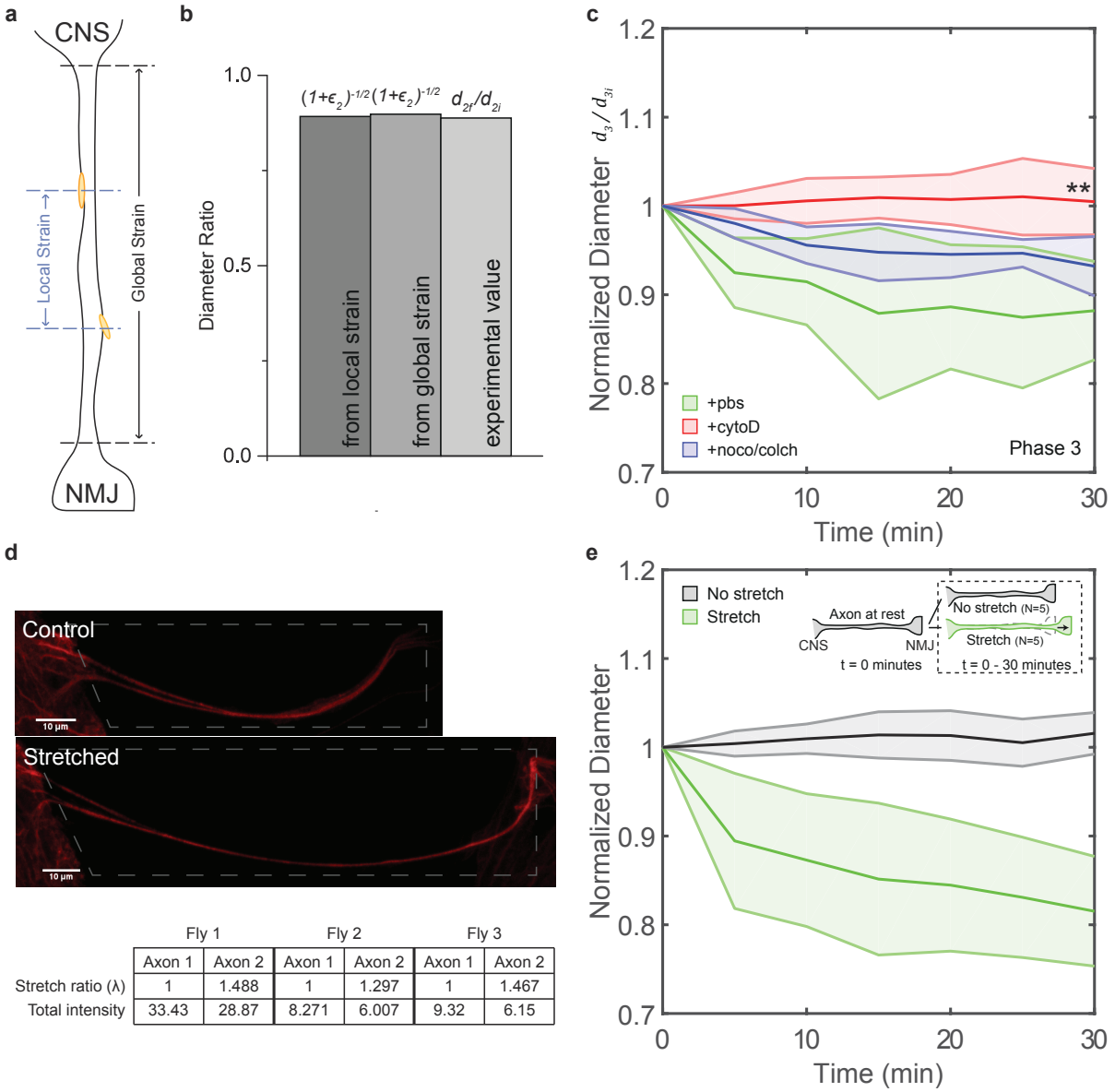
Figure 3.10: Diameter reduction driven by actin filaments upon a sustained stretch. (a) Cartoon schematic describing the concept of local strain (between 2 visible markers) and global strain (between 2 ends). (b) Diameter ratios as calculated from local and global strain and observed from experiment. (c) Diameter of axons held at prescribed stretch (15-25%) under PBS (green), cytoD (red) and noco/colch treatment (blue). (d) Two neighboring axons with similar length are cleaned per embryo. One is stretched (bottom) and the other is left unperturbed (top). Stretch is held for 30 minutes, after which MT staining is performed. The total fluorescence intensity (intensity sum over all pixels within the bounded 3D region) after background subtraction, which measures the amount of MT in each axon, is quantified and compared. Stretch ratio defined in Eq. 1. Total intensity shown in arbitrary unit. (e) Axons imaged immediately after embryo surgery with (green) or without (grey) stretch applied. Inset cartoon depicts the two processes. All shaded regions indicate error bar in standard deviation. Unpaired two-sample t-test used to obtain p-values.

Circumferential tension from actin filaments reduces axon diameter when axon is returned to initial configuration

After the stretch was held for 30 minutes, some axons were brought back to their initial configuration. We called this process "unstretch" (phase 4 in Fig. 3.5). The axons first buckled when subjected to the unstretch process. They then slowly contracted to straighten again. Note that axons treated with cytoD do not fully contract, as also observed in other studies [55], because actin-myosin contractility is hampered. For all instances, we waited 5 minutes after which their length did not visibly change. Axons left stretched served as control (Fig. 3.11a).

We then continued to monitor the diameter for another 30 minutes (phase 5 in Fig. 3.5). We called this phase "restore" for those axons returned to their taut, straight configuration. Previous studies have shown that axons build up significant tension [12] that is actin-myosin dependent [55] during this phase. We observed diameter reduction in restored axons ($d_{5f}/d_{5i} = 0.90 \pm 0.02$, $N = 6$), regardless of whether phase 1 had previously been executed (Fig. 3.11a & b, magenta). Diameter did not change in control cases where axons were either never stretched (Fig. 3.11a, grey) or remained stretched without being restored (Fig. 3.11a, green), as explained in the inset of Fig. 3.11a. Reduction in diameter was significantly hampered ($d_{5f}/d_{5i} = 0.97 \pm 0.02$, $N = 5$) in axons with actin filaments distupted (Fig. 3.11b, red).

However, axons with MT disrupted (Fig. 3.11b, blue) showed no diameter reduction ($d_{5f}/d_{5i} = 0.97 \pm 0.02$, $N = 5$). We expected higher reduction in diameter since MT disruption results in higher longitudinal tension in axons [16, 32], and hence higher circumferential tension if there is coupling. The paradox can be resolved by considering phase 4, in which we waited 5 minutes for the axons to straighten after unstretch. It is known that force-free slackened axons with MT disruption straighten 3 times faster compared to axons with MT intact [55]. Volume conservation requires that soon after straightening diameter ratio increased to $\lambda^{-1/2}$. After straightening, tension built up fast in MT-disrupted axons. Diameter reduced and arrived at a steady value before phase 5 began. This explains our experimental finding of $d_{4f}/d_{4i} < \lambda^{-\frac{1}{2}}$ (Table 3.2 & Fig. 3.11d, blue). Axons not treated with any drugs also straightened before phase 5 commenced. And diameter reduction (relative to the diameter from volume conservation calculations) in phase 4 was also observed in these axons (Table 3.2 & Fig. 3.11d, magenta); the reduction however continued in phase 5. This supports the argument that circumferential tension is coupled to axial tension: disrupting MT has been shown to speed up axial contraction and increase axial tension [55, 16, 32], and here from our measurements we infer that MT disruption can lead to faster circumferential contraction.

Table 3.2: Comparison of global strain and d_{4f}/d_{4i} in Phase 4

Sample	Treatment	Global Strain	$(1 + \epsilon_4)^{-\frac{1}{2}}$	d_{4f}/d_{4i}
1	+noco/colch	-10.9%	1.059	1.019
2	+noco/colch	-14.3%	1.080	0.973
3	+noco/colch	-17.5%	1.101	1.008
4	+pbs	-21.2%	1.126	1.062
5	+pbs	-24.9%	1.153	1.052
6	+pbs	-28.4%	1.182	1.082

We compared diameter reduction as a function of time with the evolution of tension in slackened axon measured previously [12]. Both data sets fitted well to an exponential curve in the form of $Ae^{-t/\tau} + C$ (Fig. 3.11d). Time constants (axial tension: 7.22 minutes; diameter: 7.11 minutes) were extracted from the fits. The time constant for tension development and diameter reduction are comparable, implying a common mechanism generating axial tension and reduction of diameter. This further supports that axial and circumferential tension could be coupled. Note that these time constants are greater than those observed in length shortening of slackened axons [55], because axons continue to apply tension after becoming taut. This does not change the length, but can be captured using a force sensor [12].

3.4   Discussion

In this chapter we explored the biophysical factors that influence axonal diameter in motor neurons of embryonic *drosophila*. We used two independent methods, confocal microscopy and SLIM imaging, to measure axonal diameter. We demonstrated earlier that after synaptogenesis axons tends to contract and hence develop tension along the longitudinal direction. Actin and myosin II are involved in generating the longitudinal tension [55]. Here we show that acto-myosin machinery is involved in generating circumferential tension as well along the entire length of the axon. This tension originates from the contractility of cortical actin, which in turn applies a compressive force on the MT. The force balance between cortical actin and microtubule results in an equilibrium diameter of the axon (Fig. 3.12). Thus, when MT are disrupted, diameter decreases; when actin is disrupted or myosin II is inhibited, diameter increases. We further show that longitudinal and circumferential tension are coupled. They share similar time constants of evolution; i.e., times to generate longitudinal tension and to contract the diameter to their respective steady values are similar. This suggests a common mechanistic origin for both. However, the detailed cytoskele-
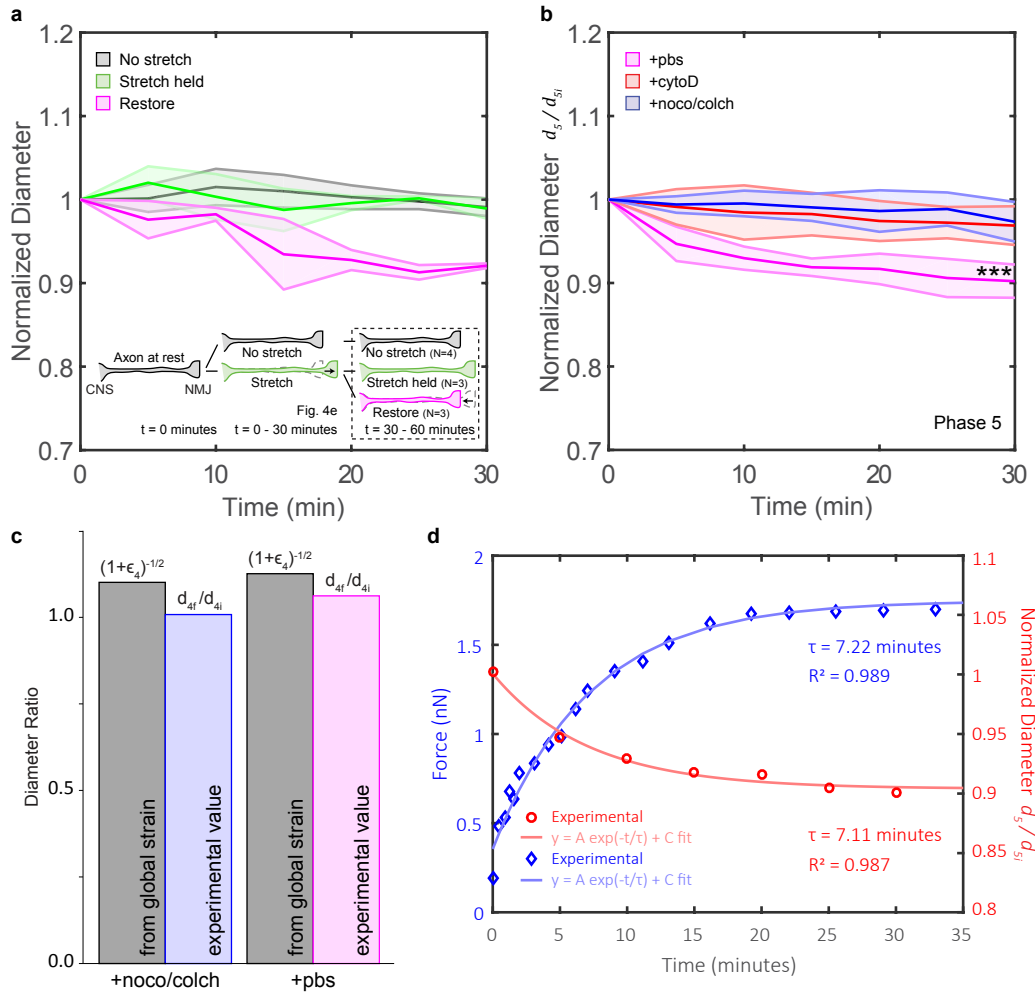
Figure 3.11: Actin-driven diameter reduction upon return to initial configuration. (a) Diameter normalized to the initial value of axons with no stretch (grey), stretch held (green), and stretch restored (magenta). The three processes are described in the inset cartoon: Axons are at rest initially. Some axons are stretched (15-25%) and the stretch is held for 30 minutes. A few axons are then returned to the original configuration. All axons are then monitored for another 30 minutes. (b) Diameter of restored axons subjected to PBS (magenta), cytoD (red), and noco/colch (blue) treatment. (c) Diameter ratios (similar to those in Fig. 3.10b) during phase 4 plotted for 2 axons treated with noco/colch and pbs respectively. The axons are selected for similar $(1 + \epsilon_4)^{-\frac{1}{2}}$. See also Table 3.2. (d) Axial tension of a restored axon in blue (data previously published in Rajagopalan et al. (2010)). Normalized diameter from 5c plotted in red. Both data sets are fitted to an exponential equation (form given in the plot). R^2 and τ values are displayed for comparison purposes. Circumferential, as inferred from diameter reduction, and axial tension have similar temporal dynamics. All shaded regions indicate error bar in standard deviation. Unpaired two-sample t-test used to obtain p-values.
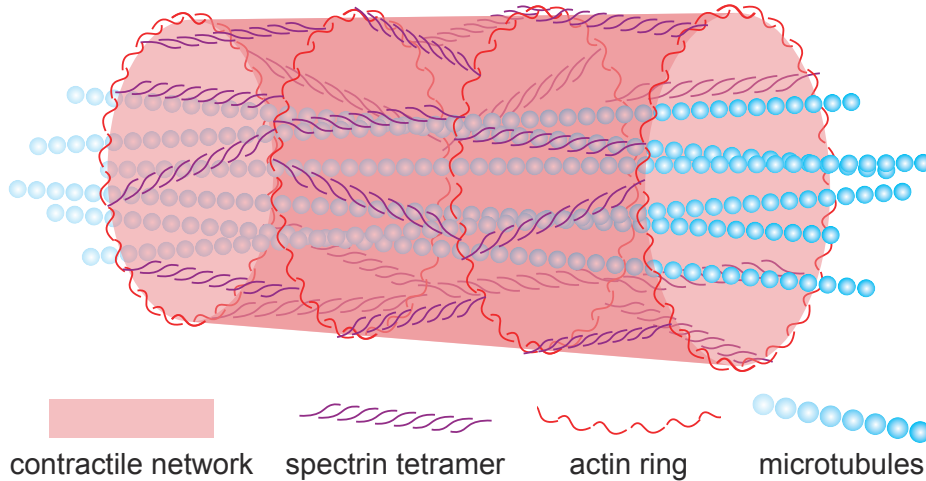
Figure 3.12: Cartoon illustration of the proposed descriptive model. Cortical actin and spectrin form a contractile network. Cytosolic MT provides structural support and act against the axial and circumferential tension generated by the contractile network.

tal architecture that gives rise to the circumferential contractility of embryonic axons remains to be resolved.

Circumferential contractile forces are found in multiple biological processes. For example, actomyosin rings are critical for wound healing [64, 65] and cytokinesis [66, 67]. In both cases, they exert a circumferential tension to do work and drive the dynamics of the processes. Notably, these other rings are much larger in size and can span several cells; they are also more dynamic than those observed in axons [68]. Furthermore, the ring structure of actin has not yet been observed in myelinated axons, except that at the nodes of Ranvier [48]. *drosophila* axons are not myelinated, but glial cells still form an insulating layer around them as early as stage 15 [30]. This limits the ability to super-resolve structure of actin (and other proteins) because of multiple scattering events [48]. Nonetheless, most evidence support the existence of actin ring in peripheral axons. It has been shown that axonal diameter increases when adducin [51], an actin-capping protein that is thought to link the actin and spectrin in the periodic membrane skeleton, is disrupted; it is unclear though how adducin can help regulate diameter. The present work provides new insights to the mechanism by which actomyosin network can maintain structural integrity and regulate shape of axons—through the coupled axial and circumferential tension.

It is important to note that we used change of diameter of axons and the effect of force relaxing drugs to infer circumferential tension, given that force and deformation (change of diameter) are related through

44

Table 3.3: Comparison of axial tension and circumferential tension inferred from diameter changes

Treatment	Stretch state	Axial tension	Reference	Diameter	Cir. tension
PBS	No	No change	[12, 55]	No change	No change
cytoD	No	↓	[16, 32]	↑	↓
noco/colch	No	↑	[16, 32]	↓	↑
PBS	Stretch	↑	[12]	↓	↑
cytoD	Stretch	?		No change	No change
noco/colch	Stretch	?		↓	↑
PBS	Restore	↑	[12, 55]	↓	↑
cytoD	Restore	No change	[55]	No change	No change
noco/colch	Restore	↑	[55]	↓	↑

the cytoskeletal elasticity of the axons. Since these material properties are not known, we cannot quantify the circumferential forces. There is no direct means available to measure circumferential tension. The nano-Newton force probe used to measure longitudinal force of the axons [2] could not be used to measure circumferential force. However, our data supports a model where longitudinal and circumferential tensions are coupled (Table 3.3), although the precise nature of this coupling remains elusive.

Our SLIM experiments demonstrated that mass displaced during diameter reduction (following MT disruption) did not change the density of the axon. Images from electron microscopy show that axons are MT-rich [47]. These 2 observations together suggest that the displaced mass is composed of depolymerized MT and their associated proteins. Mass that entered the axon during diameter dilation after actin disruption, on the other hand, had higher density and resulted in new structures with vesicle-like morphology based on our phase histogram analysis. One plausible explanation is that these new structures were originally vesicles scaffolded by an actin-rich network in the presynaptic terminal [69], which upon actin disruption, are released into the axon. Yet, we cannot exclude the possibility of vesicles/cargo from other sources. Channels gating and vesicles fusion can also regulate mass; it has been shown that membrane tension provided by actin dynamics is a key factor in these processes [65, 70]. We, however, did not observe exocytosis/endocytosis events in our experiments, which could be due to insufficient spatial-temporal resolution.

The reduction in diameter under stretch might seem counterintuitive to normal development, since one would expect the axon to increase its diameter during development. In fact, several *in vitro* experiments have shown that axons, when towed, would grow both axially and laterally [71, 57]; the growth is dependent on new MT formation [72]. In these studies, however, the stretch is imposed slowly and gradually

throughout the course of the experiment, while in our case the time from no stretch to full stretch (120% of original length) is usually in less than a minute. This seems to suggest that stretching with different strain rates can result in different MT dynamics; i.e., when stretch is applied at a higher rate than the polymerization process, MT can break and subsequently disassemble [26], which occurs at a faster time scale [73].

Axonal diameter is a physiologically relevant parameter, since conduction speed of action potential along the axons scales with the diameter for both healthy and pathological neurons [74]. Nerve atrophy results in reduction of axonal diameter and a corresponding reduction in conduction speed. Hence, significant effort has been directed to measuring axonal and nerve diameter using multiple methods including electron microscopy [75], and diffusion MRI [76]. However, how axons maintain their diameter has gained limited attention. This work reveals a biophysical mechanism that maintains the diameter.

Chapter 4

A device to apply chemical treatment to a particular segment of an axon

This chapter is adapted from a previous publication[1].

4.1   Motivation

Fluid flows at small scale are generally laminar (low Reynold's number), where neighboring streams mix at the interface only by diffusion leading to a mixing rate much slower than the flow rate. This facilitates separation of fluids without the use of any physical barrier. This phenomenon has been exploited extensively in microfluidic systems allowing a wide range of biological studies, including cell counting and sorting [77, 78], high-throughput [79] and drug screening devices [80], gene expression [81, 82], and cellular manipulations [83, 84].

One particular application of microfluidics is the exposure of a part of single living cells *in vitro* to various drugs. One method termed partial treatment of cells using laminar flows (PARTCELL) [85] demonstrated that disruption of cytoskeleton could be achieved in a portion of a single bovine endothelial capillary cell, and was used to track intracellular mitochondria movement by labeling mitochondria in a specific part of the cell [85].

PARTCELL was extended to study temperature gradient in whole *drosophila* embryos using two laminar streams at different temperatures [86]. The study demonstrated that embryos were able to adapt to and counteract unnatural ambient environment. In larger organisms, perfusion studies were performed through the capillary system of the organisms themselves [87, 88]. In these examples, however, cellular/subcellular scale processes could not be addressed.

A major unmet challenge in microfluidics to date is the lack of control on samples. This is due to the fact that microchannels are prepared first. The cells or other suspendable samples are flown into the channels next and subsequently adhere to the channel floor. But their attachment location and orientation cannot be controlled. One needs to search for a sample along the length of the channels that can be subjected to the

---

[1]Fan A, Tofangchi A, De Venecia M, Saif MT. A simple microfluidic platform for partial treatment of insuspendable tissue samples with orientation control. Lab Chip. 2018

appropriate laminar streams. This lack of control on sample choice and sample placement with respect to the flow direction has restricted the type of preparations that can be used for biological studies. Previous methods using laminar streams are therefore limited to samples that can be suspended in saline, and are adherent to the device substrate when allowed to [85, 86]. These limitations on sample preparations and choices can be resolved by reversing the sequence of fluidic device fabrication and sample preparation, i.e., by mounting microfluidic device onto the already prepared sample such that samples do not have to be transferred into the device.

Following this strategy, here we developed a simple microfluidic device that enabled us to perform partial treatment of single embryonic *drosophila* axons *in vivo*. The sample (dissected embryo with exposed axons of motor neurons) was first placed on a glass substrate where it attached to naturally. The microfluidic device was then placed on the substrate such that the flow direction was orthogonal to the axons. The device adhered to the substrate with sufficient strength, and did not detach when tested with exaggerated flow conditions. We devised a scheme such that the device can be filled completely, while keeping the samples constantly under a saline environment. A simple method was designed to measure the apparent adhesion strength to allow for the selection of appropriate base material. Using the device and the experimental set-up, we exposed part of single axons of mutant *drosophila* embryos to specific drugs. We demonstrated that blockage of voltage-gated sodium channels can lead to calcium events and membrane hyperpolarization, and that inhibition of myosin II at the proximal segment of axons can lead to vesicle declustering at the distal presynaptic terminal. Such studies could not be performed using conventional microfluidic devices where the dissected embryos would need to be flown unharmed into the channels with no control on their adherence to the floor or their orientation.

4.2   Materials & Methods

Device fabrication

Microfluidic devices were made from a liquid silicone rubber (LSR; Bluestar LSR-4305), and, for comparison, 10:1 polydimethylsiloxane (PDMS; Sylgard 184). A mold was used to cast the device. The mold was designed in a CAD software (SOLIDWORKS; Dassault Systèmes, Vélizy-Villacoublay, France), exported to an stereo lithography apparatus 3D printer (Viper SI; 3D systems, Rock Hill, SC), and printed with WaterClear Ultra 10122 (Somos, Elgin, IL). LSR and PDMS were poured into the mold and left incubated overnight at 60 °C. Blunt needles (21027A; Hamilton, Reno, NV) were punched into the silicon polymer to form inlets. Two-part epoxy (Loctite, Düsseldorf, Germany) was used to secure the needles. The inlets (Fig. 4.1a) were

connected to syringe pumps (NE-300 & NE-1000; New Era, Farmingdale, NY) through flexible tubings.

Device characterization

To visualize the surface defects of the devices, a scanning electron microscope (6060LV; JEOL, Tokyo, Japan) was used. Gold/palladium coatings were performed to make the surfaces conductive for electron microscopy. We measure the stiffness of the device material (LSR/PDMS) using a nanoindentor (Piuma; Optics 11, Amsterdam, Netherlands), with a probe stiffness of 4.1 N/m; the load vs displacement curve obtained was fit to the Hertzian model to extract the Young's Modulus (Fig. 4.4a). To determine the apparent adhesion of the device, we intercalated a glass bead (250 μm; 59202; Sigma, St. Louis, MO) between the silicone device and a glass substrate (12-545H; Fisher Scientific, Hampton, NH) and measured the delamination length between the substrate and the polymer induced by the bead. Some glass substrates had been incubated with human fibronectin (33016015; Fisher Scientific, Hampton, NH) at 50 μg/mL for 1 hour to achieve fibronectin coating.

Drosophila Culture

Transgenic *drosophila* (6923, 8760, 51056, 58763) were purchased from Bloomington Stock Center (Bloomington, IN). Single axons were exposed using microsurgery from stage 16 embryos following established protocols [20, 55].

Pharmaceutical Drug

Y-27632 (110 μM; Cayman Chemical, Ann Arbor, MI) were used to inhibit the ROCK pathway. Dimethyl sulfoxide (DMSO; D8418; Sigma, St. Louis, MO) was added as a solvent and was maintained at a final concentration of less than 1%, tested to have no observable effect [55]. Tetrodotoxin (TTX, 500 nM; T-550; Alomone Labs, Jerusalem, Israel) were used to block voltage-gated sodium channels (Na_v). All drugs were diluted in Ca^{2+}/Mg^{2+} free PBS.

Imaging

The embryos were inspected using a widefield inverted microscope (IX81; Olympus, Tokyo, Japan) with standard GFP and mCherry filter cubes (GFP-3035D & mCherry-B; Semrock, Rochester, NY) connected to a fluorescence source (X-Cite 120PC Q; Excelitas Technologies, Waltham, MA) and a CMOS camera (C11440; Hamamatsu Photonics, Hamamatsu, Japan). Fluorescence images were obtained with an exposure of 200 ms though a 20x lens (LCPlanFI; Olympus, Tokyo, Japan) unless otherwise specified.

4.3   Results

Device assembly and basic concept

The device, made of PDMS or LSR, had multiple inlets connected to a chamber (Fig. 4.1a). The chamber (200μm deep) was connected to a waste well. We devised a way to place a *drosophila* embryo inside the chamber (Fig. 4.1b) without disturbing delicate features (Fig. 4.1c). The procedure was as follows:

1. We prepared a surgically exposed drosophila embryo under a small amount of saline on a glass slide (Fig. 4.2i).

2. To form a closed environment, the device was laid on top of the glass slide with the embryo inside the chamber (Fig. 4.2ii). The device was oriented in such a way that the axons were perpendicular to the flow direction to achieve partial perfusion.

3. We gently tapped on the device to facilitate a better seal.

4. A saline bridge would form between the glass floor and the chamber ceiling initially (Fig. 4.2iii).

5. By leaving a droplet of saline at the edge of the waste well (Fig. 4.2iv), we allowed capillary action to drive saline to back fill the chamber until no gas was left in where the chamber and the waste well met (Fig. 4.2v).

6. We then added extra saline to the waste well (Fig. 4.2vi) and applied suction through the center channel to allow saline to back fill the entire chamber (Fig. 4.3i).

7. We then flowed the intended solutions through the side channels one at a time, while keeping a constant net backward flow by increasing the center suction flow (Fig. 4.3ii–v).

Following this process, all channels and the entire chamber were filled without any residue gas (Fig. 4.3vi), which was when one can start an experiment; this process typically took less than 5 minutes.

In our preparations, the embryos adhered well naturally to the glass surface. While the concept of the device can certainly be extended to other types of sample, testing is recommended to make sure that the intended sample will stay stable under the filling and perfusing processes possibly—if necessary—by using adhesives, surgical pins, or custom made apparatus[89].

An alternative to PDMS improves substrate adhesion and device performance

Most microfluidic devices are formed by functionalizing two or more layers of material (e.g. glass and PDMS) through some manipulations (e.g. oxygen plasma) and subsequently allow the two surfaces to
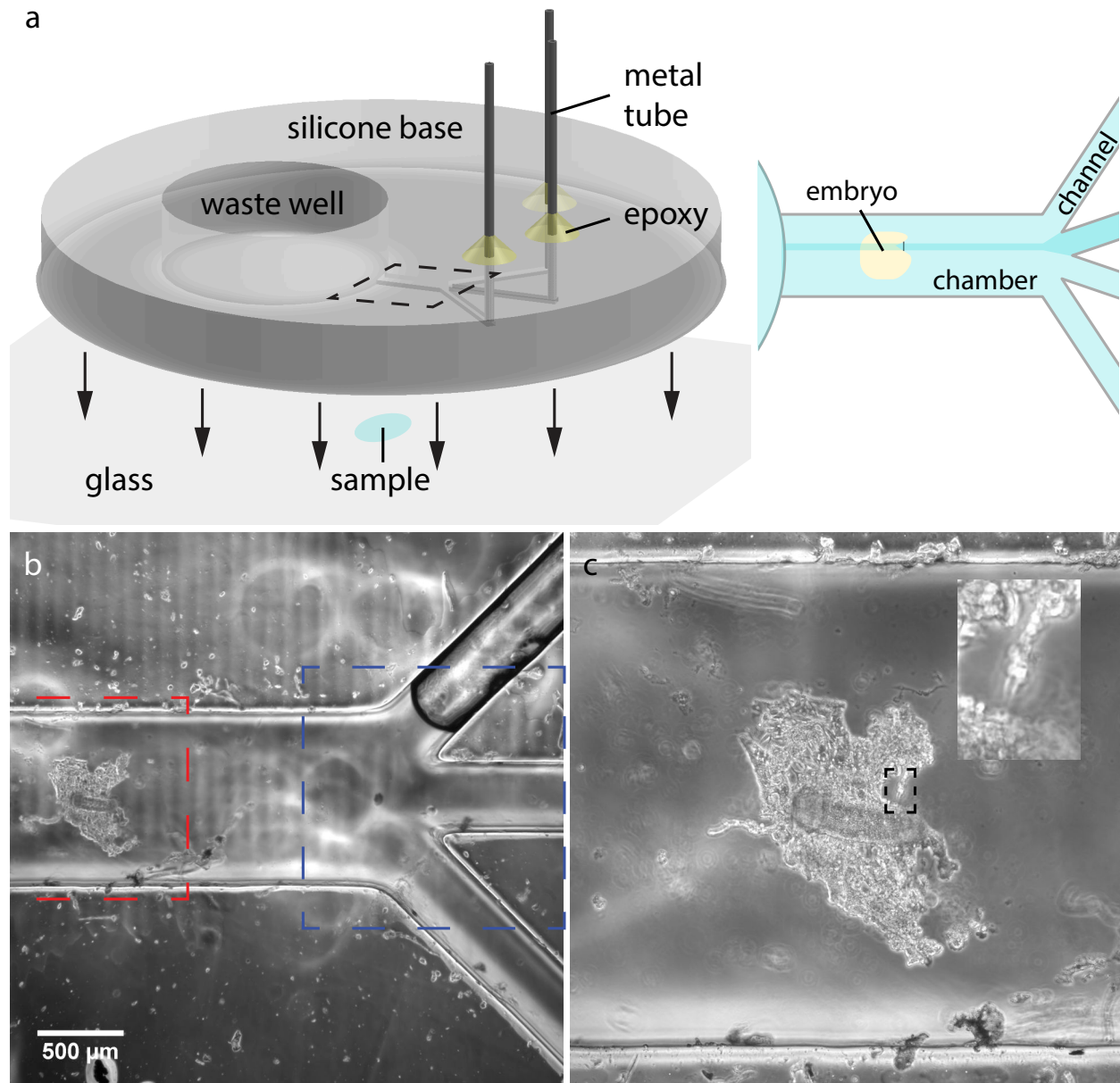
Figure 4.1: Device schematics and representative images. (a) Cartoon schematic and illustration of the device. Three or four channels are depicted, but the device can have more channels. The device is directly mounted onto the glass substrate holding the sample. (b) An image of the channels and the chamber with a drosophila embryo in it. Notice the air trapped in the top channel. We have devised a way, shown in Fig. 4.8, to remove all the air inadvertently trapped during device assembly. Content in the blue box is shown in details in Fig. 4.8, and the red box is enlarged in Fig. 4.1c. (c) Expanded view of the embryo. Inset figure shows the preservation of delicate features, in this case an exposed axon from microsurgery.
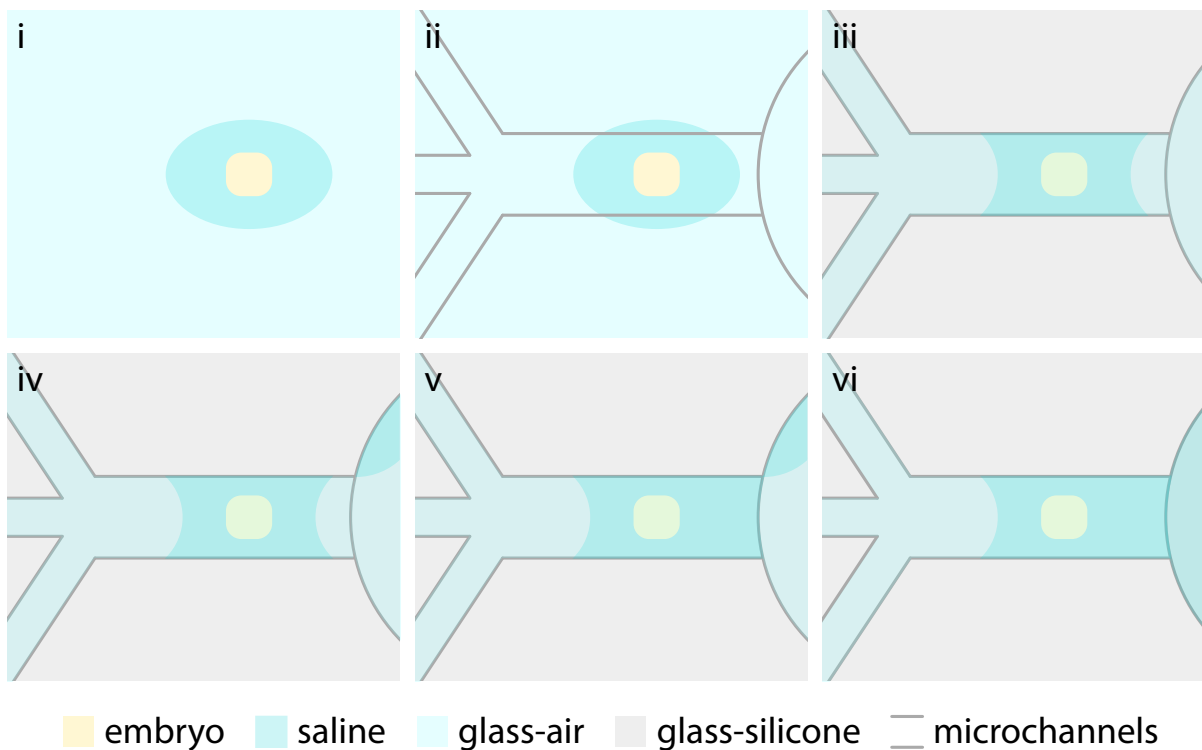
Figure 4.2: Device sealing process. (i) An embryo is under saline on a glass slide. (ii) The device is positioned with a microscope such that the embryo is inside the chamber. (iii) By placing the device on top of the glass, natural adhesion will seal the channels and the chamber. A saline bridge is formed between the glass and the device. (iv) Small amount of saline is placed at the edge of the well without blocking the chamber such that air can vent. (v) Capillary action will draw the saline into the chamber and the chamber will fill. (vi) Saline is added to the well to prepare for suction backfill.
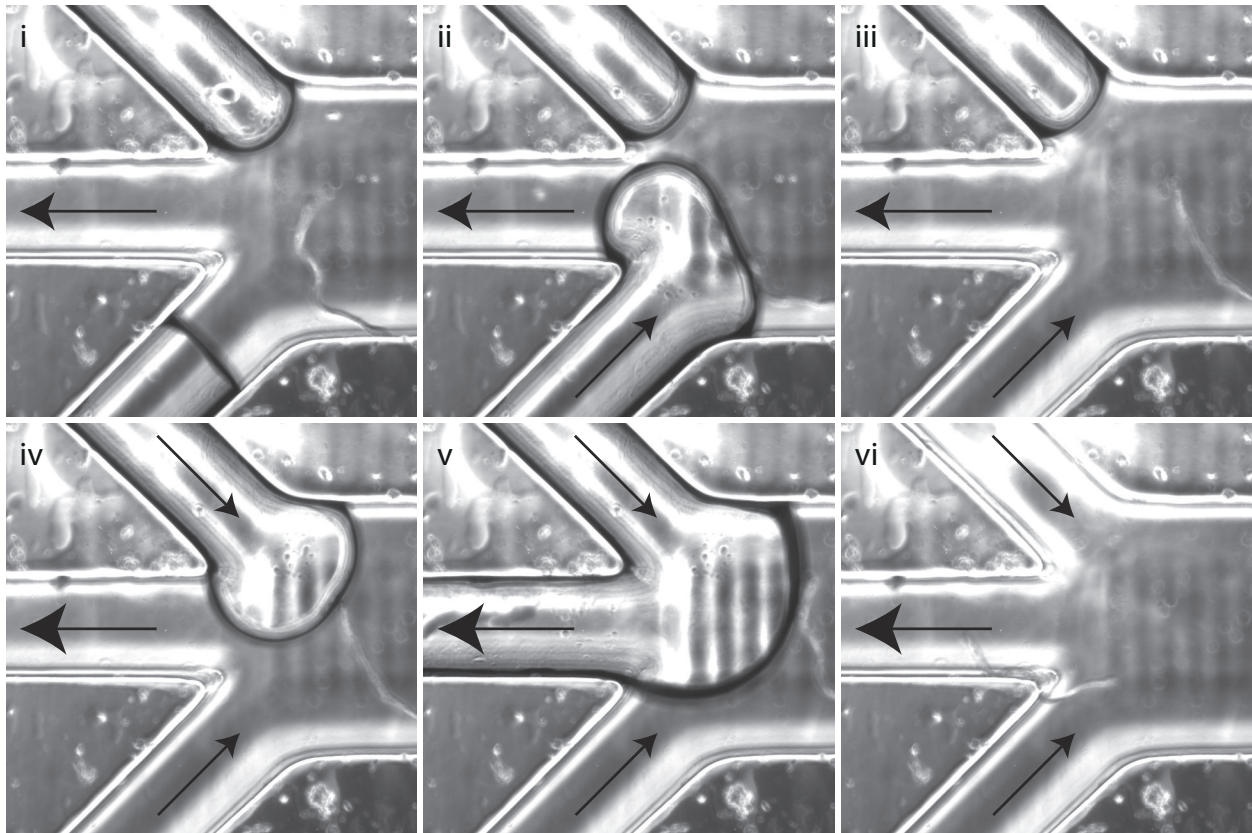
Figure 4.3: Device filling process. (i) A suction is applied in the center channel to backfill the chamber. (ii) A smaller flow in introduced in the bottom channel so that air trapped inside the channel will leave through the center channel. The sunction in the center is increased to compensate for the extra volume introduced by the bottom channel to maintain a net backward flow. (iii) Bottom channel filling is completed. (iv-vi) The same procedure is repeated for the top channel. The center suction is increased again to compensate for the extra volume.
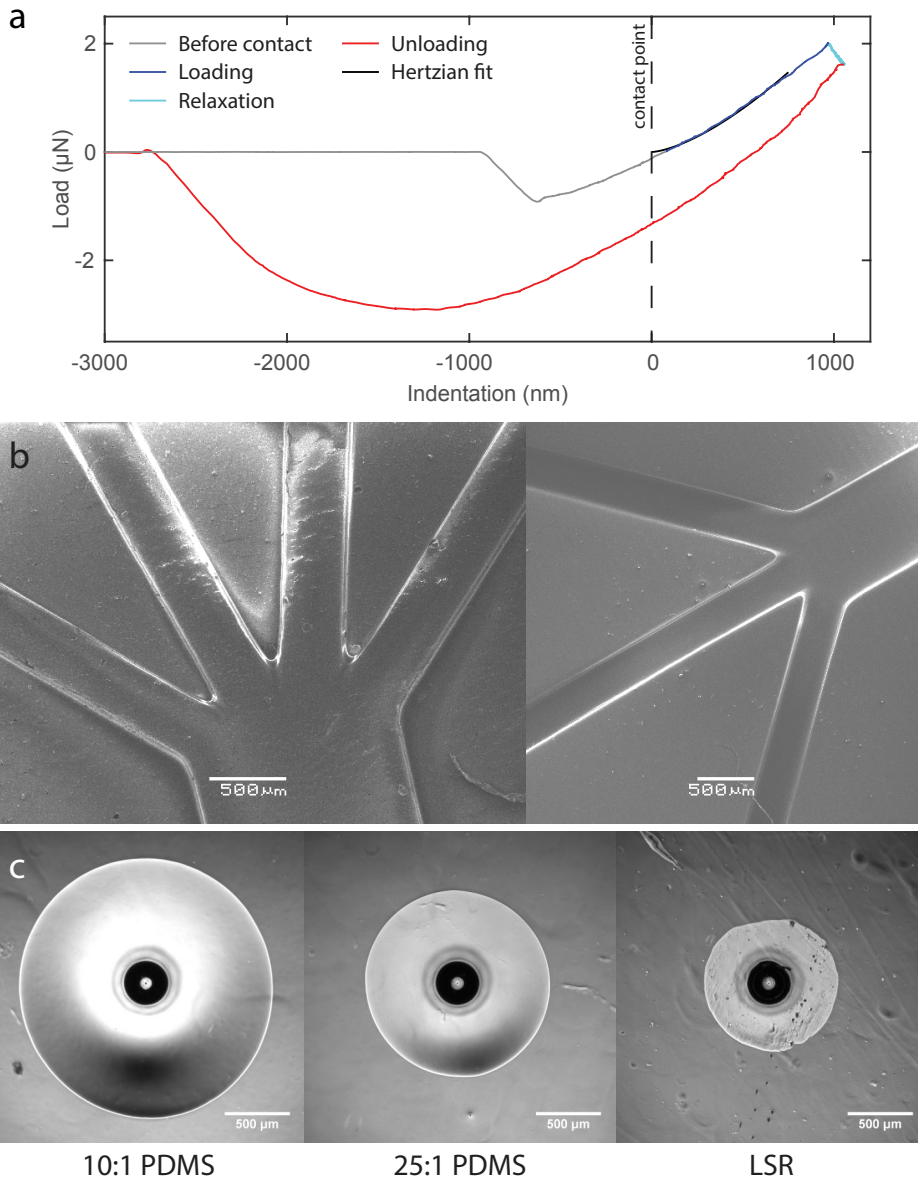
Figure 4.4: Device material characterization. (a) A sample nano-indentation curve. Loading data just after the contact point are fitted to the Hertzian model to extract the stiffness of the material. Negative load during the approach phase is due to surface adhesion. (b) SEM images of an LSR device with 4 channels and a PDMS device with 3 channels. (b) A bead is placed between the material of interest and a glass substrate. The delamination radius is much more pronounced with 10:1 PDMS (left) and 25:1 PDMS (center) compared to LSR (right). Device thickness and image size are the same.

bond for a period of time [90, 91]. This allows a very stable interface that can be used for culturing and studying adherent cells over an extensive period. In our case, however, it is necessary to rely on natural adhesion [92, 93], because artificial bonding requires chemical/physical modifications to the surface that would inevitably influence the physiological properties of the sample as well [94].

Therefore, it was important to use a material that adhered well to glass, and was soft enough to overcome any surface defects. PDMS was one good candidate. We further selected LSR, a material previously employed in elastomer actuator [95]. SEM images (Fig. 4.4b) were obtained for both materials to confirm that features on the mold were replicated. Some surface wrinkles were observed, but they did not seem to affect the seal (Fig. 4.4b). We used a bead intercalation method to measure the apparent adhesion of LSR/PDMS to glass (Fig. 4.5a). The size (radius) of the induced delamination is determined by the competition between the interfacial adhesion energy and the elastic energy of the polymer [96]. The delamination radius between LSR and glass due to the bead was half the corresponding radius for PDMS (0.511 ± 0.062 mm vs 1.059 ± 0.052 mm; Fig. 4.5b & 4.4c). The delamination diameter (radius$\times$2) also served as an estimate of the chamber width above which the chamber ceiling would remain collapsed once adhered to the glass floor. For this reason, the chamber width was designed to be smaller than the delamination diameter.

To determine if LSR's better conformability was due to its compliance alone since it is 3 times softer than PDMS (0.403 ± 0.033 MPA vs 1.72 ± 0.14 MPA; Fig. 4.5c), we also compared it to PDMS fabricated in a 25:1 base-to-agent ratio. The ratio 25:1 was selected to render its stiffness (0.313 ± 0.011 MPA) slightly lower than LSR's (Fig. 4.5c). If compliance alone explains LSR's conformability, then we should see a smaller delamination radius with 25:1 PDMS. This was however not the case (0.680 ± 0.066 mm; Fig. 4.5b). We therefore concluded that LSR has stronger surface interactions with glass and would achieve better sealing in our device.

Using the same method, we further tested glass substrates that were coated with fibronectin (FN) to see if the adhesion strength would be compromised when a extracellular matrix (ECM) protein coating was present. No significant differences in delamination radius (1.094 ± 0.137 mm) were noticed when PDMS was mounted onto the coated glass substrate (Fig. 4.5b). This suggests that the direct mounting method can be used on FN-coated glass, and potentially with other ECM proteins. However, if a certain protein weakens the adhesion significantly, one can use patterning methods to coat only the channels region of the substrate, allowing bare glass to interact with the soft polymer to form a stable seal.
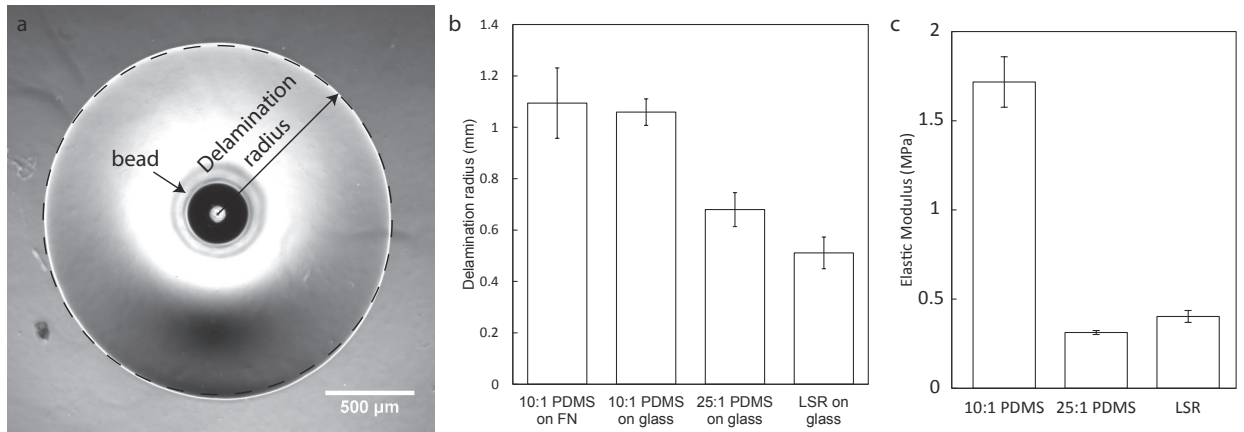
Figure 4.5: Device material characterization. (a) A bead is placed between the material of interest and a glass substrate. A blister (indicated by the dotted line) with form as a result and the delamination radius can be used to measure adhesion energy. (b) Delamination radius comparison among 10:1 PDMS on FN-coated glass (N=8) and 10:1 PDMS (N=6), 25:1 PDMS (N=6), and LSR (N=10) on glass. The radii are obtained by fitting a circle to the edge reported by the Canny edge detection method. (c) Stiffness comparison among 10:1 PDMS (N=6), 25:1 PDMS (N=6), and LSR (N=6) based on a Poisson's ratio of 0.5.

Device validated for different flow conditions—short-term at high rate & long-term at normal rate

To ensure that the seal will stay intact under extreme conditions, LSR devices with 3 channels were tested using a high flow rate (5 μL/min per channel) for 40 minutes and a normal flow rate (0.5 μL/min per channel) for 16 hours in each channel simultaneously. The glass-water-silicone triple line at the inlets (formed due to the insertion of the metal tubes; Fig. 4.1a) resulted in a ring-like edge that was traceable to investigate delamination of the device during pressurized flow (Fig. 4.6a). Image sequences of the delamination propagation were resliced and bandpass-filtered to identify local intensity minimum for edge tracing (Fig. 4.6b). This was performed for every quadrant of the circular edge, and the results were averaged. Two samples were tested under the high-flow condition (Fig. 4.6c), which showed a stable delamination propagation of around 200 μm, approximately one-sixth of the radius of the initial delamination. Three samples were tested under the normal-flow condition (Fig. 4.6c); none of them showed any significant delamination.

Our perfusion experiments in the demonstrations to follow usually lasted for around two hours, thus saline recycling was not necessary. In cases where saline recycling is important for long duration perfusion [18, 89], oxygen supply could become a concern. The speed of the flow should also be carefully considered. A flow rate with which enough new saline is supplied to limit diffusion and tissue deterioration, while keeping the flow laminar and the sample and device stable, should be used.
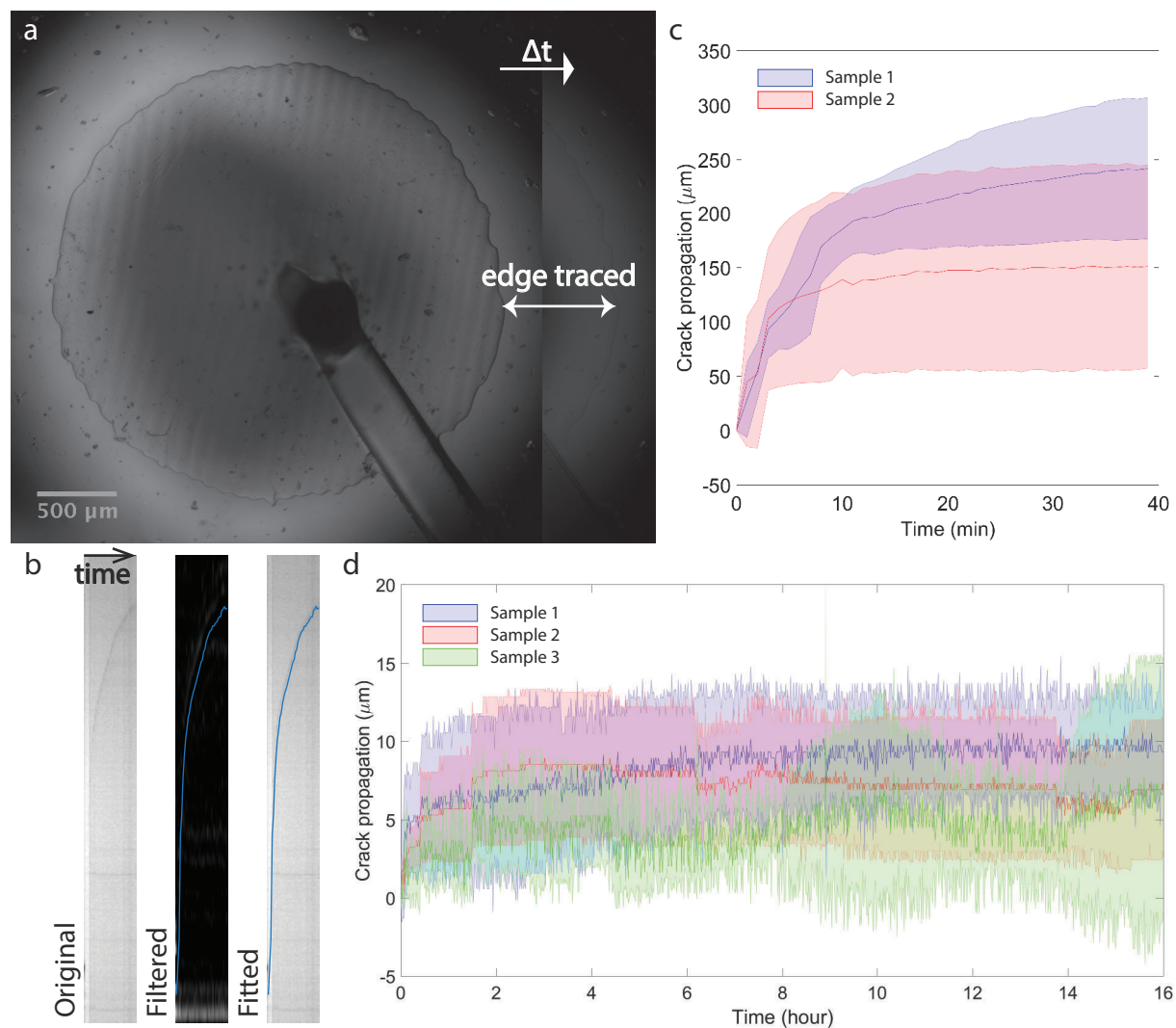
Figure 4.6: Device validation under 2 different flow conditions. (a) Image of an inlet of a device before perfusion (left) and during perfusion (right). Notice the advance of the triple line formed by glass-air/water-silicone. (b) The triple line is traced by first reslicing a time-lapse image sequence along the normal direction of the edge. The resulting image is bandpass filtered such that positions of local minima along the time-axis can be identified. The position vs. time profile is used as the time trajectory of the delaminating crack. One such analysis is performed for each quadrant of the ring edge. (c) Crack propagation under high flow rate ($5\mu L/min$) for 40 minutes in all 4 quadrants are averaged and plotted in 2 samples. Shaded areas show the standard deviation. (d) Crack propagation under normal flow rate ($0.5\mu L/min$) for 16 hours in all 4 quadrants are averaged and plotted in 3 samples. Shaded areas show the standard deviation.

$\frac{x}{x+y}$	Flow position (μm)	
	Set 1: $x + y = 20$ μL/min	Set 2: $x + y = 100$ μL/min
0.1	144.1	136.3
0.2	214.8	218.1
0.3	292.1	295.9
0.4	377.1	369.9
0.5	467.9	477

Table 4.1: Resulting flow positions at different flow rate ratios $\frac{x}{x+y}$ of experiment set 1 & 2 respectively.

Device can achieve partial treatment resolution down to 3% of chamber width

Flow positioning (both width and location) could be controlled by simply adjusting the volumetric flow rate of each channel, since the width ratios are theoretically directly proportional to the flow rate ratios—a property of viscous flow. In practice however, it is uncertain how fine the resolution can be because of variations in flow rates, channel/chamber imperfections, and other physical phenomena like diffusion. The accuracy and resolution of the device comes down to the answer to 3 questions: 1) How narrow can the center flow be? 2) How accurate is the positioning of the center flow? And 3) how stable is the position of the center flow over time? To address these questions, we performed experiments that varied the side channels flow rate, x & y (with units μL/min). The center flow was controlled at 0.5 μL/min, and contained a food dye that fluoresced in red (Fig. 4.7a).

Questions 1 can be addressed by setting $x = y$, and allow them to increase until no further flow width reduction is observed. Using this approach, we realized a center flow width of around 20 μm at $x = y = 50$ μL/min (Fig. 4.7b). The flow width was measured by fitting a Gaussian curve (G) to the intensity profile; the distance between the 2 points where $G'' = 0$ was defined as the width [97].

To validate the device's ability to position the center flow at different locations, we performed 2 sets of experiments that varied the flow rate ratio ($\frac{x}{x+y}$) similarly from 10% to 50%, but the total flow rates ($x + y$) were 20 μL/min and 100 μL/min respectively. The images obtained from each set were combined to one image by maximum intensity projection (Fig. 4.7c). The intensity profile of the combined image was obtained across the width of the chamber (Fig. 4.7d). The data were then smoothed to identify local maxima (Fig. 4.8a–b)—which provided the position of the flows (Table 4.1). The flow positions were further verified by sample autocorrelation (Fig. 4.8c–d). The flow positions from the 2 sets were then plotted against each other (Fig. 4.7e); this ensured that the results were controlled against geometric irregularities introduced by the fabrication process. The positions agreed between the 2 sets (Fig. 4.7e), demonstrating the ability to place the center flow accurately.

The stability over time of the flow position also influences the resolution of the device. To account for

such, we set $x = y = 50$ μL/min and monitored the flow over a 2-hour period. The flow position was computed for every minute and plotted against time (Fig. 4.7f). We observed fluctuations about the mean that resembles a normal distribution (Fig. 4.8e) with a standard deviation of 4.24 μm, adding around 8 μm to the resolution of the device. This resulted in a combined resolution of around 30 μm—sufficient for partial cell perfusion in many applications (Fig. 4.8f). The tested device had a chamber width of 1 mm, resulting in a 3% resolution. A chamber with a smaller width should further lead to better absolute resolution.

The employed methodology did not account for any out of focus light since we used a widefield microscope. Fluorescence light from out of focus plane will scatter and result in a larger width measurement. We therefore believe the resolution reported is an overestimate.

Demonstration 1: Inhibition of voltage-gated sodium channels (Na_v) promotes calcium influx

To observe calcium dynamics, we studied mutant embryos with a calcium sensor CaMPARI [98] expressed only in neurons under GAL4/UAS control (Fig. 4.9a). CaMPARI is excitable by blue light and emits green light in its native state. In addition, it is photoswitchable by ultraviolet light to a state that is excitable by green light and emits red light—but only under elevated concentration of calcium ions [98]. We took advantage of this property of CaMPARI to visualize calcium dynamics under Na_v inhibition using tetrodotoxin (ttx). We observed an increase in red fluorescence but not in green fluorescence in the neurons that were under ttx perfusion (Fig. 4.9b & 4.10). No changes were observed in either channel in the neurons under regular saline perfusion. This seems to suggest that, similar to previous studies [99], Na_v blockage could lead to an influx of calcium ions to the cytosol (as suggested by the increase in red fluorescence) that subsequently get removed (as suggested by the unchanged green fluorescence) either by ion pumps or calcium uptake in organelles (e.g. mitochondria).

Demonstration 2: Inhibition of Na_v modulates membrane potential

Using ttx again, we perfused embryos expressing ArcLight [100, 101], a membrane potential sensor, in neurons under GAL4/UAS control (Fig. 4.11a). ArcLight fluoresces green under blue illumination when there is a membrane potential. Its fluorescence intensity scales with the potential[100, 101]; i.e., a hyperpolarization event would lead to an increase in fluorescence, and vice versa. Neurons under ttx perfusion showed a small increase in intensity after 2 hours of perfusion (Fig. 4.11b–c), while neurons under normal saline perfusion showed smaller changes (Fig. 4.11c & S4†). This seems to support that Na_v blockage could lead to weak membrane hyperpolarization, as previously reported [102, 103].
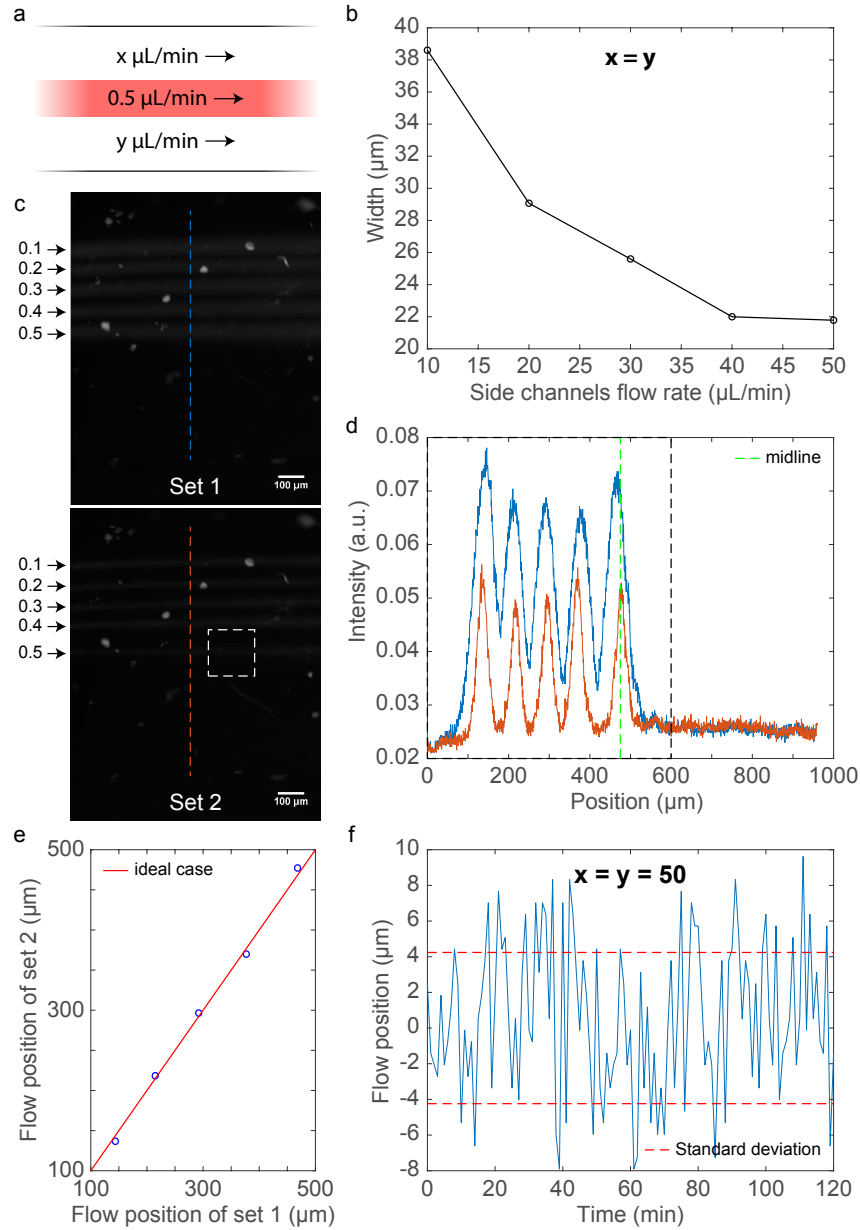
Figure 4.7: Device accuracy and resolution validation. (a) An illustration of the experiment. (b) Width of the center flow as side flow rates ($x = y$) increase. Width reduced down to around 20 μm. (c) Maximum intensity projection of images from experiment set 1 & 2 respectively at flow rates and flow ratios stated in Table 4.1. The blue and red dotted lines indicate the location of the intensity profile shown in (d). The region enclosed in the white box is shown in Fig. 4.8f. (d) Intensity profile of the projection images in (c). Green dotted line indicates the location of the chamber midline. Data enclosed in the black box are further smoother and plotted in Fig. 4.8a–b. (e) Obtained flow positions from set 1 & 2 (Table 4.1) are plotted against each other. Red line indicates the ideal scenario where the positions are equal. (f) Side flow rates set to 50 μL/min and center flow imaged for 2 hours. The position of the center flow is traced. The mean center flow position is subtracted from the data set such that the data fluctuate around a mean of zero. Red line shows the standard deviation of the position data set.
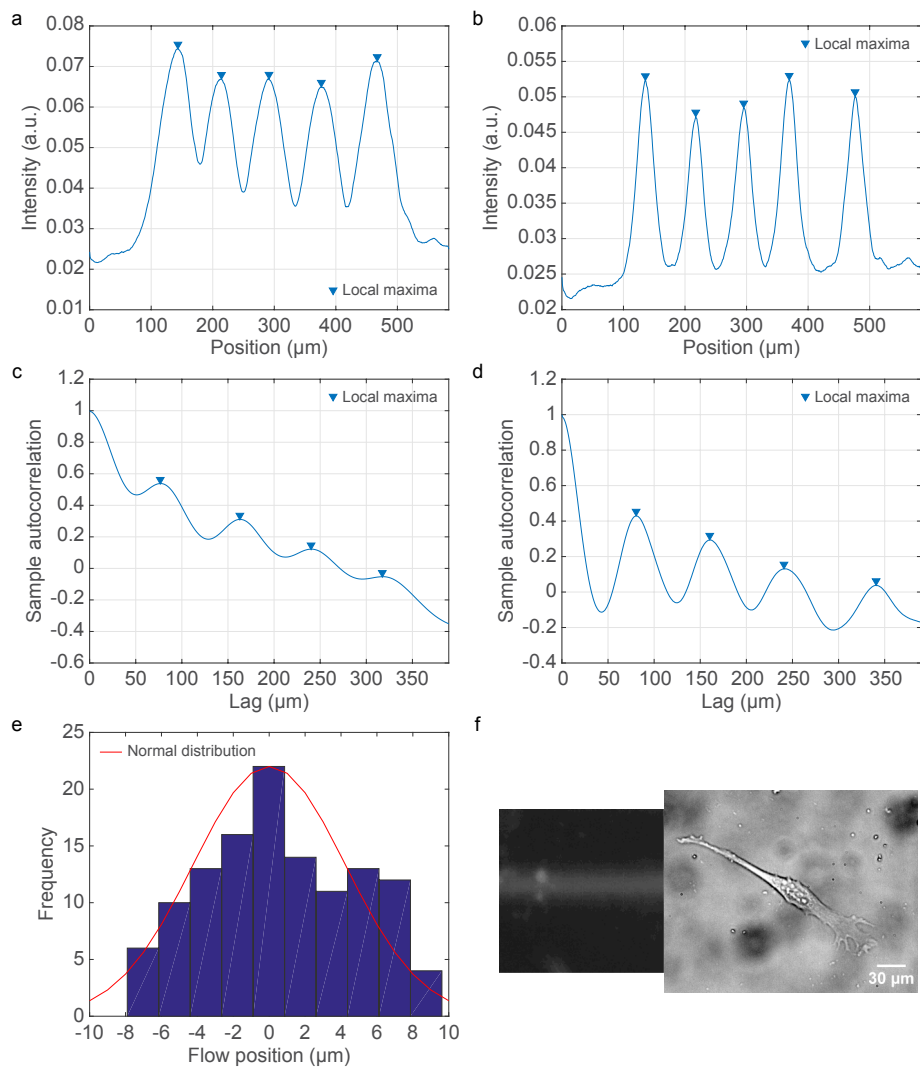
Figure 4.8: Flow accuracy and resolution characterization. Smoothed intensity data from the regions indicated in Fig. 4.7d of experiment set 1 (a) & 2 (b). Autocorrelation of the data from experiment set 1 (c) & 2 (d). (e) A position distribution histogram of the center flow over a 2-hour period. Data also plotted temporally in Fig. 4.7f. Red line shows a normal distribution (normalized to the maximum frequency) with the same standard deviation as the position distribution. (f) Expanded view of the region of interest indicated in Fig. 4.7c. Contrast adjusted to aid flow visualization. The flow is compared to a typical fibroblast cell. The images have the same scale.

Figure 4.9: TTX partially perfused to CaMPARI flies. (a) A CaMPARI embryo under TTX perfusion at the red region (top), and PBS perfusion elsewhere (bottom). Red background, made pronounced by adjusting image contrast, in top perfusion due to autofluorescence from food dye added to help visualize the flow. The regions enclosed by the green and blue boxes are shown in Fig. 4.10. (b) Their intensity values are summed and plotted. An increase in red fluorescence is observed as soon as the perfusion commences only in cells that are under TTX perfusion, suggesting that blockage of Na_v channels can lead to calcium influx in neurons. The initial offset is due to the setup phase.
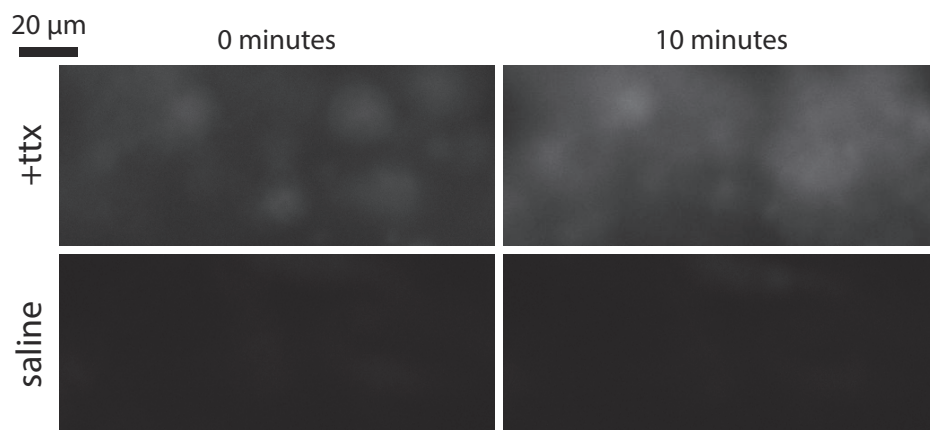
Figure 4.10: Regions of interest from Fig. 4.9a expanded. Red fluorescence observed only in cells under ttx perfusion.
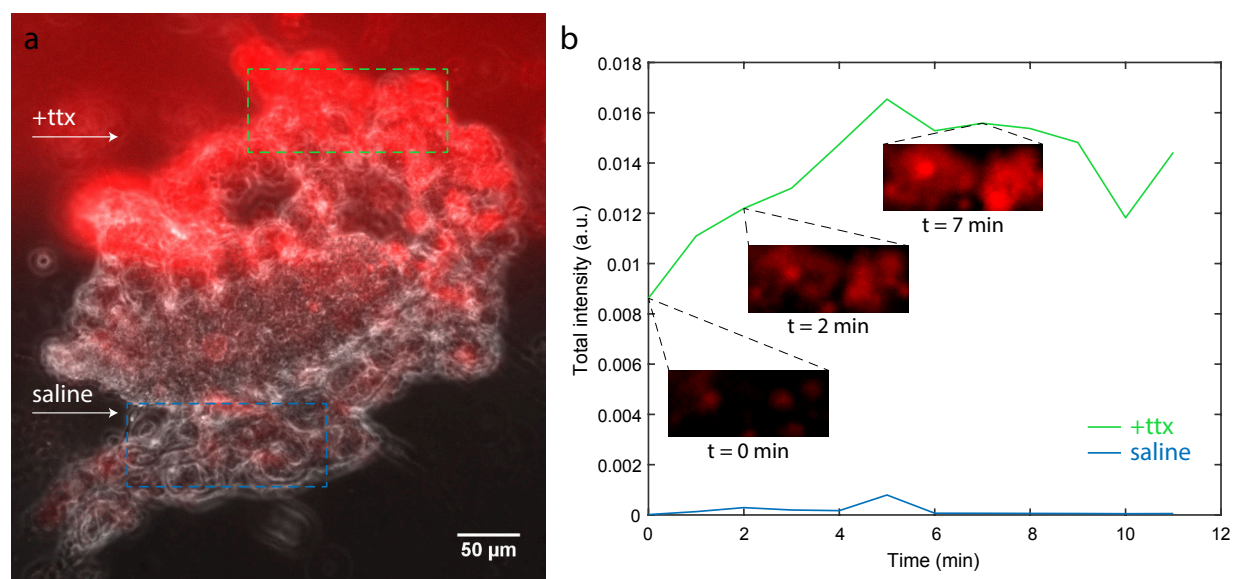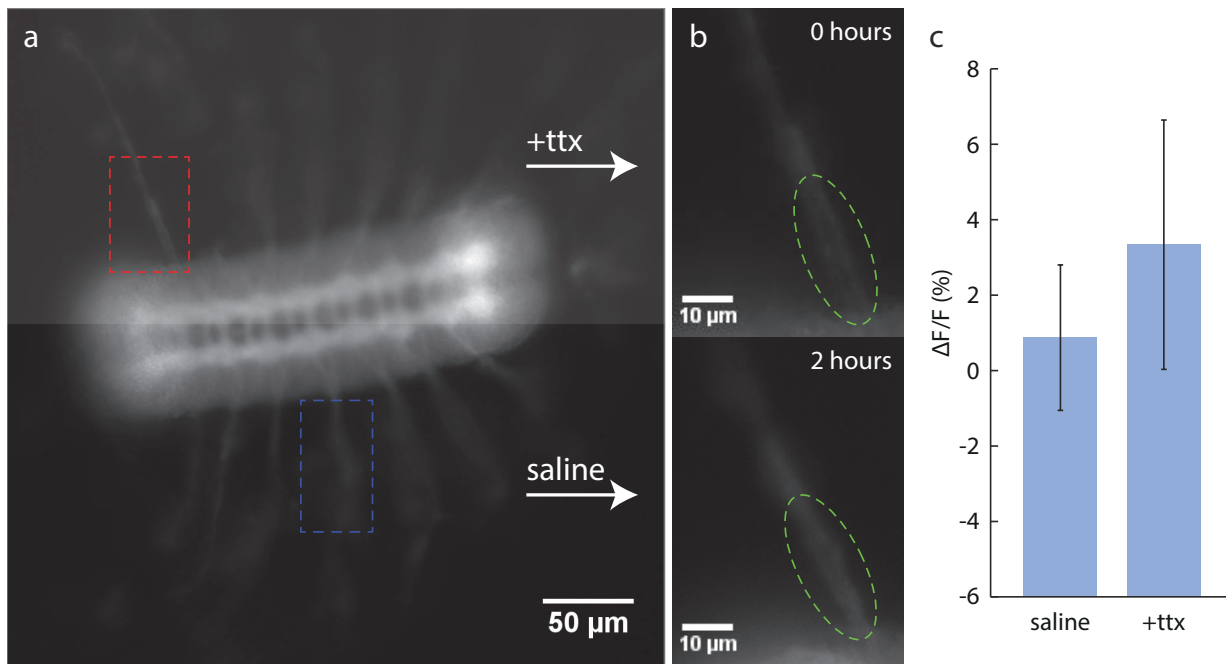
Figure 4.11: TTX partially perfused to ArcLight flies. (a) An ArcLight embryo under TTX perfusion at the lighter region (top), and PBS perfusion elsewhere (bottom). The top shade is added digitally (based on bright field images) to help visualize the flow. The regions enclosed in red and blue are depicted in (b) & Fig. 4.12 respectively. (b & c) An increase in fluorescence is observed after 2 hours of perfusion only in axons (b) that are under TTX perfusion (saline: N=5, ttx: N=4), suggesting that blockage of Na_v channels can lead to axon hyperpolarization. Note that no digital shades are added to Fig. 4.11b.

Figure 4.12: Regions of interest from Fig. 4.11a expanded. Small fluorescence increase in the axon under ttx perfusion.
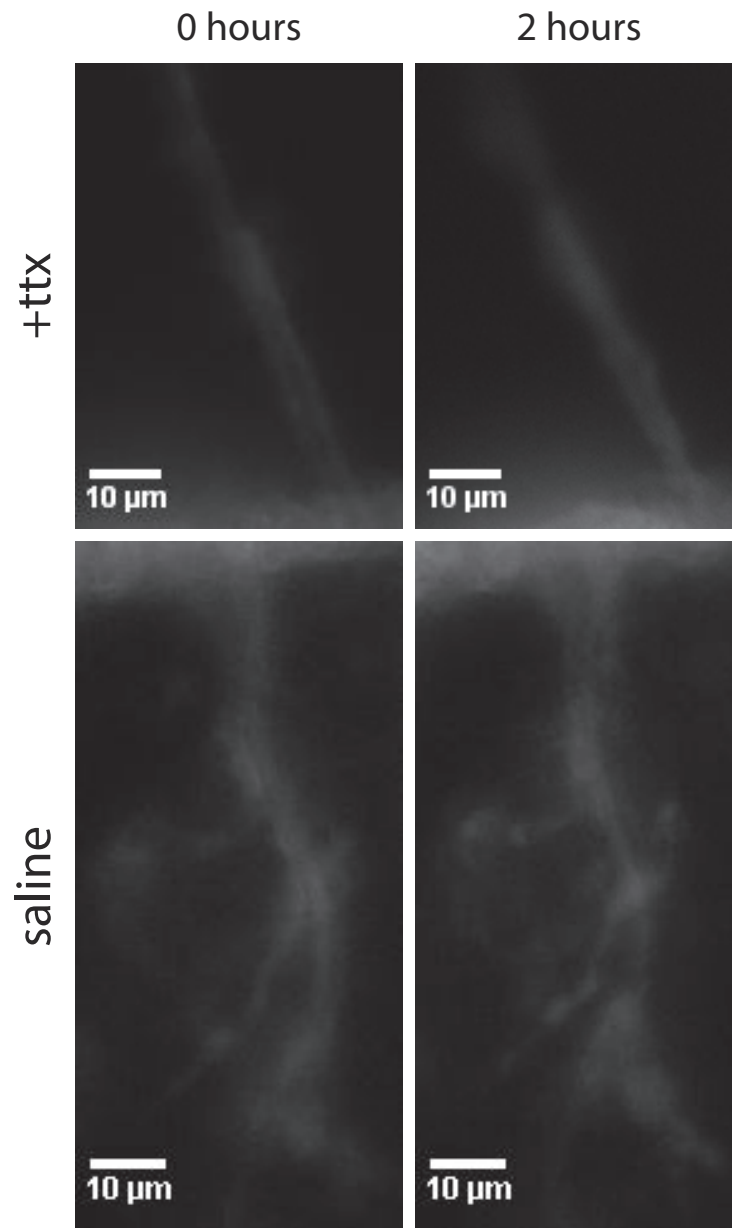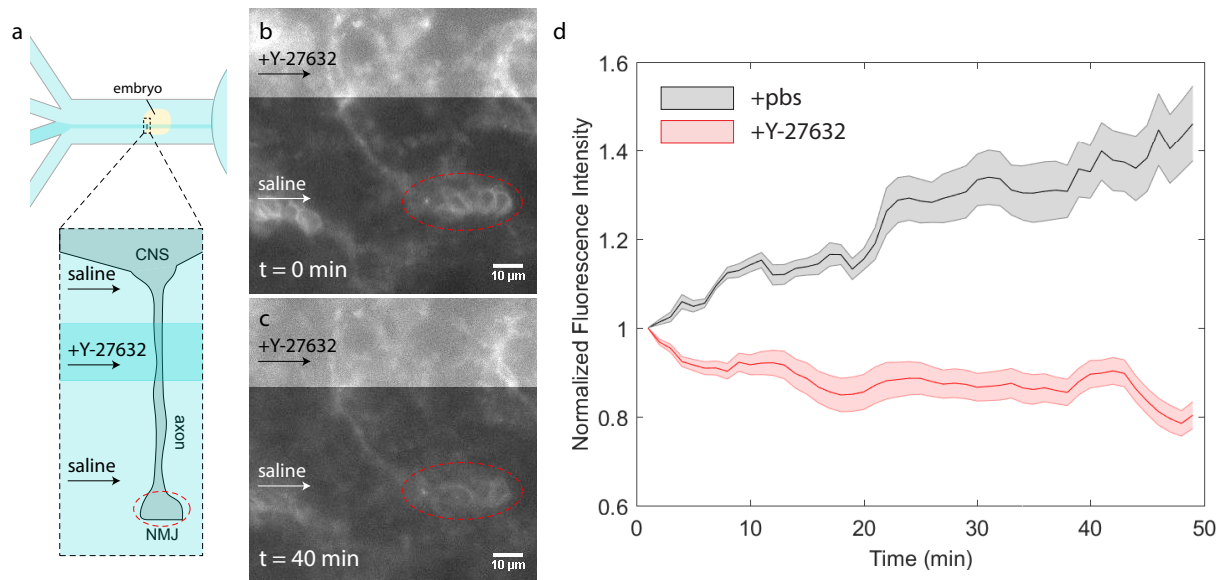
Figure 4.13: Y-27632, a myosin inhibiting drug, partially perfused to a segment of axons away from the presynaptic terminal of stage 16 Drosophila embryos. (a) An illustration of the experiment. (b & c) Images of a presynaptic terminal at different time points. Red ovals indicate the presynaptic terminal. White shades added digitally to indicate the region of Y-27632 flow. (d) Fluorescence intensity at the presynaptic terminal (N=3) decreases with time under indirect Y-27632 perfusion, suggesting that myosin has a far-field effect on maintaining vesicle clustering, while the unperturbed synapses (N=3) increase vesicle clustering as part of the development process.

Demonstration 3: Partial myosin inhibition along an axon stops vesicle accumulation at presynaptic terminal

In order to achieve sub-cellular perfusion, we used 3 simultaneous flows in a 4-channel device to perfuse exposed axons that had green fluorescence protein fused to synaptotagmin, a vesicle protein. The 2 side flows consisted of regular saline, while the center flow had Y-27632 added (Fig. 4.13a). Y-27632 inhibits myosin activity and reduces contractile force in cells [22]. The center flow was focused onto the proximal region of the axons of interest, leaving the distal synaptic regions unperturbed (Fig. 4.13a). This reduced the acto-myosin-dependent mechanical tension [55, 97], shown to be important in sustaining vesicle clustering [2], generated by the axons. We observed vesicle declustering at the distal presynaptic terminal (Fig. 4.13b–d) under partial tension loss (by proximal Y-27632 perfusion in our case), similar to another study [2] that disrupted tension by excising the axon instead—an operation that, however, could lead to other complications.

4.4 Conclusions

We developed a microfluidic device to selectively expose part of small organisms to drugs. A unique feature of the device, in contrast to other microfluidic systems, is the sequence of sample preparation and device fabrication. Here, samples were prepared first, followed by device assembly. This was possible due to LSR, in contrast to PDMS, as the material of choice for the device. LSR is 3 times more compliant than PDMS, and is more adhesive to glass without any treatment. Placement of the device on the prepared samples offered the ability to 1) study samples that are insuspendable, and 2) control channels orientation with respect to the samples. The device was characterized and tested for its performance under flow rate and duration that were an order of magnitude above what it was designed for. Accounting for the flow width and flow stability overtime, we validated that the device can achieve partial treatment accurately in a region of 30 μm in a 1 mm chamber—a resolution of 3 %. We used mutant *drosophila* to test the feasibility of the device in studying neurological phenomena. We observed increased calcium activities and weak membrane hyperpolarization under selective Na_v inhibition, similar to what was previously reported [99, 102, 103]. We further showed that selective tension inhibition in the proximal segment of an axon can lead to loss of vesicles in its distal presynaptic terminal, further supporting the far-field effect of tension on vesicle clustering previously observed [2]. These demonstrations showcase the new experimental possibilities on samples that were previously difficult to test because of the constraints of pre-assembled fluidic devices.

Chapter 5

A method to characterize adhesion energy at the interface of a soft sample and a stiff substrate

This chapter is adapted from a manuscript in preparation[1].

5.1 Motivation

Permanent or temporary bonds form at interfaces between dissimilar materials. Depending on the strength of the bonds, the interface could be stable against varying degrees of mechanical perturbations resulting in adhesion. Since adhesion can be thought of as the minimization of interfacial surface exposed to the ambient fluid—when the formation of interfacial bonds are more energetically favorable, it is therefore usually described as an energy per unit area quantity. Essentially, it quantifies the amount of energy required to separate the interface by a unit area.

To design and fabricate composite structures that rely on adhesion, methods that allow the quantification of adhesion energy have been developed [104]. Most methods work by first forming the adhesive interface, then subsequently measured the energy required to separate the interface into 2 surfaces. One example is induced delamination by peeling [105, 106] or with an axial stretcher as in the case of mode I fracture [107].

The adhesion properties of thin films are also studied extensively [108]. Some recent thin film characterization extends into the nano-scale regime where 2D materials, such as graphene [109, 110], are studied. Because of the size of the sample, it is no longer suitable to study adhesion by separating interface. Thus a bead intercalation method was developed [111], in which a bead is trapped between the 2D material and a substrate. The trapped bead would introduce a blister at the sample-substrate interface and the radius of the blister allows the determination of adhesion energy [111].

Beyond thin films however, the bead intercalation method is rarely used, mainly due to the lack of an

---

[1]Fan A, Delatorre M, Li Z, Salam M, Saif MT. Bead intercalation to measure adhesion energy of the interface between a deformable sample and a stiff substrate—Theory and Experiments. In preparation

appropriate mechanics model. The adhesion of thicker soft polymer is therefore studied using other methods, such as by inducing a pressure difference to cause sample-substrate delamination, known as the blister test [112, 96]. We believe the generalization of the bead intercalation method to thicker samples would provide a simpler alternative in studying interfacial adhesion of soft material, important in, for example, the fabrication of composite materials [113] and microfluidic devices [114].

Therefore, we propose a simple method that allows for the quantification of adhesion energy between a deformable sample with finite thickness and a stiff substrate by intercalating a spherical bead at the interface. We developed 2 sets of analytical theory, based on plate bending and contact mechanics theory respectively, to describe the interaction. Finite element simulations were conducted to support the analytical models. Experiments using PDMS and LSR over a glass substrate were performed to verify the results. A piece of software, as an ImageJ or MATLAB plug-in, was developed to aid analysis and adhesion energy computation.

5.2   Materials & Methods

Finite Element Simulation

An axisymmetric finite element model was established using ABAQUS to obtain the total strain energy and deformation profiles of the elastomeric samples. Four-node bilinear axisymmetric quadrilateral (CAX4) elements were used to discretize the geometry of the elastomer, and refined meshes were adopted to ensure the accuracy. Linear elastic model was used to characterize the material behavior. The Young's modulus and Poisson's ratio used were $E = 1.72$ or 0.403 MPa and $\nu = 0.49$ for PDMS and LSR respectively. The bead was considered to be rigid because it was much stiffer than the elastomer, and thus, its deformation was negligible. "Hard contact" was implemented to simulate the interface between the bead and the elastomer, with allowed sliding in the tangential direction. The distance between the bead and elastomer edge was kept constant of 0.5 mm in all simulation cases. Finally, displacement boundary conditions were assigned to the rigid bead to apply different levels of compression.

Sample Preparation

A glass cover slide was cleaned with compressed air in order to remove debris. Afterwards, a glass bead with a diameter of 75 μm or 250 μm was positioned at the center of the cover slide. A stereo microscope was used to visually check the quality of the glass bead. A soft polymer disk mold by the lid ($d = 3.878$ cm) or dish (d

68

= 3.5 cm) of 35 mm petri dishes was then gently laid on top of the glass bead and allowed to adhere to the cover slide. A blister would form around the bead during this process. Samples were then brought inside a vacuum chamber for 15 minutes to vent the air inside the blister. The soft polymer used was one of 3 types: PDMS mixed in a 10:1 base/agent ratio, PDMS mixed in a 25:1 base/agent ratio, and LSR mixed in a 1:1 base/agent ratio. The prepared samples were imaged immediately after leaving the vacuum chamber.

Imaging

Each blister was imaged under an inverted microscope with a 4x lens to identify the region of delamination. A motorized stage was used whenever the 4x lens did not have enough field of view for the blister, so that a larger image of the entire blister could be reconstructed by stitching individual smaller images of a portion of the blister. The beads were imaged using a 10x lens to examine their size distribution.

Analysis

We performed edge detection of the blister by first asking input from human users for an estimate of the center point and a point on the edge of the blister. The canny edge detection method was then deployed to identify edges. The human selected points were used to construct a circle, which serves to exclude identified edges that were beyond $\pm20\%$ of the radius of the constructed circle. A circle was then fitted using the least squares method to the remaining points of edges, providing the blister's delamination radius.

Software

A MATLAB graphic user interface (GUI) and an ImageJ plugin were developed to perform the image analysis, estimate the delamination radius, and compute the adhesion energy.

5.3   Results

Analytical models developed to measure adhesion energy from blister radius

Kirchhoff plates

We have the following scenario: a glass bead is sandwiched between a glass substrate and a silicone disk (Fig. 5.1a). For all practical purposes, the bead and the glass substrate can be assumed to be rigid. The bead can be seen as inducing a crack in the silicone-glass interface by deforming the silicone disk. We aim
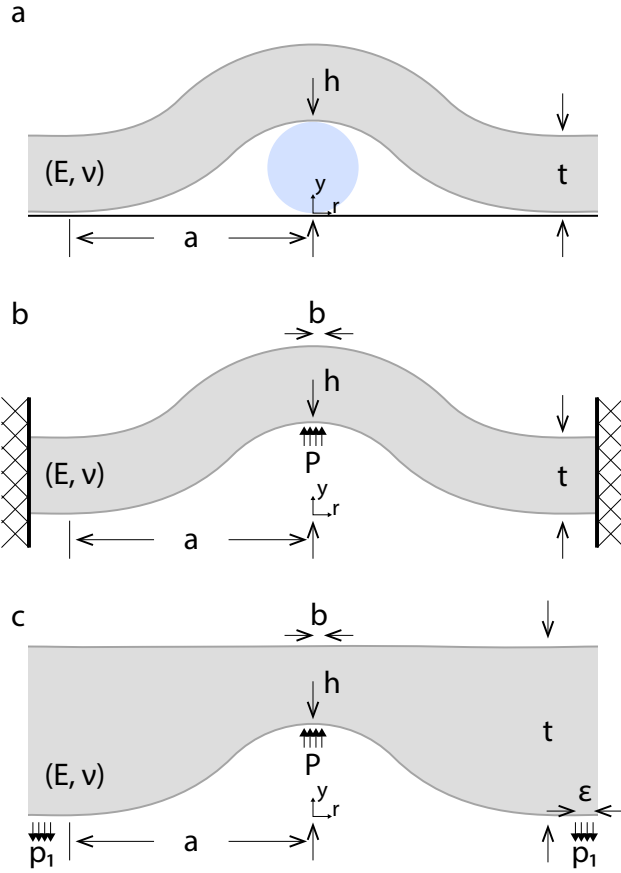
Figure 5.1: Graphical illustration of (a) the experimental setup, and the mechanical models based on (b) plate theories and (c) contact mechanics.

to compute the interface energy given the height of the bead (h) and the radius of the crack (a).

We assumed the model in Fig. 5.1b, where there is a point load P at the center of the disk. The displacement profile (u) in the radial direction (r) of the above loading scenario is given by [115]:

$$u(r) = \frac{P}{16\pi D} \left[a^2 - r^2 \left(1 + 2\ln\left(\frac{a}{r}\right) \right) \right] \tag{5.1}$$

where $D = \frac{Et^3}{12(1-\nu^2)}$

At $r = 0$

$$u(r = 0) = u_0 = \frac{3Pa^2}{4\pi E't^3} \tag{5.2}$$

where $E' = \frac{E}{1-\nu^2}$

Therefore,

$$P(u_0) = \frac{4\pi E't^3}{3a^2} u_0 \tag{5.3}$$

The strain energy of the system (U_m) can be found by integrating the force over the vertical displacement [116], i.e.

$$U_m = \int P(u_0) du_0 \tag{5.4}$$

$$= \int_0^h \frac{4\pi E't^3}{3a^2} u_0 du_0 \tag{5.5}$$

$$= \frac{2\pi E't^3 h^2}{3a^2} \tag{5.6}$$

Now $a \to \infty$ if there is no adhesion, because that would relax the strain energy stored. Adhesion energy (U_s) takes the form $U_s = \gamma\pi a^2$, where $\gamma = \gamma_{ga} + \gamma_{sa} - \gamma_{sg}$. γ_{ga}, γ_{sa}, and γ_{sg} are the amount of energy required to make a unit area surface for glass-air, silicone-air, and silicone-glass interfaces respectively. $a \to 0$ if there is only adhesion and no strain energy. Therefore, finding the minimum of the total energy $U = U_m + U_s$ will give a corresponding critical a, and as a result γ. Specifically,

$$\frac{dU}{da} = \frac{dU_m}{da} + \frac{dU_s}{da} = 0 \tag{5.7}$$

$$-\frac{4\pi E't^3 h^2}{3a^3} + 2\gamma\pi a = 0 \tag{5.8}$$

$$\gamma = \frac{2E't^3 h^2}{3a^4} \tag{5.9}$$

This method of measuring adhesion energy could be very sensitive as it scales with a^{-4}.

Mindlin plates

Since Kirchhoff plates theory are only appropriate to thin plates, we consider as well another set of plate theory known as Mindlin plates.

In axisymmetric problem, we can compute Mindlin deflection (u_M) from known deflection (u_K) of Kirchhoff plates [117]:

$$u_M = u_K + \frac{M_K - \tilde{M}_K}{K_s G t} \tag{5.10}$$

where M_K is the Marcus moment, and $\tilde{M}_K$ is the Marcus moment at the clamped edge, defined as [117]:

$$M_K = -D\frac{1}{r}\frac{d}{dr}\left(r\frac{du_K}{dr}\right) \tag{5.11}$$

$$\tilde{M}_K = -D\frac{d^2 u_K}{dr^2}\bigg|_{r=a} \tag{5.12}$$

To avoid running into the $\ln(\frac{1}{r})$ singularity in Eq. 5.1, we replaced the point load with a concentrated uniform pressure, p at $0 \leq r \leq b$. The Kirchhoff deflection profile is given as follows:

For $0 \leq r \leq b$,

$$u_K = \frac{pa^4}{64D}\left[\left(\frac{r}{a}\right)^4 + \alpha^2\left(4 - 3\alpha^2 + 4\alpha^2\ln\alpha\right) - 2\alpha^2\left(\frac{r}{a}\right)^2\left(\alpha^2 - 4\ln\alpha\right)\right] \tag{5.13}$$

And for $b \leq r \leq a$,

$$u_K = \frac{p\alpha^2 a^4}{32D}\left\{2\left[\alpha^2 + 2\left(\frac{r}{a}\right)^2\right]\ln\left(\frac{r}{a}\right) + (2 + \alpha^2)\left[1 - \left(\frac{r}{a}\right)^2\right]\right\} \tag{5.14}$$

where $\alpha = \frac{b}{a}$. By substituting Eq. 5.13 & 5.14 to Eq. 5.11 & 5.12, and then subsequently to Eq. 5.10, one can compute the Mindlin deflection.

Because for any given r, both u_K and u_M is linear to p; complementary strain energy is equal to strain

energy. Therefore,

$$dU_m = p \, dA \, du = u_{(K,M)}(r,p) \, dp \, dA \tag{5.15}$$

$$U_m = \int_0^{2\pi} \int_0^b \int_0^{p(h)} u_{(K,M)}(r,p) \, dp \, r \, dr \, d\theta \tag{5.16}$$

We set $u_{(K,M)}(r=0) = h$ to find the corresponding $p(h)$.

This has set us up to use Eq. 5.7 again to obtain γ.

$$\gamma_K = \frac{8E't^3h^2 \left(2a^2 - b^2\right) \left[24a^4 - 2a^2b^2 - 21b^4 + 12\left(6a^2b^2 + b^4\right)\ln\left(\frac{b}{a}\right)\right]}{9a^4 \left[4a^2 - 3b^2 + 4b^2\ln\left(\frac{b}{a}\right)\right]^3} \tag{5.17}$$

$$\gamma_M = \frac{8GK_sh^2t^3E'\{GK_s\left[144a^6GK_s + 9b^4\left(7b^2GK_s - 4t^2E'\right) + a^4\left(-84b^2GK_s + 48t^2E'\right) - 4a^2\left(30b^4GK_s + b^2t^2E'\right)\right]}{a^4\left[12a^2GK_s - 9b^2GK_s + 4t^2E' + 4\left(3b^2GK_s - 2t^2E'\right)\ln\left(\frac{b}{a}\right)\right]^3}$$
$$\frac{+ 4\left[12a^4GK_s\left(9b^2GK_s - 2t^2E'\right) + 3b^4GK_s\left(-3b^2GK_s + 2t^2E'\right) - 4a^2\left(9b^4G^2K_s^2 - 9b^2GK_st^2E' + 2t^4E'^2\right)\right]\ln\left(\frac{b}{a}\right)\}}{} \tag{5.18}$$

where K_s is the shear correction coefficient, which is assumed to be $\frac{5}{6}$ throughout the text [117]. Note that $\lim_{b\to 0} \gamma_K = \frac{2E't^3h^2}{3a^4}$, which is what we obtained for γ previously with the point load assumption.

Half-space indentation

The Mindlin theory accounts only for plate bending. For thick samples ($t \gg a$), it is not applicable. Therefore, we also developed a model for thick samples by using the half-space assumption. From the solution of the Boussinesq problem, we know that the surface displacement of a half-space from a normal point load is:

$$u_3 = \frac{P}{\pi E'r} \tag{5.19}$$

To avoid dealing with the $\frac{1}{r}$ singularity, we use a concentrated uniform pressure instead of a point load. This is essentially achieved by convolving the point load solution over the area of a circular loading region
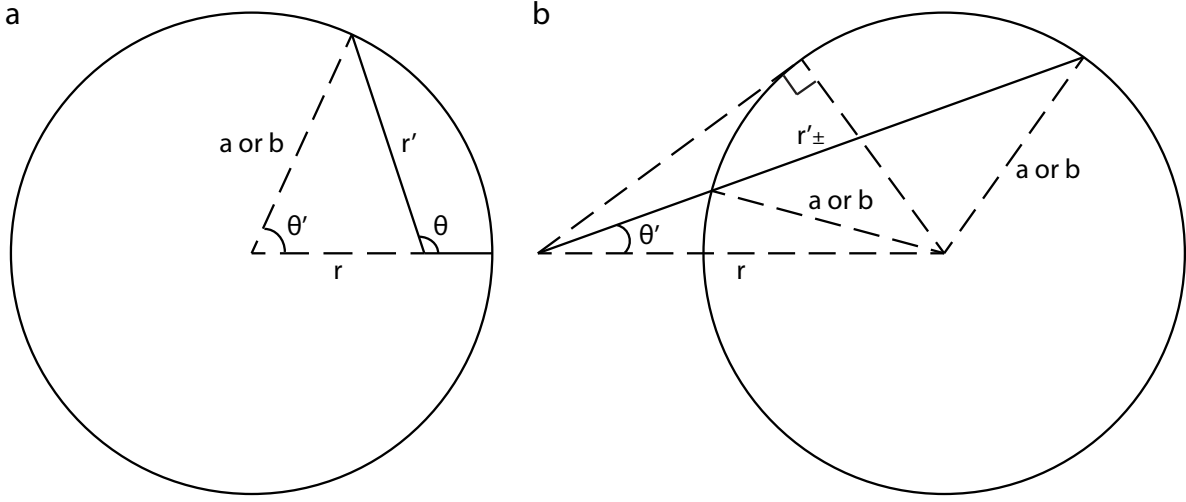
Figure 5.2: Graphical illustration of the relationship between r, r', θ, θ', and a or b.

of radius b. For a given r, where $0 \leq r \leq b$:

$$du_3 = \frac{pdA}{\pi E' r'} \tag{5.20}$$

$$u_3 = \int_0^{2\pi} \int_0^{r'(\theta)} \frac{p}{\pi E' \hat{r}'} \hat{r}' d\hat{r}' d\theta \tag{5.21}$$

$$= \frac{p}{\pi E'} \int_0^{2\pi} r'(\theta) d\theta \tag{5.22}$$

where $\hat{r}' = r'(\theta)$ is the expression of the perimeter of the circle when the origin is shifted by a distance r. Note that the case is axisymmetric, and therefore the angle (θ) of the shift is inconsequential. Eq. 5.22 is essentially summing the displacement contributions of all the load at the point (r, θ). The expression for $r'(\theta)$ can be obtained from trigonometry as illustrated in Fig. 5.2a:

$$\cos(\pi - \theta) = \frac{r^2 + r'^2 - b^2}{2\, r\, r'} \tag{5.23}$$

Solving Eq. 5.23 for r' and rejecting the negative solution yield:

$$r'_+(\theta) = \sqrt{b^2 - r^2 \sin^2 \theta} - r \cos \theta \tag{5.24}$$

which can be substituted back to Eq. 5.22. Finally, by evaluating Eq. 5.22,

$$u_{3+} = \frac{p}{\pi E'} \, 4b \, E_E \left(\frac{r^2}{b^2} \right), \qquad \text{for } 0 \leq r \leq b \tag{5.25}$$

74

where $E_E(m)$ is the complete elliptic integral of the second kind.

Now let us consider the region outside the loading zone. For $r > b$

$$
\begin{aligned}
u_3 &= 2 \int_0^{\sin^{-1}\left(\frac{b}{r}\right)} \int_{r'_-}^{r'_+} \frac{p}{\pi E' \hat{r}'} \hat{r}' d\hat{r}' d\theta^* \\
&= \frac{p}{\pi E'} 2 \int_0^{\sin^{-1}\left(\frac{b}{r}\right)} r'_+(\theta^*) - r'_-(\theta^*) d\theta^*
\end{aligned}
\tag{5.26}
$$

where (Fig. 5.2b)

$$
r'_\pm(\theta^*) = r \cos \theta^* \pm \sqrt{b^2 - r^2 \sin^2 \theta^*}
\tag{5.27}
$$

By following the procedure previously described, we obtain:

$$
u_{3+} = \begin{cases}
\dfrac{4bp}{\pi E'} E_E\left(\dfrac{r^2}{b^2}\right), & \text{if } 0 \le r \le b \\[3mm]
\dfrac{4bp}{\pi E'} E_E\left(\sin^{-1}\left(\dfrac{b}{r}\right), \dfrac{r^2}{b^2}\right), & \text{if } r > b
\end{cases}
\tag{5.28}
$$

where $E_E(\phi, m)$ is the incomplete elliptic integral of the second kind, or simply

$$
u_{3+} = \frac{4bp}{\pi E'} Re\left(E_E\left(\frac{r^2}{b^2}\right)\right)
\tag{5.29}
$$

u_{3+} is the solution to the surface displacement of a half-space subjected to a uniform pressure, p, at a region $r \le b$. But our problem also have the material clamped at $r \ge a$. One can solve the full set of mixed boundary conditions and obtain an exact solution, which could be quite challenging. Or one can approximate by superimposing solutions from other loading conditions. A ringed line load could be employed, but would result in an infinite displacement as $r \to a$. Instead, we prescribe a finite thickness, ε, to the ring. And the solution to this loading condition can be conveniently obtained by superimposing solutions of 2 uniform

pressures at opposite directions with radii a and $a + \varepsilon$ respectively. Specifically,

$$u_{3-} = - \begin{cases} \frac{4p_1}{\pi E'} \left((a + \varepsilon) E_E \left(\frac{r^2}{(a + \varepsilon)^2} \right) - a E_E \left(\frac{r^2}{a^2} \right) \right), & \text{if } 0 \leq r \leq a \\[12pt] \frac{4p_1}{\pi E'} \left((a + \varepsilon) E_E \left(\frac{r^2}{(a + \varepsilon)^2} \right) - a E_E \left(\sin^{-1} \left(\frac{a}{r} \right), \frac{r^2}{a^2} \right) \right), & \text{if } a < r \leq a + \varepsilon \\[12pt] \frac{4p_1}{\pi E'} \left((a + \varepsilon) E_E \left(\sin^{-1} \left(\frac{a + \varepsilon}{r} \right), \frac{r^2}{(a + \varepsilon)^2} \right) - a E_E \left(\sin^{-1} \left(\frac{a}{r} \right), \frac{r^2}{a^2} \right) \right), & \text{if } r > a + \varepsilon \end{cases}$$

$$(5.30)$$

It can also simply be written as:

$$u_{3-} = -\frac{4p_1}{\pi E'} \left((a + \varepsilon) \, Re \left(E_E \left(\frac{r^2}{(a + \varepsilon)^2} \right) \right) + a \, Re \left(E_E \left(\frac{r^2}{a^2} \right) \right) \right) \tag{5.31}$$

Superimposing the solutions yields:

$$u_3 = u_{3+} + u_{3-} \tag{5.32}$$

We are interested in $u_3(r = 0)$ & $u_3(r = a)$.

$$u_3(r = 0) = h = \frac{2bp}{E'} - \frac{2\varepsilon p_1}{E'} \tag{5.33}$$

$$u_3(r = a) = 0 = pb \, E_E \left(\sin^{-1} \left(\frac{b}{a} \right), \frac{a^2}{b^2} \right) - p_1 \left((a + \varepsilon) E_E \left(\frac{a^2}{(a + \varepsilon)^2} \right) - a \right) \tag{5.34}$$

Force balance requires:

$$-p_1(2a\varepsilon + \varepsilon^2) + pb^2 = 0 \tag{5.35}$$

Thus, p, p_1, and ε can be obtained by solving the above 3 equations together.

The loading profile at the center however is not necessarily a uniform distribution. It is therefore useful to compare results with another loading profile. We conveniently use the Hertzian loading profile noting that it is most appropriate for a small contact area:

$$p(r) = p_0 \left(1 - \frac{r^2}{b^2} \right)^{\frac{1}{2}} \tag{5.36}$$

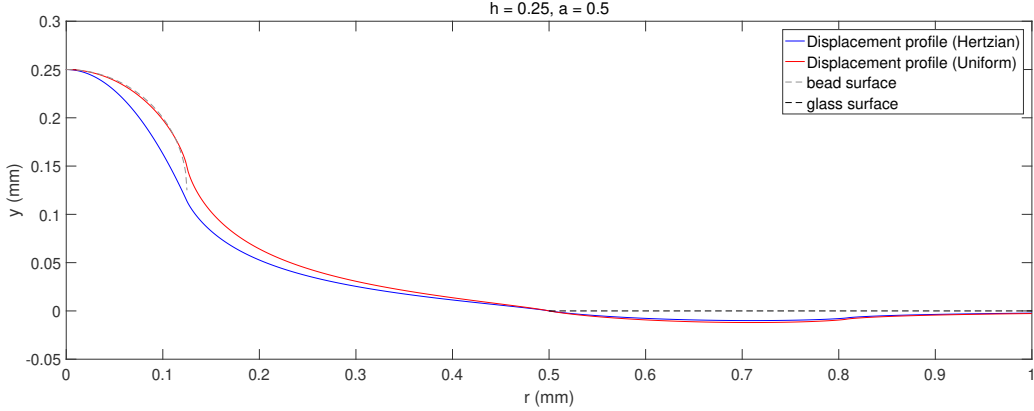The resulting displacement profile from the 2 loading conditions are plotted together in Fig. 5.3 for

Figure 5.3: Blue line shows the displacement profile resulting from a Hertzian load applied at $0 \leq r \leq h/2$. Red line shows the displacement profile resulting from a uniform load applied at $0 \leq r \leq h/2$. Grey dashed line shows the bead's top surface at $0 \leq r \leq h/2$, and black dashed line shows the glass surface at $r > a$.

comparison purposes. The uniform load resulted in a displacement profile matching the bead surface, while the Hertzian condition did not, justifying the selection of the uniform load profile. Compatibility is not satisfied at $r > a$ as expected; a negative displacement was observed. The difference, however, is small and does not contribute significantly to strain energy calculations, as shown previously by others [118].

Finally, we use the same method as previously described to get γ for the uniform loading condition:

$$\gamma = -\frac{1}{2\pi a} \frac{d \left[\int_0^{2\pi} \int_0^b \int_0^{p(h)} u_3(r,p) \, dp \, r \, dr \, d\theta \right]}{da} \tag{5.37}$$

Finite element simulation results validated analytical models

To verify the analytical model, finite element analyses (FEA) were performed on samples with different thicknesses. We applied a fixed boundary condition ($u = 0$) at $r \geq 0.5$ mm. A rigid sphere with $d = 0.25$ was brought to indent the disk at $r = 0$. Strain energy was computed for various disk thicknesses when the indentation has reached the full diameter of the bead ($u(r = 0) = 0.25$ μm). A deformation mode change from bending to indentation was observed when sample thickness increased (Fig. 5.4a).

The strain energy values computed by FEA simulations as the indentation depth increased were obtained
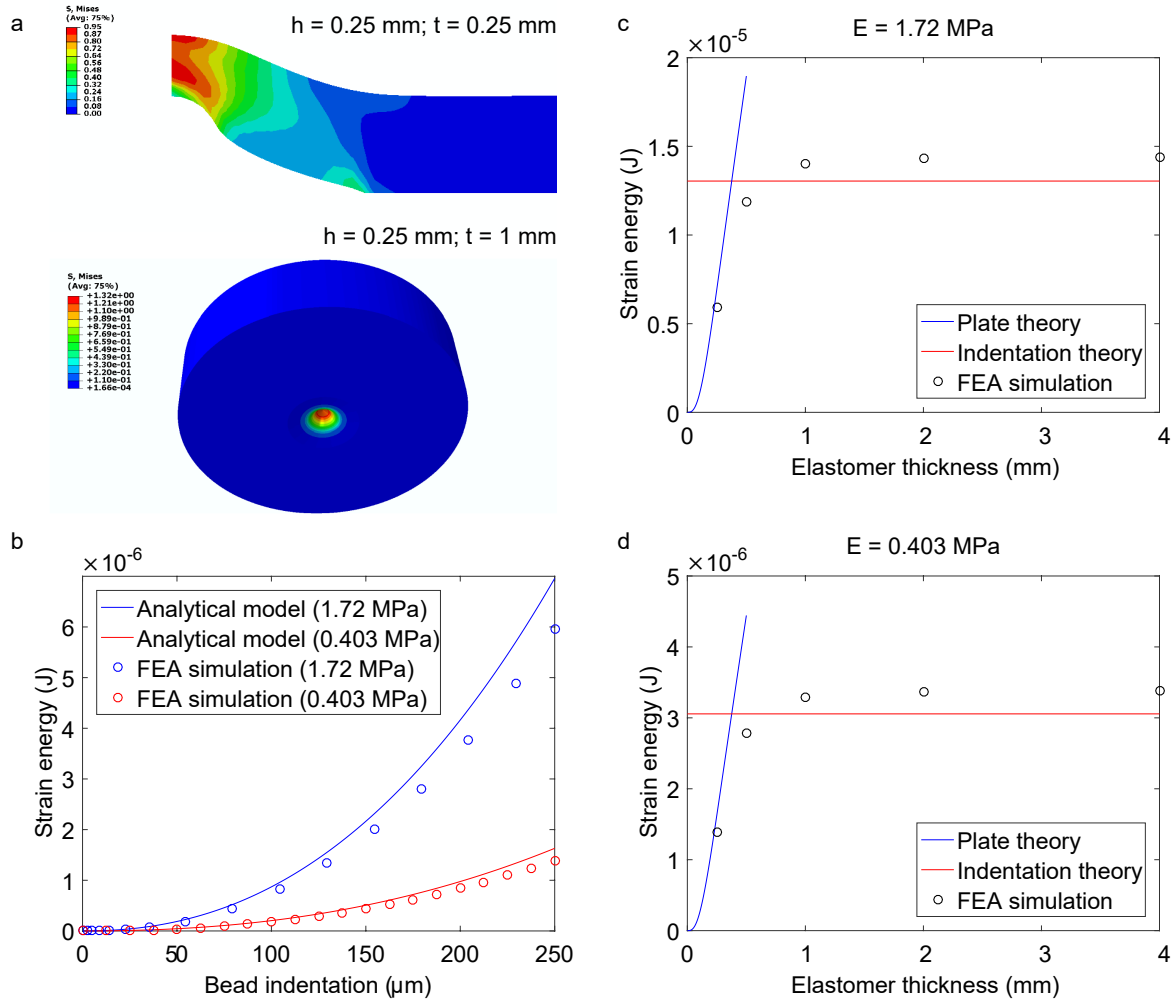
Figure 5.4: FEA simulations compared with analytical models. (a) Cross-sectional view of a thin sample (t = 0.25 mm) and 3D view of a thick sample (t = 1 mm), both loaded by a 250 μm bead in FEA simulations. Mises stress in MPa. (b) Strain energy as a function of bead indentation depth for samples with t = 0.25 mm and E = 1.72 (blue) or 0.403 (red) MPa computed by FEA (hollow circle) and the Mindlin plate model (solid line). (c & d) Strain energy as a function of sample thickness computed by FEA simulations (hollow circle), the Mindlin Plate model (blue line), and the half-space indentation model (red line) for samples with E = 1.72 or 0.403 MPa.

for the case of a thin sample ($t = 0.25$ mm). The results were displayed together with the strain energy values predicted by the Mindlin plate theory (Fig. 5.4b). We observed a close agreement between the 2 sets of data for both stiffnesses, verifying the accuracy of the analytical models.

When compared to the results of the analytical model, the strain energy values obtained from FEA simulations were well-predicted by the Mindlin plate theory at small thicknesses (Fig. 5.4c & d). As the thickness of the disk increased, the strain energy approached a plateau with values matching up with the thickness-independent indentation theory (Fig. 5.4c & d). This transition allows the deformation mode change from plate bending to indentation as the latter is becoming more energetically favorable when the sample thickness increases.

Experimental results of adhesion energy

Weight can serve as a reliable measurement of disk thickness

Disk thickness is an important parameter in our model. However, measuring the thickness of every disk could lead to debris build-up during the extra handling, inadvertently affecting the adhesion strength. Therefore, we wanted to measure the weight of the disks instead and subsequently extract the thickness from the weight measurements.

We measured the weight of the disks after polymerization, which allowed us to calculate a theoretical thickness based on the documented density for each material (PDMS: $\rho = 0.965$ g/cm^3; LSR: $\rho = 1.07$ g/cm^3). To measured their actual thickness for comparison, we placed fluorescence beads on the top and bottom surfaces of each disk and subsequently performed z-stack imaging to identify the best focal plane for both surfaces using the maximum gradient method (Fig. 5.5a). This allowed us to calculate the distance between the 2 surfaces, indicative of the actual thickness of the disks.

We observed a linear relationship between the theoretical and measured thickness (Fig. 5.5b). The slopes smaller than 1 could be attributed to the geometry of the lids and dishes, which have slanted inner walls. Based on the excellent correlation, thickness of the disks could be obtained by substituting the weight/theoretical thickness into the best-fit equations.
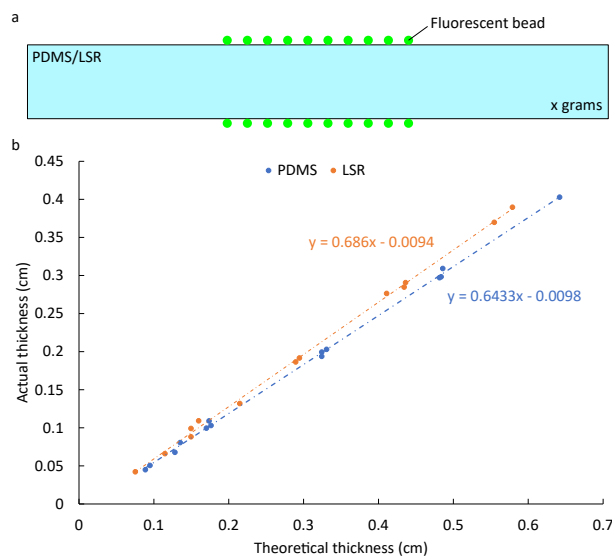
Figure 5.5: Thickness determination of samples. (a) Fluorescent beads (0.1 μm) are spread on the top and bottom surfaces of the sample. An optical z-stack of the sample is then obtained and the best focal plane of the 2 surfaces is determined by a computer algorithm. (b) Disks thickness measured vs. calculated based on weight ($h = \frac{4m}{\rho \pi d^2}$) of PDMS and LSR.

Adhesion energy computed from blister radius

A blister would form when intercalating the glass bead between the soft polymer disk and the stiff glass substrate (Fig. 5.6a & b). The blister (delamination) radius, as proposed in our model and others', is governed by the adhesion energy at the polymer-glass interface. Therefore, by measuring the blister radius (Fig. 5.6c), one can estimate the adhesion energy.

We checked the reliability of the method on 5 different preparations using combinations of 3 different materials (10:1 PDMS, 25:1 PDMS, and LSR) and 3 different bead sizes (75 μm, 250 μm, and 500 μm). The sizes of the beads were measured again using a light microscope with known pixel size (Fig. 5.7). We plotted the blister radii of the different experimental sets as a function of the disk thickness. Our energy analysis predicted that there should be a deformation mode transformation from bending to indentation as disk thickness increases. This transformation was most apparent with the 10:1 PDMS + 250 μm bead group (Fig. 5.8, blue), in which the blister radius initially increases, then drop to a smaller radius as indentation deformation becomes more favorable for thicker samples. The point of transformation was dependent on the height of the bead (indentation depth) (Fig. 5.8a) and the stiffness of the material (Fig. 5.8b), both expected to increase the energy to indent a sample, thus hindering a mode change.
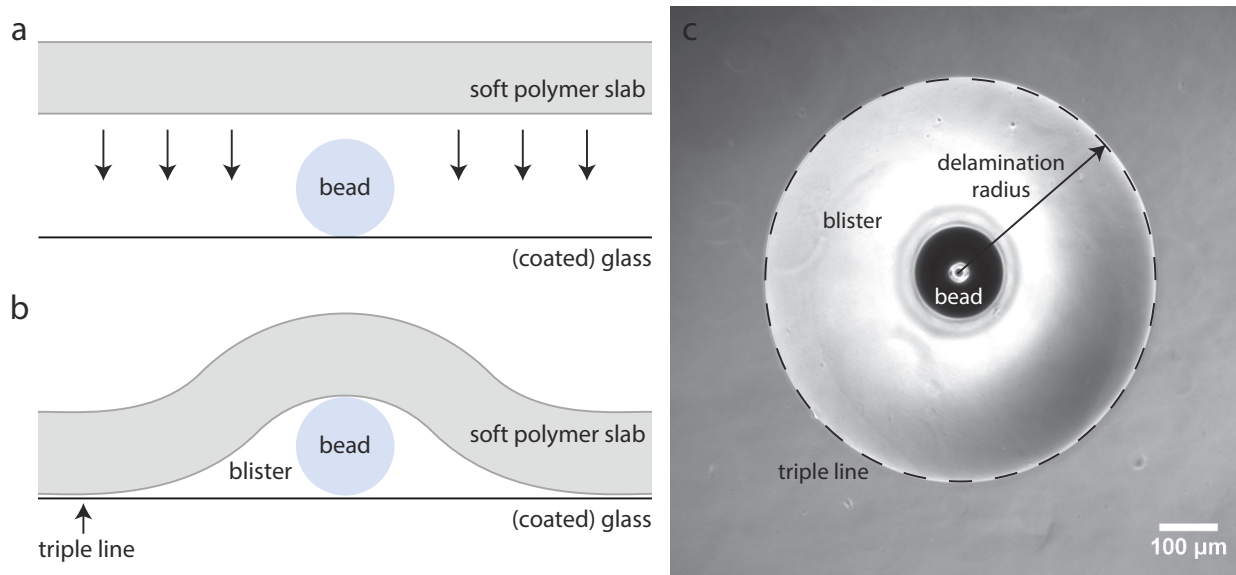
Figure 5.6: Experimental illustrations. (a) A soft polymer slab is brought to make contact with a glass substrate with a glass bead trapped between. (b) The trapped bead will allow the formation of a blister made visible by the polymer-glass-air triple line. (c) An image of the blister is taken. A piece of software will first compute the blister radius and then the adhesion energy based on the obtained radius and the mechanics models.
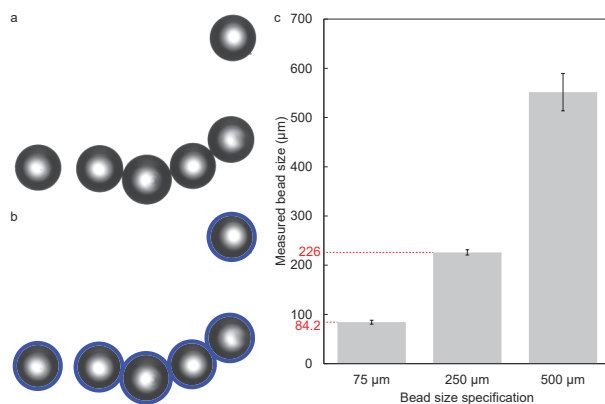
Figure 5.7: Analysis of bead sizes. (a) We obtained images of beads with diameter specifications of 75 (N=33), 250 (N=24), and 500 (N=26) μm. (b) The images are then analyzed to obtain the actual diameter of the beads using the built-in circular Hough transform ("imfindcircles") function in MATLAB. (c) The measured diameters are plotted against the manufacturer-specified diameter for all 3 groups.

Figure 5.8: Blister radius as a function of sample thickness for (a) 10:1 PDMS samples under the influence of 75 (black), 250 (blue) and 500 (green) μm beads, and (b) 10:1 PDMS (blue), 25:1 PDMS (magenta), and LSR (red) samples under the influence of 250 μm beads. Shaded regions show error in standard deviation.

Table 5.1: Comparison of adhesion energy of different samples

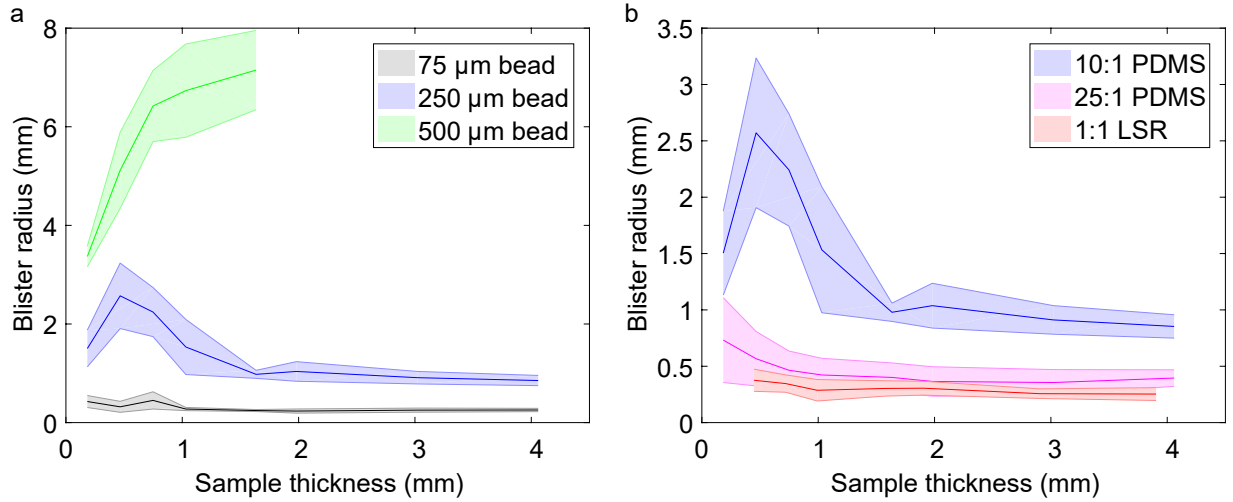| Sample	Young's Modulus (kPa)	Mean Bead Height (mm)	Thickness (mm)	Mean Blister Radius (mm)	Methodology	Adhesion Energy (J/m^2)
10:1 PDMS	1720	0.226	0.184	1.50	Mindlin	0.0725
10:1 PDMS	1720	0.226	4.06	0.853	Half-space	0.0856
10:1 PDMS	1720	0.0842	1.98	0.234	Half-space	0.0820
25:1 PDMS	313	0.226	3.02	0.356	Half-space	0.238
LSR	403	0.226	4.06	0.253	Half-space	0.898

In a separate table (Tb. 5.1), we showed the adhesion energy calculated by the Mindlin and half-space model for thin and thick samples respectively when the deformation mode was approaching pure bending or pure indentation. The values computed for PDMS were similar to that reported in literature [96]. We further used the half-space model to compute adhesion energy of other polymer-glass interfaces. Adhesion energy for samples intercalating 500 μm beads was not computed because of the large variation in their actual diameter.

Image analysis software

A piece of software was developed in ImageJ and MATLAB to aid analysis. An image of the blister is first treated with standard histogram equalization to enhance contrast (Fig. 5.9). In the ImageJ version (Fig. 5.10), users are asked to first import the blister image. The image will then be displayed and users are further asked to select the center of the blister and a point on the triple line. The software then employs

the canny edge filter to identify the triple line based on the estimation provided by the user. A best fit circle is then obtained from the identified triple line and the associated radius is recorded. Once the radius is recorded, another prompt will ask for the material properties of the sample. Based on these inputs, the software will compute and display values of adhesion energy using the 3 analytical models described here. The MATLAB version works similarly, but with the material properties prompt appearing earlier.

5.4 Discussion

Although the results from our analytical model seem to agree with those from FEA simulations and experiments, testifying to the validity of the assumptions made, we note that the assumptions are nonetheless unrealistic. We assumed a uniform pressure over a constant contact radius (b) at the bead-sample interface. The uniform pressure assumption seem to show good agreement with the ideal displacement boundary condition (Fig. 5.3), but at small displacement we know from Hertzain theory that the pressure profile should approach that given by Eq. 5.36. The constant contact radius is also not valid at small displacement. We suspect that these differences might not be significant, since in our case the entire bead is embedded inside the blister, and energy contribution is mostly resulting from the later phase of the indentation process. Furthermore, the fictitious negative displacement at region $r \geq a$ is a result of the ring load assumption (Fig. 5.3). In reality, we expect a decreasing load as r increases with the maximum occurring at the triple line. This load profile would lead to a larger strain energy. We expect, however, the difference to be small as demonstrated by others [118].

We initially hypothesized that the weight of the sample over the blister might influence the blister radius. This was shown to be untrue, since the blister radius did not vary significantly after the deformation mode change to indentation-dominant. Scaling arguments also show that the pressure exerted by the weight is negligible. The stresses obtained from FEA simulations are on the order of 1 MPa. The pressure from sample weight is quantified by $\rho g t$, and is on the order of 100 Pa for a 10 mm sample, 4 orders of magnitude smaller.

Internal blister pressure is another factor to consider. The actual pressure inside the blister is never measured. We assumed it to be equivalent to the ambient pressure in all our calculations. Any pressure difference can however influence the blister radius significantly. We mediate this by allowing the samples to form the seal as slowly as possible such that no extra air will be trapped. The samples used in this study are
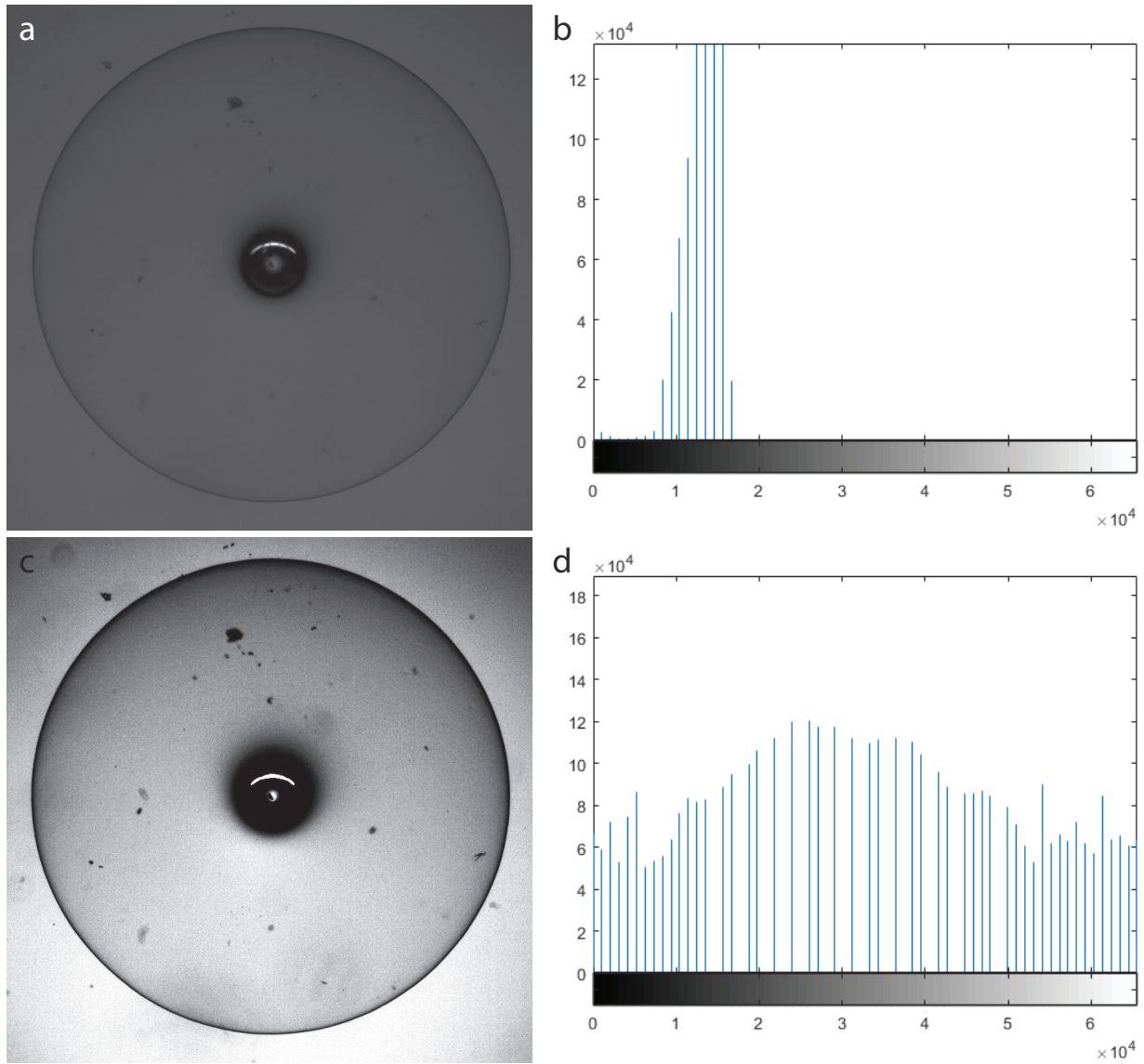
Figure 5.9: The contrast of the triple line can be increased by balancing the contrast of the blister image using the built-in histogram equalizaion ("histeq") function in MATLAB. An example is shown here with (a) the original image, (c) the adjusted image, and (b & d) their intensity distributions respectively.
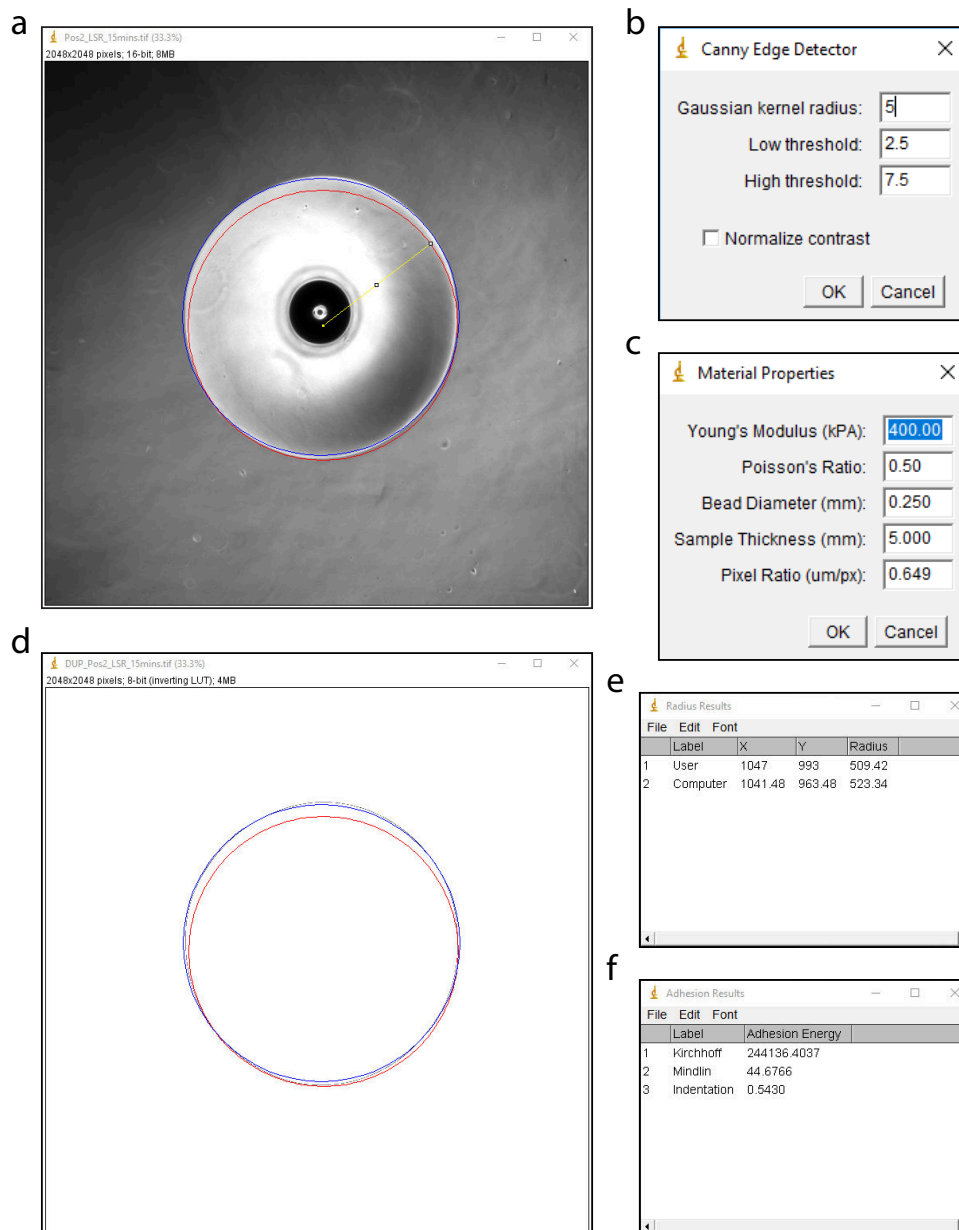
Figure 5.10: Screenshots of the ImageJ plugin. (a) A blister image is loaded into the ImageJ environment. The user is asked to draw a line connecting the center and the edge of the blister. (b) A prompt asking for input parameters in smoothing the image as part of the canny edge detector algorithm adopted from [cite]. (c) A prompt asking for the material properties of the sample and the experimental parameters. (d) An image of the identified edge (grey line), the best-fit circle to the edge (blue line), and the initial guess from the user (red line). (e) A pop-up window displaying the center coordinates and radius of the 2 circles. (f) A pop-up window displaying the values of adhesion energy computed based on the 3 analytical models described in the main text.

also gas permeable to a certain extent and thus pressure shall equate over time [119]. A better way to control the pressure could be by performing the measurements while the sample is under a constant vacuum, which could be done for example in a scanning electron microscope. However, in our study, we want to propose a simple method that can be accomplished by any light microscope without extensive sample preparations.

The visibility of the sample-substrate-fluid triple line is essential to the methodology proposed here. If the refractive indexes of the 3 materials are very similar, then contrast might be compromised. This loss in contrast can be rescued by introducing dyes, usually to the fluid [96]. Caution is required however to account for the influence of the presence of the dye to the adhesion strength of the interface. As such, a low dosage is desired.

In our current setup, since contrast is created by transmission light, both the sample and the substrate have to be transparent. This limitation can be negated by using reflection light to create contrast. In such case, only one of either the sample or the substrate has to be transparent. If both the sample and the substrate are opaque, light microscopy can no longer be used, and other imaging modalities should be explored.

Chapter 6

The mechanism of vesicle clustering by tension

This chapter is adapted from a submitted manuscript[1].

6.1 Motivation

Neurons communicate with each other and with other cells by releasing synaptic vesicles stored at the presynpatic terminal. Synaptic vesicles can be broadly categorized into 3 distinct pools [120, 121]: the readily releasable pool, the recycling pool, and the reserve pool. Among the three pools, vesicles at the reserve pool cluster together against dispersal and constitute the majority of all vesicles in most presynapic terminals [121]. Many binding proteins including synapsin [122, 123], α-synuclein [124], and endocytic scaffolding proteins [125] have been shown important in maintaining clustering. Furthermore, through functional [126, 127] and structural [128] studies, it has been shown that F-actin, together with these binding proteins [129], may form a scaffold [40, 130, 131] that allows vesicles to stay clustered.

F-actin assembly is facilitated by mechanical tension through stabilization of the catch bonds in F-actin and its associated binding proteins [132, 133, 39]. The axon being a cable like structure can provide the necessary tension to sustain the vast network of F-actin at the presynaptic terminal. Indeed, many experiments showed that axons maintain a rest tension [54, 12]. One experiment demonstrated that axon can generate its own intrinsic tension through actin and myosin contractility [55]. The recent discovery of periodic actin rings in axons [38] provides structural evidence that there exists a contractile network [97] along the axon that can generate tension.

There also exists functional evidence that tension can influence neural activity. It has been shown that tension and stretch can induce axon growth [4, 58], alter brain excitability [18], influence vesicle transport [17], and modulate neurotransmitter release [45]. One study [2] showed, by first excising the axon and

---

[1]Fan A, Tofangchi A, Saif MT. Presynaptic vesicle clustering is sustained by a tension-stabilized actin scaffold.

subsequently pulling the free end, that tension can influence vesicle clustering. However, the explanation of how axonal tension may mediate vesicle clustering remains elusive.

To develop a better understanding of the relationship between tension and vesicle clustering, we disrupted axonal tension by applying myosin disrupting drugs either globally or partially with laminar flows in embryonic drosophila, and subsequently monitored F-actin disassembly and vesicle declustering. We found, both F-actin and vesicle density decreases at the synapse under tension disruption. Tension was then restored by washing out the drug, which allowed F-actin and vesicles to recover. In both disruption and recovery, F-actin events occurred first. Fluorescence recovery after photobleaching (FRAP) experiments were conducted to reveal that declustered vesicles moved back into the axon conduit. Our results demonstrated that mechanical tension is necessary to sustain the F-actin network at the presynaptic terminal, which in turn provides anchorage for vesicles/their associated proteins to stay clustered.

6.2   Materials & Methods

Drosophila Melanogaster Culture

Drosophila culture follows standard procedure. The fly lines (6923, 8760, 58714) were purchased from Bloomington stock center. Flies were crossed in a culture chamber and embryos were collected on a grape-agar gel. Stage 16 embryos of either sex were selected based on morphology.

Dissection and Manipulation

A detailed protocol was described previously [20]. Briefly, the harvested embryos were treated with 50% bleach for 1 minute to remove their outer cuticle. They were then placed on a glass slide with the ventral side facing down. Patch pipettes were used to remove some of the internal organs such that the muscle wall and the motor neurons could be laid flat for imaging. Y-27632 (110 μM) was added 15 minutes before the FRAP experiments, and immediately before in other experiments.

Confocal Imaging

A confocal microscope (LSM 700; Zeiss) was used to obtain optical sections of the exposed axon. A 40x/1.3 objective (420462-9900; Zeiss) was used. The 488 nm laser line was used to image embryos with GFP fused to synaptotagmin, and the 555 nm laser line was used to image embryos with RFP fused to LifeAct. Image stacks were taken every 5 minutes.

FRAP Imaging

A confocal microscope (LSM 880; Zeiss) with a 488 nm laser and a 63x/1.4 objective was used. The plane which the regions of interest had the highest fluorescence was visually identified and used as the plane for bleaching. The regions of interest were bleached at 75% power for 12 μs per pixel. Bleaching was repeated 3 times. The pinhole was set to larger than optimal such that the microscope could cover the exposed axon in less than 30 seconds for each time frame, while not losing any photons that would be blocked by a smaller pinhole. Image stacks were taken every minute. All settings were kept unchanged in all FRAP experiments.

Microfludic Device

Detailed description can be found in previous work [114]. Briefly, a dissected embryo was placed on a cover slip. A slab of patterned liquid silicon rubber is positioned on top of the embryo and mounted directly to the cover slip. A suction flow is used to backfill the device to remove the bubbles trapped during assembly. A widefield fluorescence microscope (IX 81; Olympus) and a 20x objective (LCPlanFI; Olympus) was used for imaging.

Chemical Treatment

Y-27632 (110 μM, 10005583) was purchased from Cayman Chemical (Ann Arbor, MI). The concentration used was adapted from previous work also using drosophila [55, 97]. When the drug was used in microfluidic experiments, 2 droplets of food dye (McCormick) per 1 mL of the drug at the final concentration were added to aid visualization.

Image Analysis

The confocal stack acquired could be represented by the intensity field $I[x, y, z, t]$. The summation intensity projection $I_{sum}[x, t]$ performs the following operation:

$$I_{sum}[x,t] = \sum_{y=y_{min}}^{y_{max}} \sum_{z=z_{min}}^{z_{max}} I[x,y,z,t] \tag{6.1}$$

As a result, for every time frame, intensity could be plotted against the length of the axon (x). However, the axons could have some variations in length. A normalization scheme was needed to ensure a proper comparison among all axons. Simply scaling the x-axis would lead to a normalization in length but would skewed the total intensity. Therefore, we further scale the intensity (I_{norm}) such that the total intensity

remains conserved; i.e., $\sum_{\tilde{x}=0}^{\tilde{x}_{max}} I_{norm}[\tilde{x}]\Delta\tilde{x} = \sum_{x=0}^{x_{max}} I_{sum}[x]\Delta x,$:

$$I_{norm}\left[\tilde{x} = \frac{100}{x_{max}}x, t\right] = \frac{x_{max}}{100}I_{sum}[x, t] \tag{6.2}$$

The x-axis was conveniently scaled to 100 such that results could be plotted as a function of the percentage of length. The data were interpolated for every 0.33%. The first 10% of the length from the muscle end was established as the presynaptic terminal (Fig. 6.1c).

6.3 Results

F-actin disassembly precedes vesicle declustering upon tension loss

To establish that tension influences presynaptic vesicle clustering, we performed chemical treatment using Y-27632 to inhibit the ROCK pathway, previously shown to be important in axonal tension generation [55], in embryos of a recombinant fly line (elav-Gal4/syn-GFP-UAS) expressing synaptotagmin fused with GFP in neuronal cells (Fig. 6.1a & b). Synaptotagmin is a vesicle protein. By fusing it with GFP, we can correlate green fluorescence (Fig. 6.1c & d) with the amount of vesicles present in a region of interest (e.g. the presynaptic terminal). We observed a decrease in vesicle content for the 45 minutes that the embryos were under chemical treatment (Fig. 6.2a). Subsequently, we washed out the drug with PBS to rescue axonal tension and again measured the amount of vesicles for another 45 minutes; clustering was partially rescued (Fig. 6.2a).

Since F-actin appears to have a significant role in regulating vesicle clustering [134], we further conducted the same experiment to embryos expressing LifeAct fused with RFP (Fig. 6.1a & b). Employing LifeAct allowed us to correlate red fluorescence with the amount of F-actin at the presynaptic terminal. Similar to synaptic vesicles, the amount of F-actin decreased under force disruption and recovered after force recovery (Fig. 6.2b).

The green and red fluorescence intensity at the presynaptic terminal can be summed respectively and plotted against time to look at the temporal dynamics of vesicles and F-actin respectively. The time series for each embryo can be normalized to the initial intensity to aid comparison. The summary of the results for the 2 sets of experiments were shown together in (Fig. 6.2c & d). Notably, the disruption (Fig. 6.2c) and recovery (Fig. 6.2d) of F-actin appears to occur before that of vesicles. Such has motivated us to
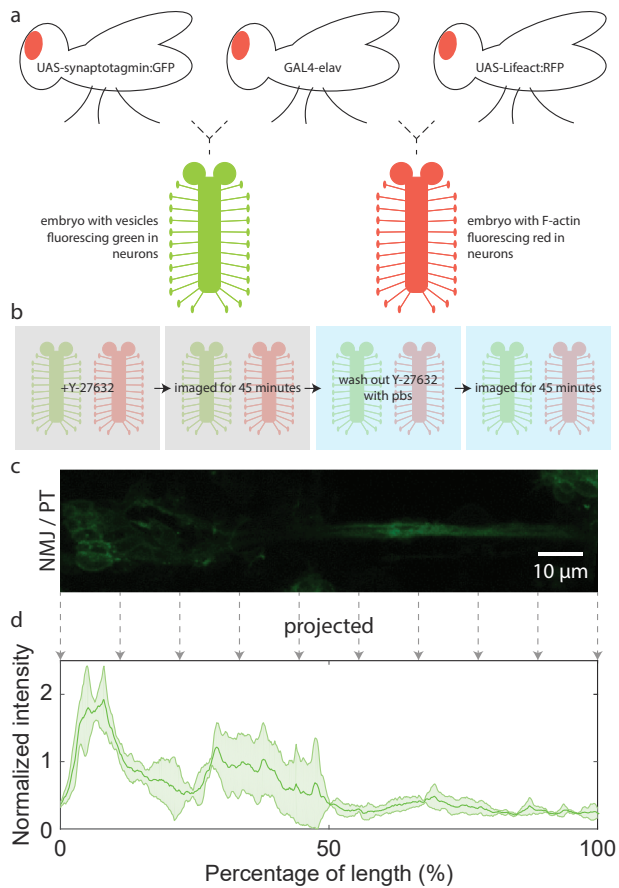
Figure 6.1: Experimental setup. a) Mutants are crossed to express synaptotagmin tagged with GFP or Lifeact tagged with RFP; these mutants serve to visualize vesicles and F-actin respectively. Embryos resulted from the crosses are then surgically prepared to expose the axons. b) The embryos are treated with a force (ROCK pathway) inhibitor, Y-27632, and imaged for 45 minutes under a confocal setup. The drugs are then washed out with pbs and the embryos are imaged for another 45 minutes. c) A stack of optical slices of the exposed axon is obtained by confocal imaging. The stack is reconstructed into a single image by summation projection. d) The image is further projected to an intensity-vs-length plot by summing the intensity values across the axon.

characterize the data by fitting each time series to an exponential function of the form $a(e^{-\frac{t}{\tau}}) + c$. The time constant, τ, for each individual fit was then extracted and averaged for both experimental groups monitoring vesicles (Fig. 6.3) and F-actin (Fig. 6.4). Our data showed that actin disruption and recovery occurred before vesicle declustering and reclustering (Fig. 6.2e), suggesting that axonal tension influence presynaptic vesicles through F-actin.

To further support the claim, we compared the spatial intensity distributions of vesicles (Fig. 6.5) and F-actin (Fig. 6.6) at the presynaptic terminals before and after treatment. Each intensity distribution is normalized to the average value of the distribution. From the data, it could be observed that the disruption and recovery for both vesicles and F-actin occurred at around the mid-region of the presynaptic terminal, supporting that their activities could be co-localized and correlated.
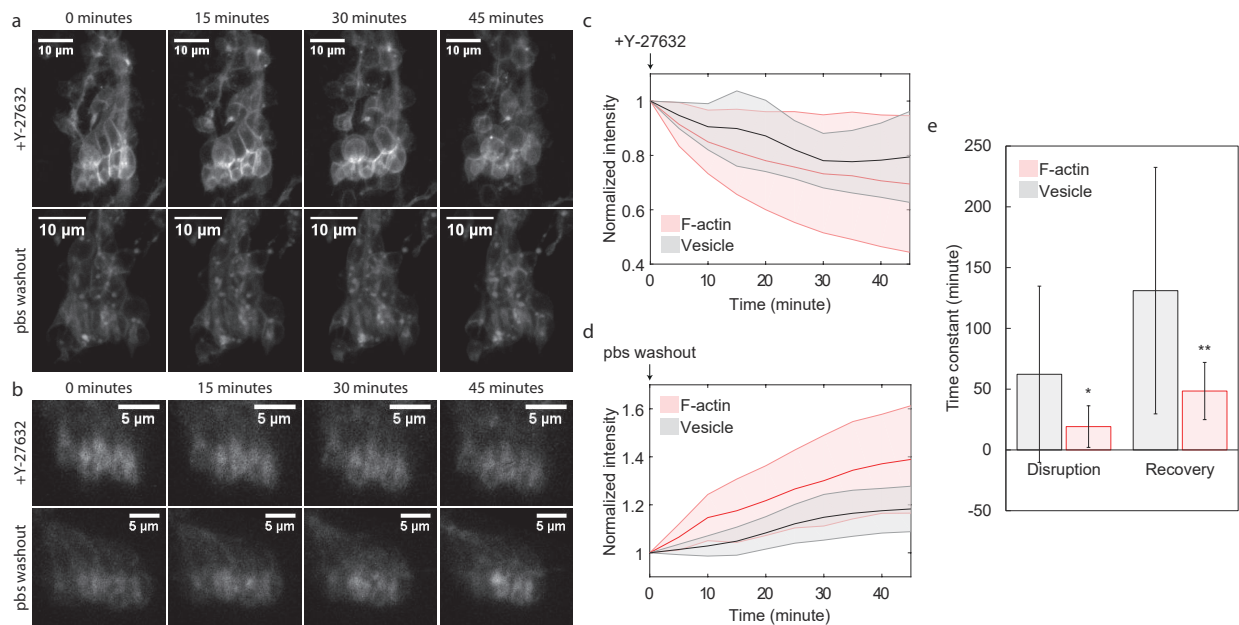
Figure 6.2: F-actin and vesicle dynamics during tension loss and recovery. a) Treating embryos with Y-27632 leads to the reduction of green fluorescence, pointing to a loss of vesicles at the presynaptic terminal. Upon pbs washout, the fluorescence (and vesicle clustering) is partially recovered. b) Similarly, red fluorescence, indicative of F-actin, diminishes under Y-27632 treatment, and recovers after pbs washout. c) The intensity reduction upon Y-27632 treatment of multiple samples are summarized. The red curve (N=7) represents F-actin reduction, while the black curve represents vesicle reduction (N=17). d) The intensity recovery upon pbs washout of multiple samples are summarized. The red curve (N=7) represents F-actin recovery, while the black curve represents vesicle recovery (N=15). Shaded regions in both c & d are standard deviation error. Intensity data are normalized to the initial value at time = 0. e) The disruption and recovery data sets of each sample are fitted individually to an exponential curve of the form $ae^{-\frac{t}{\tau}} + c$. The time constants (τ) for disruption and recovery of vesicles and F-actin are averaged respectively and shown here and—for comparing the fit with the data—in Fig. 6.3 & 6.4. In both disruption and recovery, although the overall trend is similar, F-actin activities precede that of vesicles. Error bars in standard deviations. Unpaired two-sample t-test used to obtain p-values. Fig. 6.5 & 6.6 further show the spatial difference in vesicles and F-actin intensity before and after tension relaxation and recovery.
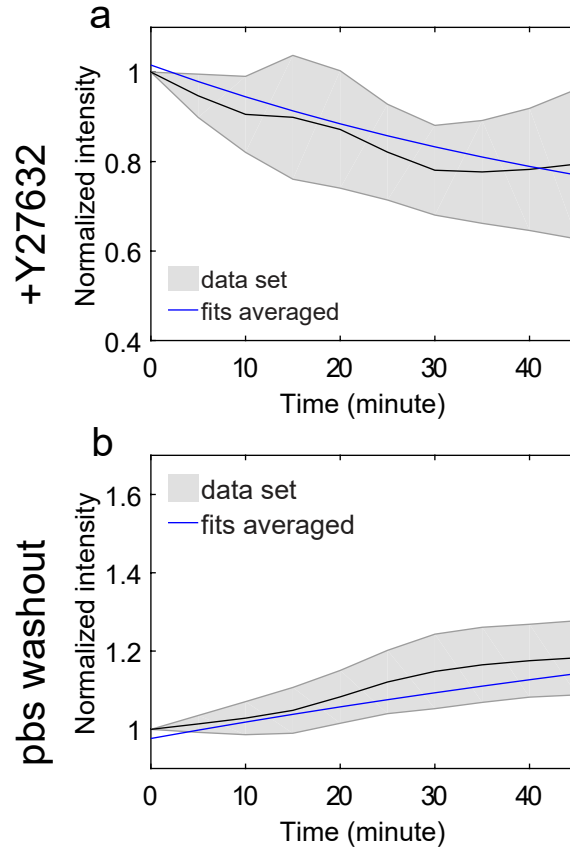
Figure 6.3: Temporal data sets of normalized vesicle intensity are fit individually to an exponential of the form $a(e^{-\frac{t}{\tau}}) + c$. The resulting best-fit parameters are averaged to generate the blue curve as a representation of the temporal dynamics of vesicle (a) declustering and (b) reclustering. Shaded regions show error in standard deviation.
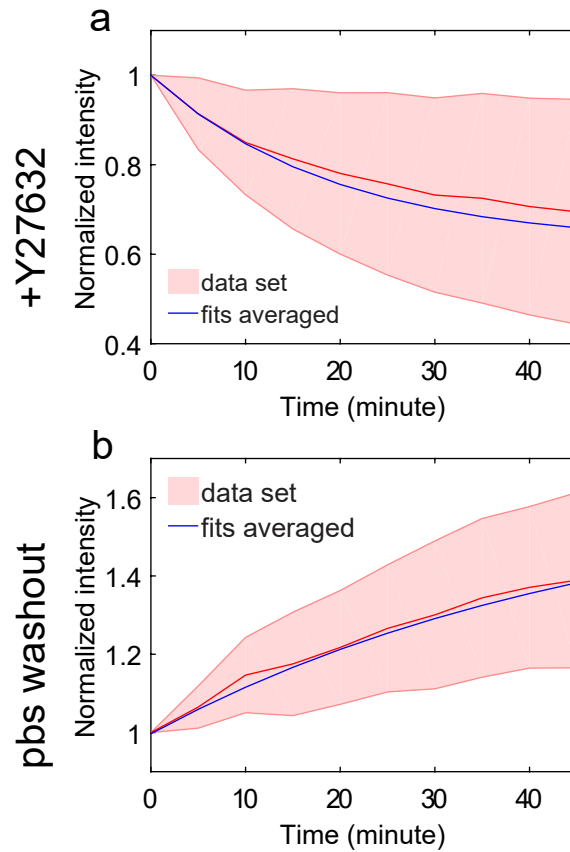
Figure 6.4: Temporal data sets of normalized F-actin intensity are fit individually to an exponential of the form $a(e^{-\frac{t}{\tau}})+c$. The resulting best-fit parameters are averaged to generate the blue curve as a representation of the temporal dynamics of F-actin (a) disassembly and (b) reassembly. Shaded regions show error in standard deviation.

Previously clustered presynaptic vesicles diffuse out of the synapse to the axon conduit upon tension loss

The disappearance of F-actin could be explained by actin disassembly, which can occur rapidly. However, the reduction in clustered vesicles could be due to 3 reasons: 1) vesicles were degraded, 2) vesicles were released, 3) vesicles moved elsewhere. Fluorescence recovery after photobleaching (FRAP) has been extensively used in studying the mobility of molecules. It utilizes a high power laser to bleach the fluorescence molecules in a region of interest. Since the bleaching is permanent, any recovery in fluorescence is due to new molecules coming into the region (Fig. 6.7a). To understand the dynamics of the vesicles after declustering, we performed FRAP at the presynaptic terminal and at a distal region of the axon.

Figure 6.5: Normalized intensity of vesicles along the length of the axon at the synaptic region before and after force (a) relaxation and (b) recovery. The intensity data of each synapse (before and after treatment combined) are normalized to a mean intensity of 1. Shaded regions show error in standard deviation.

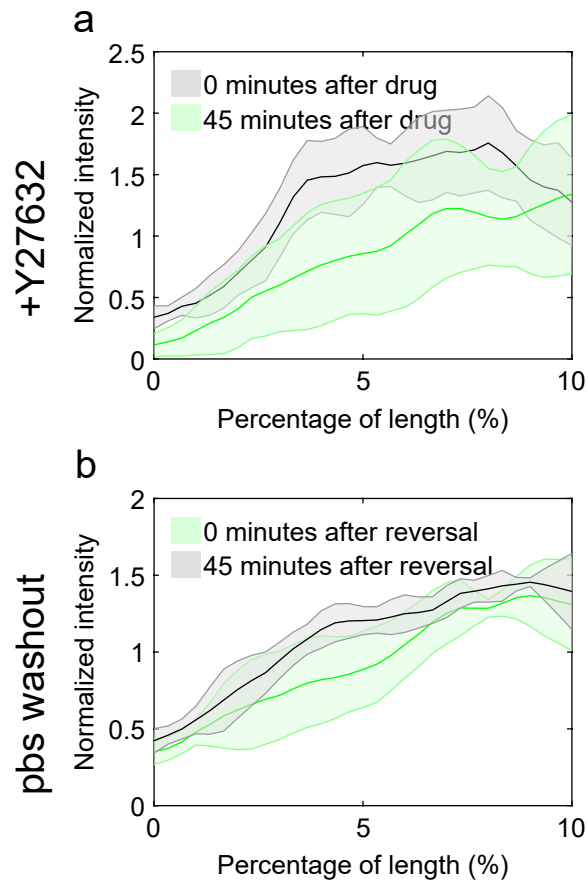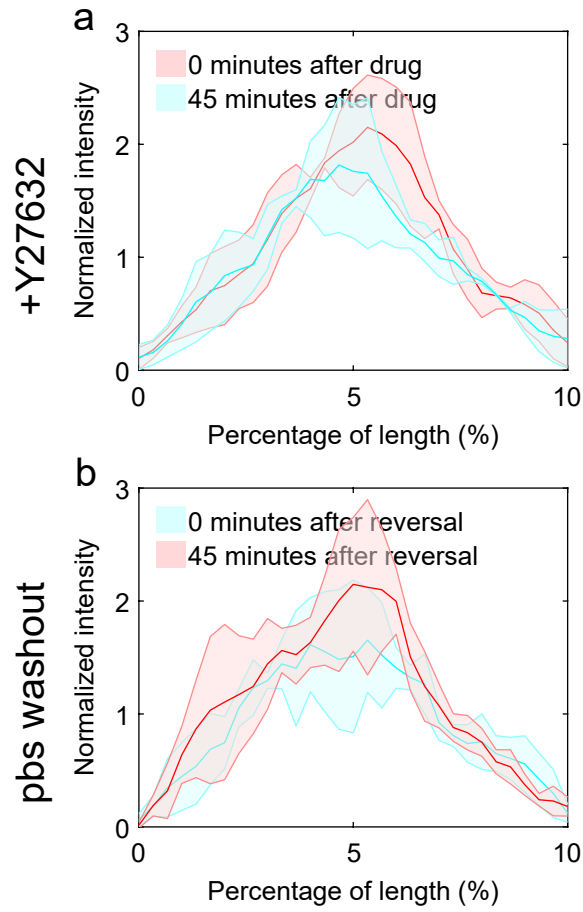Figure 6.6: Normalized intensity of F-actin along the length of the axon at the synaptic region before and after force (a) relaxation and (b) recovery. The intensity data of each synapse (before and after treatment combined) are normalized to a mean intensity of 1. Shaded regions show error in standard deviation.

At the presynaptic terminal, embryos treated with Y-27632 recovered at a slower rate compared to the control embryos not treated with Y-27632 (Fig. 6.7b). The rate could be rescued by washing out Y-27632 with pbs. The fluorescence intensity can be again summed and plotted (Fig. 6.7c), this time however normalized as $\frac{\Delta F}{\Delta F_0} = \frac{I - I_b}{I_0 - I_b}$, where I is the intensity sum at each time frame, I_b is the intensity sum post-bleach, and I_0 is the intensity sum pre-bleach. The recovery curves were therefore bound by 0 and 1 and could be compared among the different experimental conditions. The individual recovery curves were then further fit to an exponential of the form $a(e^{-\frac{t}{\tau}}) + c$. Comparing the time constants of the different conditions, we confirmed that under Y-27632 fluorescence recovery was hampered (Fig. 6.7d). The results suggest that less new vesicles came into the presynaptic terminal when tension was disrupted. Based on these findings, we hypothesized that under tension disruption the presynaptic terminal lost the ability to "store" vesicles, leading to a flux of vesicles from the presynaptic terminal to the axon conduit.

Such has motivated us to perform FRAP on the distal end of the axon conduit. The first 30% of length of the axon (not including the presynaptic terminal) was bleached (Fig. 6.8a). The fluorescence of that region was then monitored and summed across the width for each time frame. The region was split into 10 equal and non overlapping segments for analysis and comparison (Fig. 6.8b). Segments closer to the presynaptic terminal could be seen from both the images themselves (Fig. 6.8a) and the kymograph (Fig. 6.8c) to have faster fluorescence recovery under tension relaxation. The fluorescence recovery data of each segment (Fig. 6.9) were fit to an exponential of the from $a(e^{-\frac{t}{\tau}}) + c$. The extracted time constants were then averaged and plotted in both control and tension disrupted conditions against their respective segment number (Fig. 6.8d). This plot revealed that in the control samples, recovery was much slower at the segments immediately next to the presynaptic terminal (large τ). Such trend was not observed in samples with tension disrupted, and the recovery occurred at a faster rate at the extreme segments.

Together with what was observed when we perform FRAP on the presynaptic terminal, the data suggested that vesicles in axons, when unperturbed, undergo movement unidirectionally from the CNS to the synapse at the distal region of axon that we studied (Fig. 6.8e). When tension was disrupted, there was a flux of declustered vesicles from the presynaptic terminal to the axon conduit, which explained the bidirectional recovery observed (Fig. 6.8e).
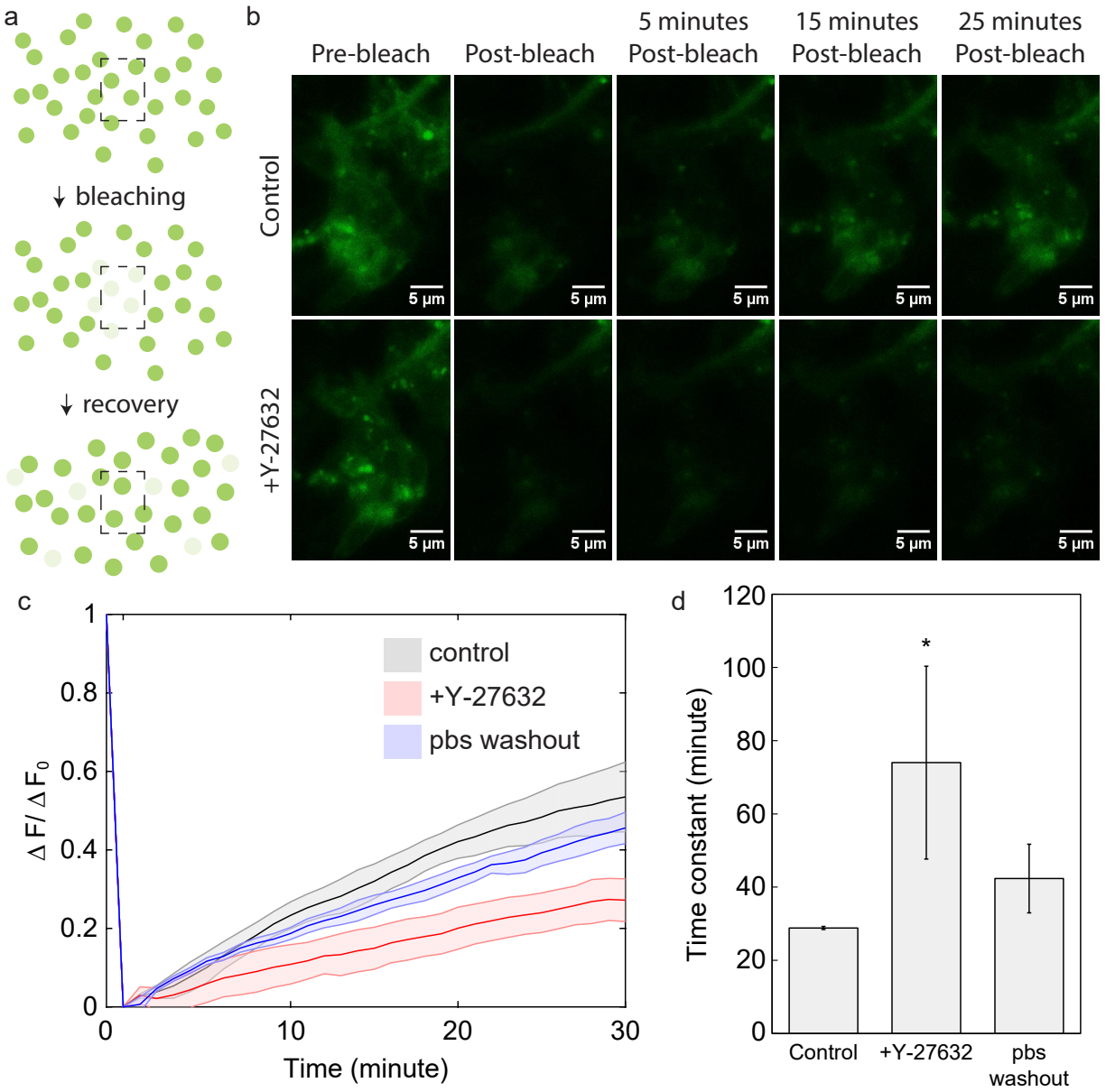
Figure 6.7: Movement of vesicles at the synapse upon tension disruption and recovery. a) FRAP allows the study of vesicle movements. It works by subjecting a region of interest to prolonged light exposure in order to photobleach the region. The region is continuously monitored after the bleaching event. When surrounding unbleached molecules move into the region of interest, fluorescence signal recovers. b) The presynaptic terminal is subjected to FRAP; fluorescence recovery is significantly hampered when samples are treated with Y-27632. c) Results for multiple samples are summarized. The intensity values are normalized to the pre-bleach (1) and post-bleach (0) values. Recovery is slower in the Y-27632 treated samples (red, N=3) compared to the control samples (black, N=3). Pbs washout restored recovery partially (blue, N=3). All shaded regions indicate error bar in standard deviation. d) Recovery data sets from all 3 conditions are fitted individually to an exponential curve of the form $ae^{-\frac{t}{\tau}} + c$. Error bars in standard deviations. Unpaired two-sample t-test used to obtain p-values.
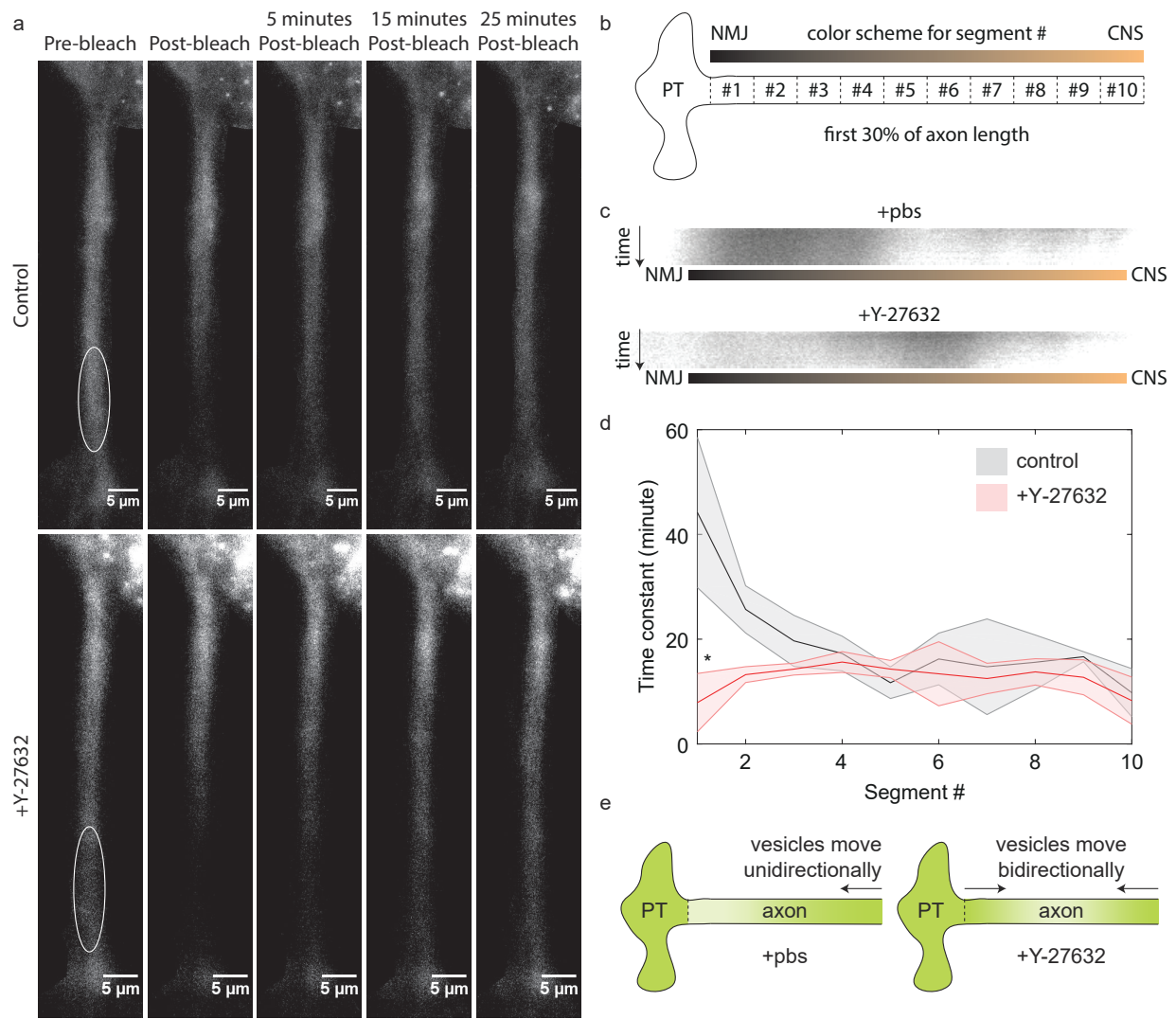
Figure 6.8: Changes in directionality of vesicle movement at axon upon tension disruption. (a) A distal region of an axon is bleached in embryos where Y-27632 is either added to the saline or not added (control). Visual inspection reveals that recovery occurs faster at regions further away from the synapse in control cases, while all regions recover at similar rate when tension is disrupted. (b) A scheme is devised, in which the bleached region, amount to around 30% of the axon length, is divided into 10 equal segments. Each segment can then be analyzed separately. (c) Kymographs of the bleached region is generated by summing the intensity laterally across the axon for each time frame. The different recovery profiles as described in (a) can be observed again. (d) For each of the 10 segments, a recovery time constant is obtained by fitting the data set, such as that shown in Fig. 6.9, to an exponential curve of the form $ae^{-\frac{t}{\tau}} + c$. The time constants are summarized and reported here. Control samples (grey, N=3) show a higher time constant at segments closer to the synapse. Tension-disrupted samples (red, N=3) show lower time constant near the synapse, and a higher time constant at the middle segments. All shaded regions indicate error bar in standard deviation. Unpaired two-sample t-test used to obtain p-values. (e) The data support a model in which vesicles move unidirectionally (towards the synapse) normally, but bidirectionally when under tension disruption.

Figure 6.9: FRAP data of each segment of (a) control and (b) treated axons are plotted according to the color gradient scheme established in the main text with darker color representing segments closer to the synapse.

Localized tension disruption of axon away from the synapse also leads to vesicle declustering

So far we have applied the chemical treatment over the entire embryo, which could lead to processes independent of axonal 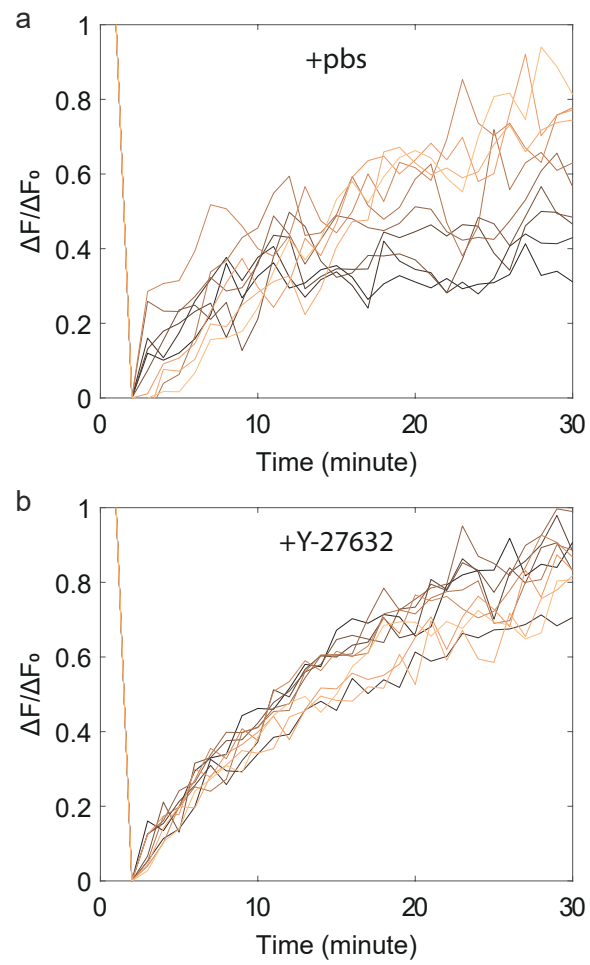force that can result in depletion of synaptic vesicles and F-actin. If chemical treatment can be localized at the axon, then we can disrupt only tension while still maintaining the integrity of the synapse and the rest of the embryo. Anything observed at the presynaptic terminal is therefore due to the loss of tension and not because of other compounding factors.

We therefore employed a microfluidic setup [114] that allowed us to perform partial treatment of the axon using the properties of laminar flow (Fig. 6.10a). A proximal region of the axon was perfused with Y-27632 to relax the motors at that region, while the rest of the neuron was perfused with pbs (Fig. 6.10a). Control axons were perfused with pbs or diluted food dye at the region of interest. We observed a stark contrast of vesicles fluorescence between control and tension disrupted axons (Fig. 6.10b). In control axons (Fig. 6.10c), vesicles were recruited into the presynaptic terminal over time possibly as part of the development process. In tension disupted axons (Fig. 6.10c), vesicles declustered over time resulting in reduced fluorescence, similar to what we observed when we applied the chemical treatment globally.

Since the synapse was kept unperturbed throughout the experiment, we concluded that vesicle clustering can be solely influenced by the tension maintained along the axon.

6.4   Discussion

Axonal tension was demonstrated in both in vitro and in vivo experiments [54, 135]. Recently, it has been shown that axons generate intrinsic tension in vivo through actin and myosin contractility [55]. By using a ROCK pathway inhibitor, we disrupted this contractility—and therefore axonal tension—and observed first F-actin disassembly and then vesicle declustering (Fig. 6.2c–e). The declustered vesicles moved from the presynaptic terminal into the axon conduit as revealed by our FRAP experiments (Fig. 6.8e). Furthermore, when we disrupted the contractility at a proximal segment of the axon conduit away from the synapse, vesicle declustering still occurred (Fig. 6.10b). Declustering with force relaxation far away from the synapse implies that tension is essential to sustain clustering, and that the tension is transmitted along the entire length of the axon as a series of force generators holding each other. Since F-actin forms cortical rings periodically along the length of the axon [38, 48], it is conceivable that axonal tension is generated

Figure 6.10: Partial treatment of axon for localized tension release leads to vesicle declustering. (a) A previously developed microfluidic device is used to partially treat a segment of an exposed axon away from the synapse. (b) Fluorescence intensity (from vesicles) at the synapse is summed and plotted when the center flow contains Y-27632 and food dye (red, N=5), just food dye (blue, N=3), or neither (black, N=4). All shaded regions indicate error bar in standard deviation. Unpaired two-sample t-test used to obtain p-values. (c) The declustering event can also be observed by visual inspection when Y-27632 is added to the center flow.

by F-actin-myosin machines pulling onto neighboring F-actin rings (Fig. 6.11a). In fact, recently it was observed that myosin expressions show a similar, but offset, periodicity of ∼190 nm to F-actin rings' [136]. Myosin filaments are ∼300 nm in length [137, 138], we therefore suspect that they are positioned at an angle to the long axis such that they can fit inside the 190 nm gaps between neighboring actin rings. This way the F-actin-myosin machines can apply coupled axial and circumferential tension as observed previously [97].

This architecture may serve another purpose. It ensures that F-actin fibers are not continuous along the axon conduit when interrupted by the actin rings. This loss of continuous F-actin prevents the vesicles from leaving the actin rich [139] presynaptic terminals where they are transported by myosin V and VI along F-actin tracks to/from the active zone [134, 140]. The above mechanism could explain our observed slower vesicle mobility (longer FRAP recovery time) at the presynaptic terminal when motors are disrupted by Y-27632 (Fig. 6.7c), since the disruption of motors leads to more passive vesicle dynamics in contrast to active motions driven by the motors.

The change of synaptic strength [141], or better known as synaptic plasticity, has major implications in learning and memory. Plasticity can occur either presynaptically [142], when more neurotransmitter vesicles are released per action potential, or postsynaptically [143], when a larger response arises per stimulation due to the increase in the number of neurotransmitter receptors. The number of synaptic vesicles available at the presynaptic terminal can therefore influence synaptic strength. Interestingly, reserve vesicles are deployed mainly during intense stimulation [144], which is also when presynaptic plasticity is observed [145, 146], suggesting that reserve vesicles and their associated clustering mechanism could play a role in presynaptic plasticity.

Of all the proteins that have been shown to influence vesicle clustering, synapsin I has been studied the most extensively [147, 148, 149]. Synapsin I is a membrane protein that has a Ca^{2+}-dependent affinity to both F-actin and the vesicle membrane [150, 69, 151], allowing it to facilitate F-actin polymerization [129], to bundle F-actin [152], and to anchor vesicles to F-actin [153]. It has been suggested that with Ca^{2+} influx during an action potential, vesicles anchored onto F-actin through synapsin I are released, and are moved away from the reserve pool [154], possibly by myosin motors [155, 156], to replenish released vesicles. We demonstrated that F-actin events precede vesicles events in all our experiments, supporting the claim that F-actin can serve as an anchoring scaffold for vesicles primed with synapsin I and other proteins [40, 130, 131]. We note that, however, several experiments have reported that disruption of F-actin by latrunculin-A did not

have significant effect on vesicle dynamics in adult frog and mouse neuromuscular junctions [157, 158, 159].

Although the short-term regulation of reserve pool size can be explained by the interaction between synapsin I and F-actin in a Ca^{2+}-dependent manner [153, 152, 154], any long-term regulation, such as those observed in presynaptic plasticity [145, 146, 160], most certainly would require alterations of the F-actin scaffold itself given that intracellular Ca^{2+} concentration is tightly regulated [161]. Based on our results that axonal tension exerts an influence on presynaptic F-actin, we suspect that neurons may utilize this tension pathway to regulate vesicle density long-term.

Taker together, we propose that F-actin network at the presynaptic terminal serves two major functions— 1) a scaffold to hold the vesicles and 2) a set of double lane highways for vesicle transport (Fig. 6.11b). Myosin II motors serve as the force generators between the anti-parallel actin fibers. This anti-parallel organization of F-actin allows bi-directional vesicle trafficking using plus-end-directed myosin V and minus-end-directed myosin VI [134]. In the axon conduit, tension is continuous along the entire length in a series fashion (Fig. 6.11a). A disruption of force at any region of the axon-synapse hard wired system results in an imbalance in force at the synapse destabilizing the synaptic actin network. Vesicles then begin to move out of the synapse by diffusion, as evidenced in our FRAP experiments. Current literature describes the molecular mechanisms of F-actin polymerization at the synapse, but this molecular view does not explain how the architecture of F-actin network is formed and how it is sustained for scaffolding and directing vesicle dynamics at the synapse. Our data closes this gap and reveals that long-range mechanical force generated by acto-myosin machinery is necessary for the emergence and sustenance of the extensive F-actin network at the synapse, and hence vesicle clustering.
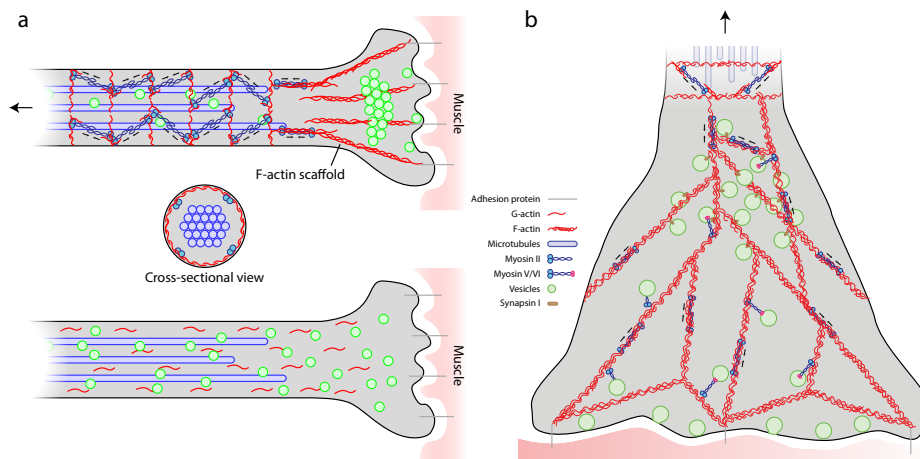
Figure 6.11: Proposed mechanistic model of vesicle clustering. (a) Axonal tension generated by F-actin and myosin motors along the axon stabilizes the F-actin network at the presynaptic terminal. The F-actin network at the presynaptic terminal provides a scaffold for vesicles to attach to. Therefore, when tension is disrupted, F-actin disassembly occurs before vesicle declustering; the declustered vesicles move proximally into the axon conduit as supported by the FRAP experiments. The microfluidic experiments further confirm the role of tension: although disruption occurs away from the presynaptic terminal, vesicles still decluster. (b) At the presynaptic terminal, F-actin can serve a dual purpose to 1) provide a scaffold for clustered vesicles and to 2) provide the physical tracks where cargo-carrying motors can transport vesicles to/from the active zone. By binding onto the F-actin scaffold through synapsin I and other proteins, vesicles can cluster at the reserve pool. Myosin II generates tension by pulling onto anti-parallel F-actin fibers, which provides force continuity to stabilize the F-actin network. The F-actin fibers can then serve as tracks for Myosin V and VI to transport vesicles.

Chapter 7

The serial nature of the tension generators along the axon

This chapter is adapted from a manuscript in preparation[1].

7.1 Motivation

Mechanical tension has been shown to play an influential role in vesicle clustering [2], vesicle dynamics [17], neural excitability [18], and axon growth [3, 4]. Studies using glass needles [54, 162], force probe [12], and fluidic flow [36] show that there exists a finite intrinsic tension in *in vitro* and *in vivo* neurons. Further evidence shows that mammalian brains also maintain a residual tension [43], which was speculated to drive cortical folding among other things [42, 44]. It is thus possible that a neuron can regulate its function by regulating its intrinsic tension.

How a neuron regulates its tension therefore warrants investigation. Many groups have shown that actin and myosin are responsible for generating tension, while microtubules act against it [32, 31, 55]. Recently, it is further revealed that axonal tension has a coupled circumferential component, pointing to the hypothesis that tension is generated by a contractile network unaligned to the axis of the axon [97]. Super-resolution microscopy reveals that F-actin forms periodic rings along the length of the axon, with connecting spectrin tetramer in between each ring [38, 48]. Myosin motors have also been shown to associate with the F-actin rings [136]. We therefore hypothesize that the contractile network could be in series and tension is transmitted along the network.

Here, we test this hypothesis by disrupting a segment of axonal cytoskeletal proteins by partial chemical treatment—if the contractile network is indeed in series, a local disruption will lead to a total loss of tension. We achieved this by using a microfluidic device that can combine partial treatment with tension measurement [114]. We modeled the axon as a slender string subjected to a shear load. Flow rate was increased in a

---

[1]Fan A, Saif MT. Partial treatment of single axons reveals a connected cytoskeleton network in generating axonal tension. In preparation

step-wise fashion to probe the elastic response of the axon. A global/partial chemical treatment could also be simultaneously applied. Such allowed us to evaluate the stiffness and rest tension of axons under partial/global F-actin, myosin, and microtubules disruption, and reveal the underlying architecture of the tension network.

7.2   Materials & Methods

Drosophila culture

Drosophila culture followed standard procedure [20]. The fly line expressing green fluorescence protein (GFP) on neuronal membranes (5146) was purchased from Bloomington stock center (Bloomington, IN). Flies were placed in a culture chamber and embryos were collected on a grape-agar gel. Embryos of stage 16 were selected based on morphology.

Microfluidics setup

Sample preparation followed an established protocol [114]. Briefly, a dissected embryo was placed on a cover slip (12-545H; Fisher Scientific, Hampton, NH). A slab of patterned liquid silicon rubber (Bluestar LSR-4305) is positioned on top of the embryo and mounted directly to the cover slip. A suction flow is used to backfill the device to remove the bubbles trapped during assembly.

Chemical treatment

Cytochalasin D (50 μg/mL), Nocodazole (15 μg/mL), Y-27632 (110 μM) were applied to the center flow to either partially or globally inhibit the respective proteins. Cytochalasin D and nocodazole were purchased from Sigma-Aldrich (St. Louis, MO) and Y-27632 from Cayman Chemical (Ann Arbor, MI).

Imaging

An inverted microscope (IX81; Olympus, Center Valley, PA) with standard GFP and mCherry filters was used. All images were acquired using a 20x/0.4 lens (LCPlanFI; Olympus, Center Valley, PA). Exposure time for axon imaging is set to 300ms. Red fluorescent beads of 0.1 μm in diameter (F8801; Thermo Fisher Scientific, Waltham, MA) were placed at the bottom of the glass slide (exposed to air). The best focal planes of the beads and the axon were identified. The distance d between the 2 planes minus the thickness t of the glass slide provided the elevation of the axon from the glass surface (Fig. 7.1a).
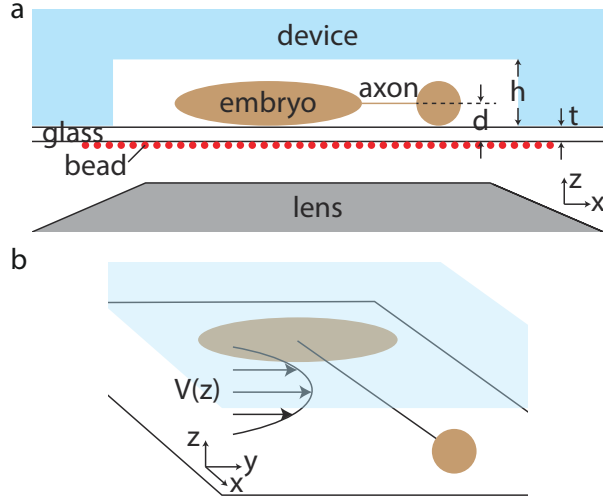
Figure 7.1: Schematics of the device. (a) A side-view of the device illustrating the position of the red fluorescence beads and their role in determining the elevation of the exposed axon, $z_a = d - t$. (b) The elevation of the exposed axon is important in determining the flow rate at that z-plane, which governs the shear load felt by the axon.

Mechanics Model

The elevation of the axon, z_a, is important because the flow velocity is a function of such. Our device can be approximated as a parallel plate setup (Fig. 7.1b) since the width w is much larger than the height h. Given the no-slip boundary condition at the fluid-solid interface and the laminar flow condition at low Reynold's number, the flow profile is:

$$V(z) = V_{max}(1 - 4\frac{z^2}{h^2})$$ (7.1)

where z is the direction perpendicular to the top and bottom surface, and z=0 is the mid-plane of the chamber parallel to the top and bottom surface. The constant V_{max} could be determined by integrating $V(z)$ over z multiplied by the width, and matching the applied volumetric flow rate, Q_{app}, from the syringe pump:

$$Q_{app} = w \int_{-\frac{h}{2}}^{\frac{h}{2}} V(z)dz = V_{max}w \int_{-\frac{h}{2}}^{\frac{h}{2}} (1 - 4\frac{z^2}{h^2})dz$$ (7.2)
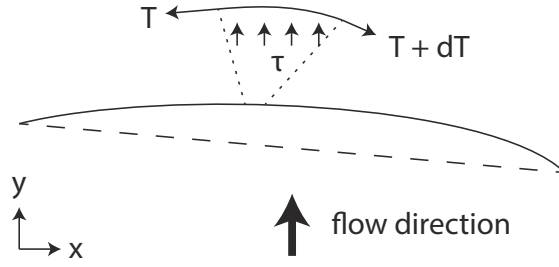
Figure 7.2: Free body diagram of the axon under a distributed load τ induced by the fluid flow.

As a result, the flow velocity felt by the axon is:

$$V(z_a) = \frac{Q_{app}}{w \int_{-\frac{h}{2}}^{\frac{h}{2}} (1 - 4\frac{z^2}{h^2})dz}(1 - 4\frac{z_a^2}{h^2}) \tag{7.3}$$

The flow velocity can then be further converted to a shear load, given by $\tau = \frac{4\pi\mu V}{ln(\frac{3.7\nu}{rV})}$ [163], where μ is the dynamic viscosity, ν is the kinematic viscosity, and r is the radius of the axon.

The shear load would lead to a force balance (Fig. 7.2) in the form of:

$$dT_x = 0 \tag{7.4}$$

$$dT_y = \tau dx \tag{7.5}$$

Eq. 7.4 & 7.5 can be rewritten as:

$$T_0 \, cos\theta_0 = T \, cos\theta \tag{7.6}$$

$$d(T \, sin\theta) = \tau dx \tag{7.7}$$

where T_0 and θ_0 indicates the tension and angle at the origin. Eq. 7.7 can then be reformulated to:

$$d(T_0 \, cos\theta_0 \frac{dy}{dx}) = \tau dx \tag{7.8}$$

By performing integrations and applying the appropriate boundary conditions: 1) $y(x = 0) = 0$, and 2) $\frac{dy}{dx}\big|_{x=0} = tan\theta_0$, we arrived at the following expression for the profile of the axon subjected to a shear load

110

of τ:

$$y = \underbrace{\frac{\tau}{2T_0\,cos\theta_0}}_{A[t]}\,x^2 + \underbrace{\tan\theta_0}_{B[t]}\,x \tag{7.9}$$

The profile of the axon was obtained from image analysis. The identified points along the axon were expressed as x-y coordinates. The points were then fit to Eq. 7.9 to obtain the constants A and B for each frame t with the point closest to the central nervous system (CNS) as the origin. By substituting Eq. 7.6 to Eq. 7.9, tension can also be expressed as

$$T[t] = \frac{\tau}{2A[t]cos\theta} \tag{7.10}$$

$$= \frac{\tau}{2A[t]}\sqrt{1+\left(\frac{dy}{dx}\right)^2} \tag{7.11}$$

$$\overline{T}[t] = \frac{\tau}{2A[t]}\frac{\int ds[t]}{\int dx} \tag{7.12}$$

where $\overline{T}$ is the average tension along the axon, $\int ds$ is the arc length of the axon, and $\int dx$ is the projected length of the axon perpendicular to the flow direction. The arc length can be evaluated by using the equation Eq 7.9. The difference in arc length over time will also provide the displacement of the axon. The projected length does not vary significantly with time because it is perpendicular to the flow direction and thus can be prescribed based on the images.

Image Analysis

The following procedures were performed by a custom code written in MATLAB (Fig 7.3). Image intensity profile along the y-axis for every x was collected and smoothed. Intensity peaks falling between predefined minimum and maximum widths and satisfying a minimum prominence were obtained. The obtained peak points were further screened for continuity to identify the axon. The profile of the axon (now in x-y coordinate) was then translated such that the point closest to the CNS was at the origin. The profile was subsequently fitted to a quadratic function. The parameters $A[t]$ and $B[t]$ in Eq. 7.9 could then be obtained and were used to calculate the average tension and the path length of the axon.
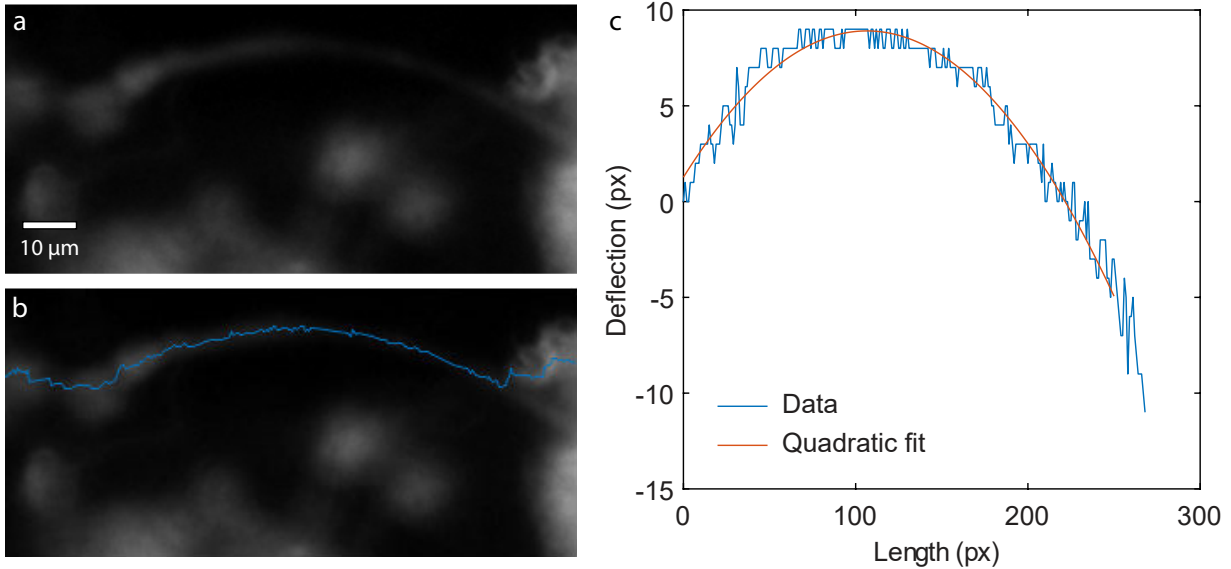
Figure 7.3: An axon (a) before and (b) after image analysis. The blue line in b traces the profile of the axon. (c) An obtained axon profile is translated such that the point closest to the CNS is at the origin. The profile is fitted to a quadratic function and the coefficients A and B in Eq. 9 (main text) is obtained.

7.3   Results

Stiffness and rest tension of axon

The ability to calculate tension using the profile of the axon enabled us to perform a loading experiment by increasing the flow rate. Therefore, we held the flow rate at 0, 20, 40, 60, 100, 140, and 200 μL/min respectively for approximately 3 minutes at each step. The immediate elastic response as captured by the dotted line in Fig. 7.4 were used to calculate displacement (path length difference) and the change in average tension. A load vs. displacement plot could then be obtained by adding the elastic response sequentially. This procedure allows us to look at the pure elastic response of the axon with minimal influence from the viscous response.

The load-displacement plot conforms to a linear function with the slope being the stiffness and the y-intercept being the rest tension (Fig. 7.5a). Since stiffness is length dependent—a longer axon under the same load will lead to a larger deflection, we plotted the stiffness value for each axon tested with respect to their rest length (Fig. 7.5b). A 1/length scaling was observed as expected. Further comparing to existing literature we found that PC12 axons of 100 - 200 μm in length had stiffness values of 0.4 - 0.5 nN/μm [162, 36, 32], matching our results here. We also observed a rest tension range of 0.1 to 3.5 nN (Fig. 7.5c),

112
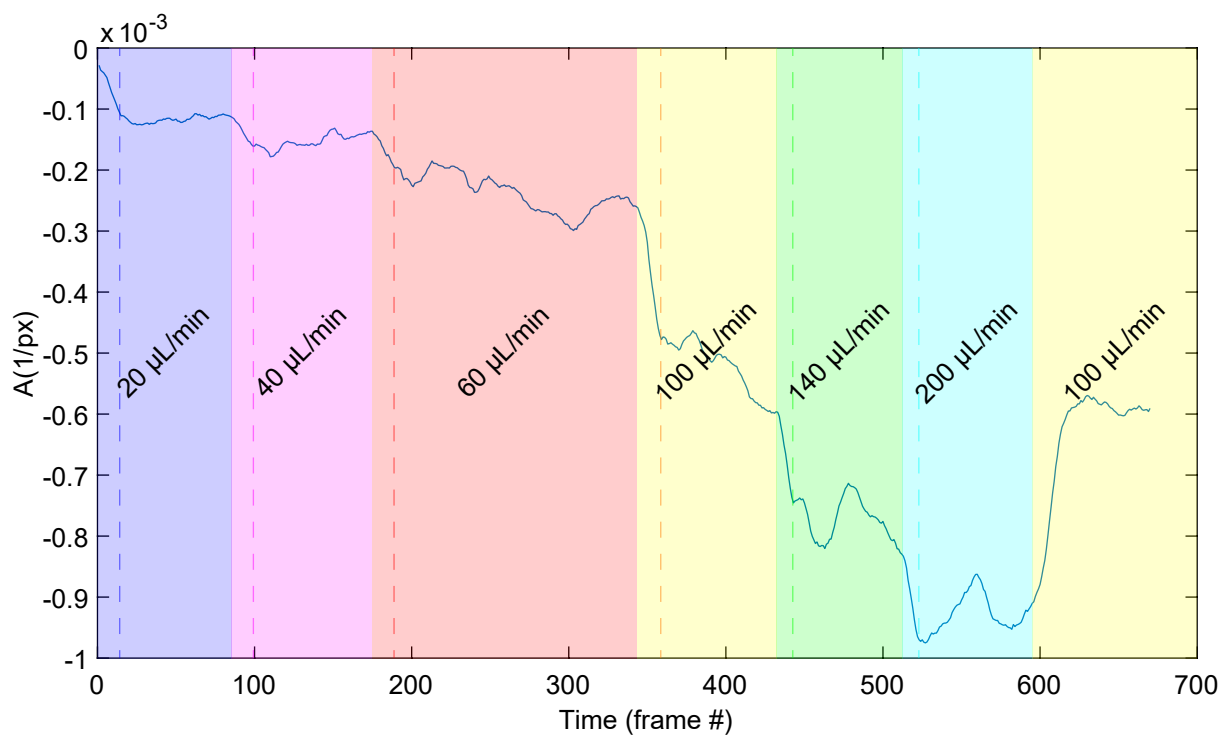
Figure 7.4: A sample profile of the coefficient A under the influence of increasing flow rate from 20 to 100 μL/min. The dotted line in each region indicates the immediate elastic response after the increased load.
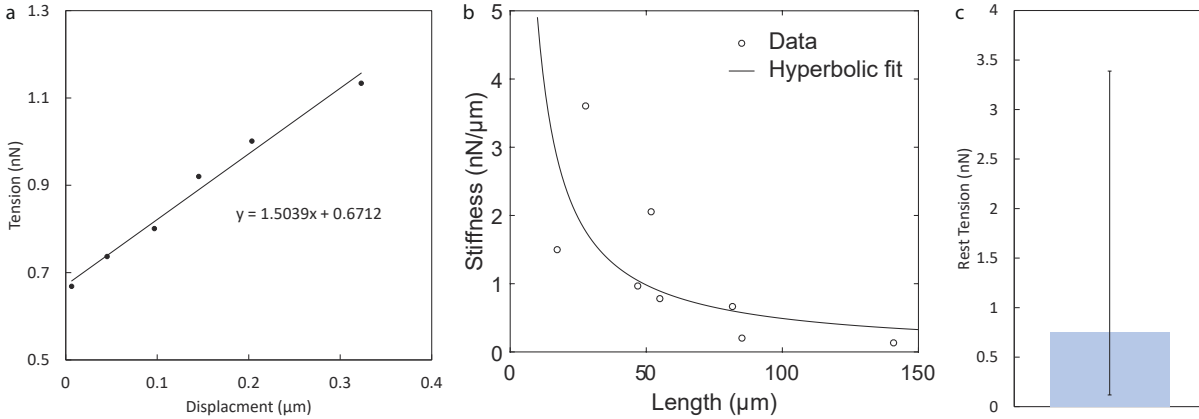
Figure 7.5: Stiffness and rest tension measurements. (a) A load-displacement curve of an untreated axon. By definition, the slope and constant of the linear fit gives the stiffness and rest tension of the axon respectively. (b) Stiffness values of 8 tested axons are reported here. We assess the length (L) dependency of stiffness (K) by fitting $K = \frac{C}{L}$ to the data, as indicated by the black curve. (c) Rest tension values of the 8 axons are summarized here. Error bars showing the minimum and maximum tension values.

agreeing with that reported previously both *in vitro* [162, 36] and *in vivo* [12].

Partial F-actin and myosin disruption can lead to total tension loss without changing an axon's elasticity

After confirming the validity of our setup by comparing our tension and stiffness measurements to that found in the literature, we can then make use of the advantages unique in our setup—the ability to do partial treatment on an insuspendable sample. A flow containing cytochalasin D or Y-27632 were applied through one of the center channels (Fig. 7.6). At the same time, the side channels applied the appropriate flow rate such that the central flow can be focused onto only a portion of the axon (∼30 μm [114]). To achieve partial treatment at all times, the total flow rate had to be kept high. Therefore, we held the flow rate at 100 μL/min for 10 minutes. Then the axon was loaded twice more at 140 and 200 μL/min. After the loading paradigm, the flow rate was brought back to 100 μL/min and held for another 10 minutes. However, the central flow was switched off in this case. This way, we intended to wash out the effect of the chemical treatment. The axon was again loaded at 140 and 200 μL/min after the washout. We then repeated the same procedure as described in the previous section to obtain the load-displacement plots that allowed us to calculate stiffness and rest tension.

Both F-actin and myosin disruption led to a decrease in rest tension to a negative value, while stiffness
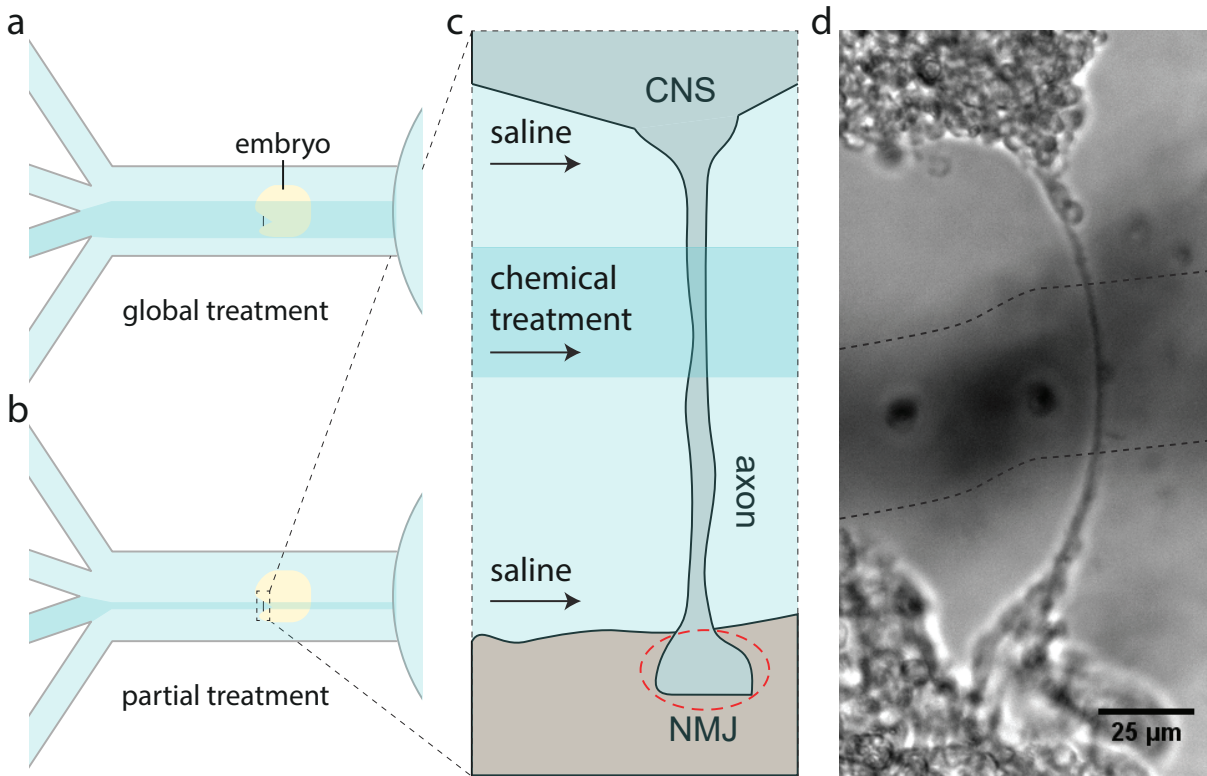
114

Figure 7.6: Schematics of (a) global and (b) partial treatments. (c) An expanded schematic of an axon under partial treatment. Only a portion of the axon length is subjected to chemical treatment. (d) An experimental image showing the partial treatment. Contrast created by added food dye.

remained largely unchanged (Fig, 7.7a & b). A negative rest tension has no physical meaning, but it points to that when tension is zero, the displacement is finite and the axon would remain curved. We checked that by unloading the axon in a few cases immediately after the partial treatment. The axons did remain curved. This observation is similar to those observed previously in another study where axons were buckled under the influence of acto-myosin disruption. Those axons would remain buckled since contractility was hampered.

Partial and global microtubules disruption can lead to axon softening without changing an axon's rest tension

Microtubules are known to provide the structural stiffness for axons [1]. This led us to treat axons with nocodazole to disrupt microtubules both partially and globally to investigate if such would affect the slope in our load-displacement plots. Indeed, stiffness after washout increased several folds, but rest tension remained the same (Fig. 7.7c).

We further compared all our results by dividing the stiffness and tension values in the treatment cases with those in the respective washout cases. This way we compare the same axon with disruption and without disruption. We observed a similar trend that microtubules disruption led to a decrease in stiffness but not rest tension, and acto-myosin disruption led to a decrease in rest tension but not stiffness (Fig. 7.7d & e). The magnitude of stiffness decrease was more pronounced in global microtubules disruption (Fig. 7.7d). We therefore inspected the experimental images and observed that since microtubules disruption was localized in the partial treatment cases, the axons retained some of their structural stiffness in the untreated regions (Fig. 7.7f & g).

7.4   Discussion

In this study, we employed a microfluidic setup [114] that can perform partial treatment on insuspendable samples to 1) measure the elastic response of an exposed axon, and 2) disrupt F-actin, myosin motors, and microtubules locally at a segment of the axon conduit. This unique approach allowed us to investigate the underlying architecture of the cytoskeletal network.

We revealed that a local F-actin or myosin disruption could lead to a complete intrinsic tension loss without effecting the elastic properties of the axon. We reasoned that this observation could be explained
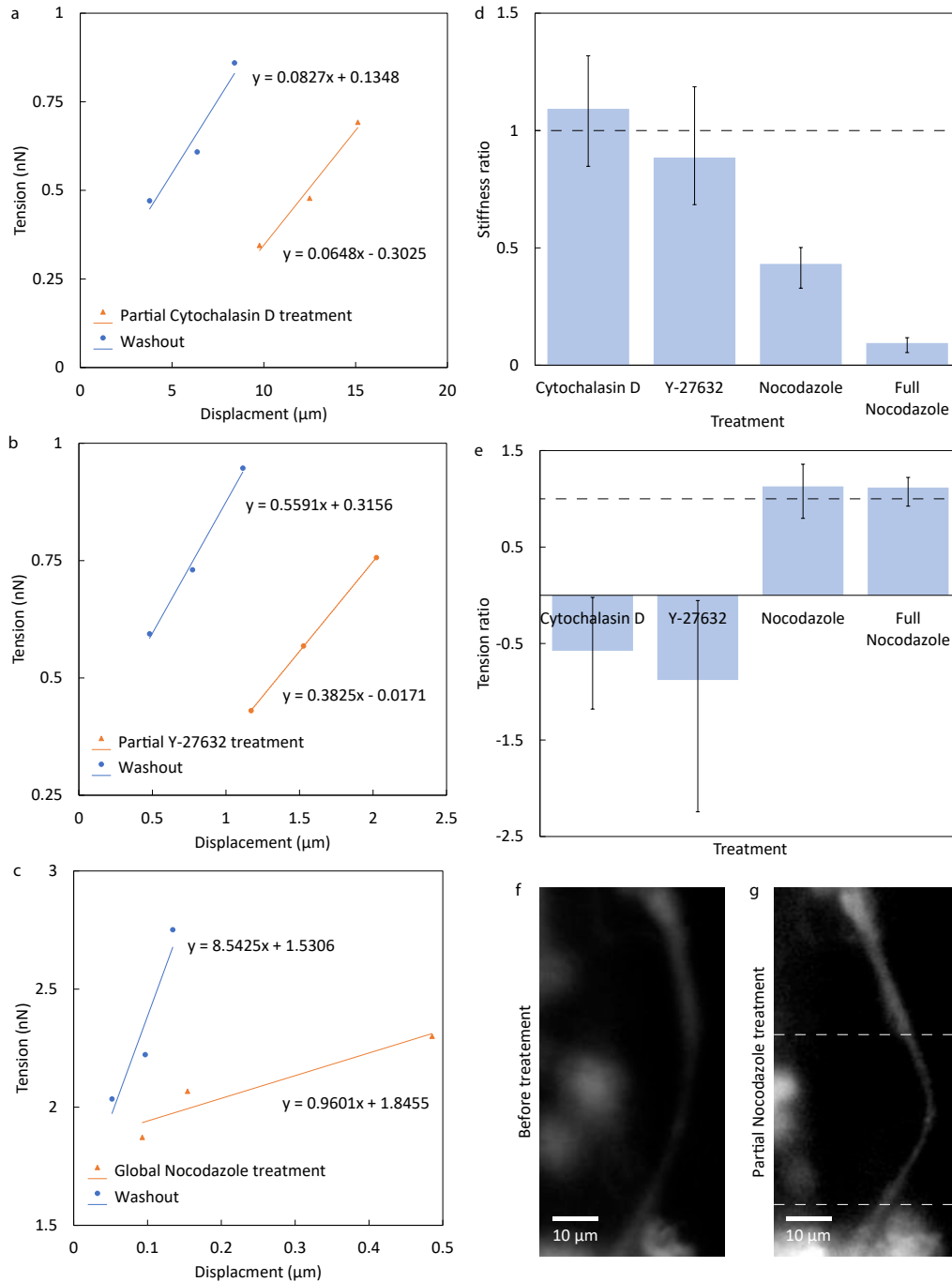
Figure 7.7: Effects of chemical treatments on axonal stiffness and rest tension. Load-displacement curves of axons under partial treatment (red) and subsequent pbs washout (blue) using (a) cytochalasin D and (b) Y-27632 to target F-actin and myosin motors respectively. (c) Load-displacement curves of axons under global treatment (red) and subsequent pbs washout (blue) using nocodazole to target microtubules. (d) Stiffness and (e) tension ratios are obtained by dividing the stiffness and rest tension values under drug disruption with those after washout respectively. The values for all conditions are compared. Dotted lines indicate a ratio of 1 expected for unchanged values. Error bars showing minimum and maximum values. An axon (f) before and (g) after partial microtubules disruption is shown. Chemical treatment is applied at the region between the dotted lines, which leads to a more pronounced curvature compared to the other regions.

by a connected network of acto-myosin contractile units (Fig. 7.8). A failure to transmit tension at any point would lead to a total loss of tension, since the rest of the network lost the anchor points for contractile motion, and hence tension generation, to happen. The undisrupted proteins might have other anchor points, especially to the cell membrane. The cell membrane alone however may not be able to sustain force because of its fluidic nature.

Microtubules disruption, on the other hand, led to a concentrated loss of microtubules at the region of treatment affecting the stiffness partially, but not the intrinsic tension. This observation agrees with the current view that microtubules plays a passive role in tension generation in axons; they provide resistance to the contractile motion of F-actin and myosin motors, but do not actively generate a force [55].

A recent study provided the functional insight for our experiments here. Using the same partial treatment system, the study revealed that a local myosin motors disruption can lead to presynaptic vesicle declustering with a magnitude similar to that of global myosin motors disruption. Using the results of the current study, we reasoned that the similarity in magnitude in both global and local disruption is due to a total tension loss in the connected tension network. Thus, it is possible that a neuron can regulate its synaptic efficacy—which occurs at the distal end—by regulating mechanical tension at the proximal region of its axon or even its cell body.

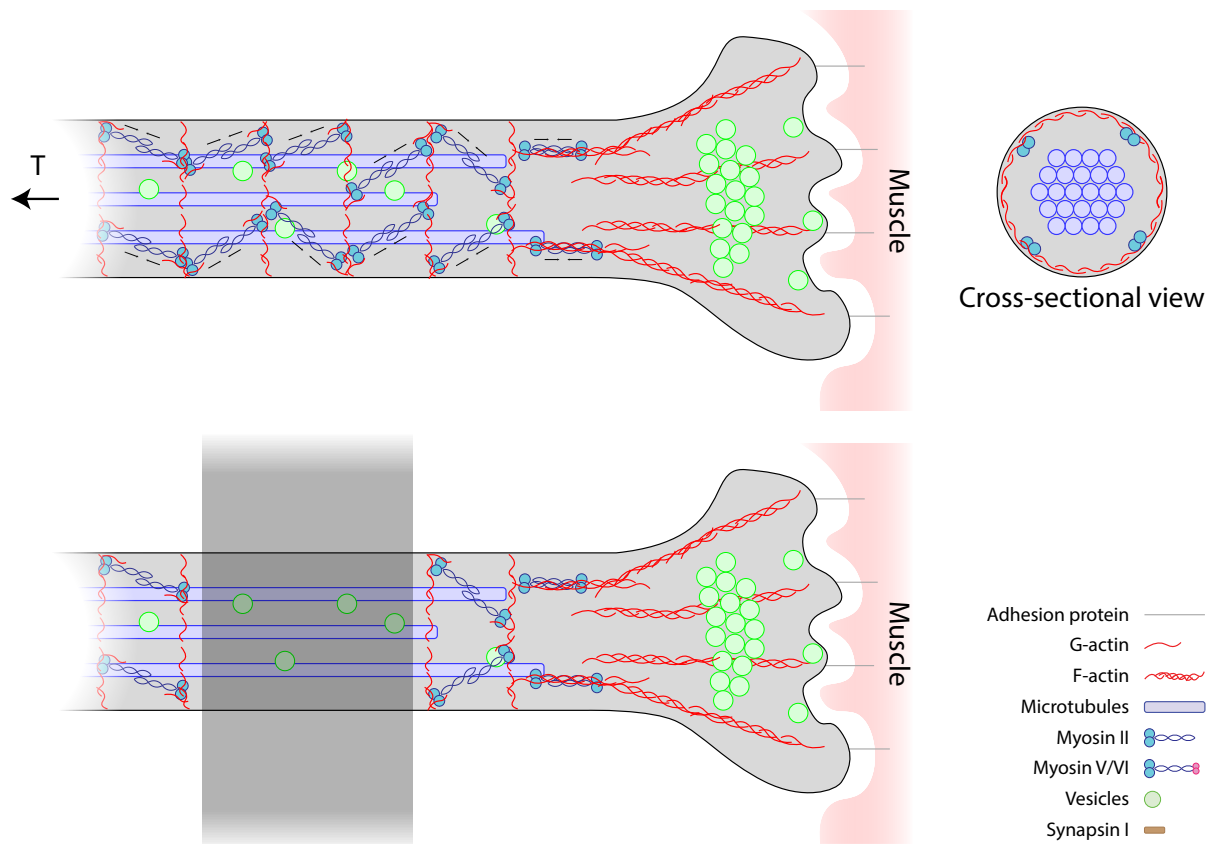Figure 7.8: An illustration of the tension generating contractile network. (top) F-actin rings and myosin motors form periodic intercalating units that are actively contractile to generate tension. (bottom) When a disruption occurs locally (black band), the intact units lose the connections in between. Contractile motion might still occur but a tension is not sustained leading to total tension loss.

Chapter 8

Conclusions and Future Works

In this dissertation, I revealed that the mechanical tension maintained by the neurons themselves can regulate presynaptic vesicle clustering through a previously unknown biophysical mechanism: tension along the axon stabilizes a presynaptic actin-rich scaffold, which provides an anchorage for vesicles to accumulate. This implies that neurons can potentially modulate their synaptic strength (important in learning and memory) through changing their tension state. The discovery can be broken down into 4 different but related findings:

1. **Axons maintain tension through actin and myosin.** Vesicles cluster naturally at the presynaptic terminal, and tension is necessary for the vesicles to cluster. So it seems that either neurons maintain a tension themselves, or the surrounding tissues are pulling onto the neurons. To distinguish between the two, I slackened in vivo fruit fly axons to observe if they can contract to generate tension themselves. Axons exhibited contractility and recovered the taut profile in less than 4 minutes. This contractility was significantly hampered under the inhibition of myosin motors and disruption of actin filaments, leading to the conclusion that actin and myosin generate tension in axon.

2. **Actin and myosin also maintain tension in the circumferential direction.** Actin in axons, however, has a cortical ring-like structure. These actin rings are periodic along the length. This raised the possibility that actin and myosin are also generating tension in the circumferential direction. To study this, I used confocal microscopy and spatial light interference microscopy (in collaboration with Prof. Gabriel Popescu) to monitor the diameter of axons over time. Both imaging modalities revealed that diameter increased when actin or myosin were disrupted, and decreased when microtubules were disrupted. This suggests that actin and myosin are constantly applying a circumferential tension onto the content, mostly microtubules, of the axon. I further demonstrated, through stretching and relaxing the axon with a piezo-manipulator, that tension was coupled in the axial and circumferential direction.

3. **Axonal tension sustains presynaptic F-actin to recruit vesicles and stop vesicles from diffusing back into the axon.** Since axons maintain its own axial and circumferential tension by actin and myosin, I then asked how these proteins could influence vesicle clustering. This would point

120

to the mechanistic pathway that neurons employ to regulate vesicle clustering with mechanical tension. I investigated this by inhibiting myosin motors and observing vesicle declustering. Vesicle declustered as a result of myosin loss. Interestingly, under myosin inhibition, actin filaments at the presynaptic terminal also disassembled, and do so before vesicles declustered. It appears that actin disassembly occurs before vesicle declustering in the cascade of events, pointing to a presynaptic actin scaffold.

The declustered vesicles have to go somewhere. To account for their dynamics, I employed a technique called fluorescence recovery after photobleaching (FRAP). This allows the study of the movement of the fluorescing vesicles. Using this technique, I observed less vesicles moving into the synapse and more vesicles moving into the distal region of the axon when the samples were under myosin inhibition. Therefore, I concluded that declustered vesicles moved into the axon conduit.

One problem with chemical inhibition of proteins is that it has no spatial specificity. In our case, all the myosin motors were inhibited. This limits the interpretation of any observations to myosin dependent, not (myosin-generated) tension dependent. For this reason, I developed a microfluidic platform that can perform partial treatment on a small tissue sample. I used the platform to inhibit myosin motors at a proximal segment of the axon, therefore leaving the myosin motors at the presynaptic terminal intact. Declustering events still occurred under partial treatment, suggesting that the tension generated by myosin motors, but not myosin motors themselves, regulated the process.

4. **Axonal tension is in series in nature.** Given the observation that a partial tension disruption can lead to declustering of equal magnitude to that induced by a global disruption, I hypothesize that the tension generators are in series in nature. To test this hypothesis, I used the same partial treatment setup to disrupt F-actin, myosin, and microtubules respectively locally at a segment of the axon while simultaneously load the axon by increasing the flow rate. The experiments show that a partial F-actin or myosin disruption can lead to a total tension loss supporting that the tension-generating contractile network is connected in a in-series fashion along the length of the axon.

Collectively, I demonstrated that 2 contractile proteins, actin and myosin, maintain an intrinsic tension along the axon both axially and circumferentially. These contractile proteins stabilize a presynaptic actin-rich scaffold, which allows vesicles to act against diffusion to accumulate at the synapse. When these proteins are disrupted, the scaffold disassembles, and vesicles diffuse back into the axon conduit. Tension from myosin motors along the axon—but not the motors themselves—sustains this process, possibly through activating the catch bonds in the F-actin scaffold. This biophysical pathway provides the first evidence that an axon can perform strength modulation on its synaptic connections, a key process in our understanding of learning and memory, through regulating its own mechanical tension.

A future avenue could be that of further relating mechanical tension to neural function. I discussed here that vesicle clustering can be regulated by mechanical tension, but the effect of an increase pool of vesicles has yet to be demonstrated to influence 1) release rate and magnitude, and 2) the evoked potential at the postsynaptic terminal. These 2 themes can be tested by experiments in the cellular scale in using neurons stemming from embryonic bodies or from living animals.

Some diseases such as traumatic brain injury can also be caused by the alteration in tension by an external or internal event. Therefore, comparing the tension state of animals with and without the disease of interest would illuminate the role of tension in it. In order to acheive this, a robust and non-invasive method to measure physiological forces at high spatial and temporal resolution is necessary. This is why I also believe a new tool to map mechanical forces systematically will produce many interesting discoveries related to the field of neuromechanics.

References

[1] Eric Kandel, James Schwartz, Thomas Jessell, Steven Siegelbaum, and A. J. Hudspeth. *Principles of Neural Science, Fifth Edition*. McGraw Hill Professional, September 2012.

[2] Scott Siechen, Shengyuan Yang, Akira Chiba, and Taher Saif. Mechanical tension contributes to clustering of neurotransmitter vesicles at presynaptic terminals. *Proceedings of the National Academy of Sciences of the United States of America*, 106(31):12611–6, August 2009.

[3] D Bray. Axonal growth in response to experimentally applied mechanical tension. *Developmental biology*, 102(2):379–89, April 1984.

[4] Bryan J Pfister, Akira Iwata, David F Meaney, and Douglas H Smith. Extreme stretch growth of integrated axons. *The Journal of neuroscience : the official journal of the Society for Neuroscience*, 24(36):7978–83, September 2004.

[5] Bryan J Pfister, David P Bonislawski, Douglas H Smith, and Akiva S Cohen. Stretch-grown axons retain the ability to transmit active electrical signals. *FEBS letters*, 580(14):3525–31, June 2006.

[6] C Lockyer. Growth and energy budgets of large baleen whales from the Southern Hemisphere. *Mammals in the seas*, January 1981.

[7] S R Heidemann and R E Buxbaum. Tension as a regulator and integrator of axonal growth. *Cell motility and the cytoskeleton*, 17(1):6–10, January 1990.

[8] Matthew O'Toole, Phillip Lamoureux, and Kyle E Miller. Measurement of subcellular force generation in neurons. *Biophysical journal*, 108(5):1027–37, March 2015.

[9] T J Dennerll, P Lamoureux, R E Buxbaum, and S R Heidemann. The cytomechanics of axonal elongation and retraction. *The Journal of cell biology*, 109(6 Pt 1):3073–83, December 1989.

[10] S Chada, P Lamoureux, R E Buxbaum, and S R Heidemann. Cytomechanics of neurite outgrowth from chick brain neurons. *Journal of cell science*, 110 (Pt 10):1179–86, May 1997.

[11] Joseph R Loverde, Vivian C Ozoka, Robert Aquino, Ling Lin, and Bryan J Pfister. Live imaging of axon stretch growth in embryonic and adult neurons. *Journal of neurotrauma*, 28(11):2389–403, November 2011.

[12] Jagannathan Rajagopalan, Alireza Tofangchi, and M Taher A Saif. Drosophila neurons actively regulate axonal tension in vivo. *Biophysical journal*, 99(10):3208–15, November 2010.

[13] G Shaw and D Bray. Movement and extension of isolated growth cones. *Experimental cell research*, 104(1):55–62, January 1977.

[14] Gianluca Gallo. Myosin II activity is required for severing-induced axon retraction in vitro. *Experimental neurology*, 189(1):112–21, September 2004.

[15] E B George, B F Schneider, R J Lasek, and M J Katz. Axonal shortening and the mechanisms of axonal motility. *Cell motility and the cytoskeleton*, 9(1):48–59, January 1988.

[16] H C Joshi, D Chu, R E Buxbaum, and S R Heidemann. Tension and compression in the cytoskeleton of PC 12 neurites. *The Journal of cell biology*, 101(3):697–705, September 1985.

[17] W W Ahmed, T C Li, S S Rubakhin, A Chiba, J V Sweedler, and T A Saif. Mechanical tension modulates local and global vesicle dynamics in neurons. *Cellular and molecular bioengineering*, 5(2):155–164, June 2012.

[18] Anthony Fan, Kevin A Stebbings, Daniel A Llano, and Taher Saif. Stretch induced hyperexcitability of mice callosal pathway. *Frontiers in cellular neuroscience*, 9:292, January 2015.

[19] Sara Seabrooke, Xinping Qiu, and Bryan A Stewart. Nonmuscle Myosin II helps regulate synaptic vesicle mobility at the Drosophila neuromuscular junction. *BMC neuroscience*, 11:37, January 2010.

[20] Vivian Budnik, Michael Gorczyca, and Andreas Prokop. Selected methods for the anatomical study of Drosophila embryonic and larval neuromuscular junctions. *International review of neurobiology*, 75:323–65, January 2006.

[21] M P Sheetz, N L Baumrind, D B Wayne, and A L Pearlman. Concentration of membrane antigens by forward transport and trapping in neuronal growth cones. *Cell*, 61(2):231–41, April 1990.

[22] Steven R Wylie and Peter D Chantler. Myosin IIA drives neurite retraction. *Molecular biology of the cell*, 14(11):4654–66, November 2003.

[23] I Spector, N R Shochet, D Blasberger, and Y Kashman. Latrunculins–novel marine macrolides that disrupt microfilament organization and affect cell growth: I. Comparison with cytochalasin D. *Cell motility and the cytoskeleton*, 13(3):127–44, January 1989.

[24] J A Lunn, H Wong, E Rozengurt, and J H Walsh. Requirement of cortical actin organization for bombesin, endothelin, and EGF receptor internalization. *American journal of physiology. Cell physiology*, 279(6):C2019–27, December 2000.

[25] J A Cooper. Effects of cytochalasin and phalloidin on actin. *The Journal of cell biology*, 105(4):1473–8, October 1987.

[26] Min D Tang-Schomer, Ankur R Patel, Peter W Baas, and Douglas H Smith. Mechanical breaking of microtubules in axons during dynamic stretch injury underlies delayed elasticity, microtubule disassembly, and axon degeneration. *FASEB journal : official publication of the Federation of American Societies for Experimental Biology*, 24(5):1401–10, May 2010.

[27] Lee F Willoughby, Tanja Schlosser, Samuel A Manning, John P Parisot, Ian P Street, Helena E Richardson, Patrick O Humbert, and Anthony M Brumby. An in vivo large-scale chemical screening platform using Drosophila for anti-cancer drug discovery. *Disease models & mechanisms*, 6(2):521–9, March 2013.

[28] Raymond Wong, Lacramioara Fabian, Arthur Forer, and Julie A Brill. Phospholipase C and myosin light chain kinase inhibition define a common step in actin regulation during cytokinesis. *BMC cell biology*, 8:15, January 2007.

[29] F J Ahmad, C J Echeverri, R B Vallee, and P W Baas. Cytoplasmic dynein and dynactin are required for the transport of microtubules into the axon. *The Journal of cell biology*, 140(2):391–401, January 1998.

[30] Swati Banerjee and Manzoor A Bhat. Glial ensheathment of peripheral axons in Drosophila. *Journal of neuroscience research*, 86(6):1189–98, May 2008.

[31] F J Ahmad, J Hughey, T Wittmann, A Hyman, M Greaser, and P W Baas. Motor proteins regulate force interactions between microtubules and microfilaments in the axon. *Nature cell biology*, 2(5):276–80, May 2000.

[32] T J Dennerll, H C Joshi, V L Steel, R E Buxbaum, and S R Heidemann. Tension and compression in the cytoskeleton of PC-12 neurites. II: Quantitative measurements. *The Journal of cell biology*, 107(2):665–74, August 1988.

[33] Clifford P Brangwynne, Frederick C MacKintosh, Sanjay Kumar, Nicholas A Geisse, Jennifer Talbot, L Mahadevan, Kevin K Parker, Donald E Ingber, and David A Weitz. Microtubules can bear enhanced compressive loads in living cells because of lateral reinforcement. *The Journal of cell biology*, 173(5):733–41, June 2006.

[34] Hossein Ahmadzadeh, Douglas H Smith, and Vivek B Shenoy. Viscoelasticity of tau proteins leads to strain rate-dependent breaking of microtubules during axonal stretch injury: predictions from a mathematical model. *Biophysical journal*, 106(5):1123–33, March 2014.

[35] Douglas H Roossien, Kyle E Miller, and Gianluca Gallo. Ciliobrevins as tools for studying dynein motor function. *Frontiers in cellular neuroscience*, 9:252, January 2015.

[36] Roberto Bernal, Francisco Melo, and Pramod A Pullarkat. Drag force as a tool to test the active mechanical response of PC12 neurites. *Biophysical journal*, 98(4):515–23, February 2010.

[37] Daniel M Suter and Kyle E Miller. The emerging role of forces in axonal elongation. *Progress in neurobiology*, 94(2):91–101, July 2011.

[38] Ke Xu, Guisheng Zhong, and Xiaowei Zhuang. Actin, spectrin, and associated proteins form a periodic cytoskeletal structure in axons. *Science (New York, N.Y.)*, 339(6118):452–456, January 2013.

[39] Naomi Courtemanche, Ja Yil Lee, Thomas D Pollard, and Eric C Greene. Tension modulates actin filament polymerization mediated by formin and profilin. *Proceedings of the National Academy of Sciences of the United States of America*, 110(24):9752–7, June 2013.

[40] H Kuromi and Y Kidokoro. Two distinct pools of synaptic vesicles in single presynaptic boutons in a temperature-sensitive Drosophila mutant, shibire. *Neuron*, 20(5):917–25, May 1998.

[41] Frederick Sachs. Stretch-activated ion channels: what are they? *Physiology (Bethesda, Md.)*, 25(1):50–6, February 2010.

[42] D C van Essen. A tension-based theory of morphogenesis and compact wiring in the central nervous system. *Nature*, 385(6614):313–8, January 1997.

[43] Gang Xu, Philip V Bayly, and Larry A Taber. Residual stress in the adult mouse brain. *Biomechanics and modeling in mechanobiology*, 8(4):253–62, August 2009.

[44] Gang Xu, Andrew K Knutsen, Krikor Dikranian, Christopher D Kroenke, Philip V Bayly, and Larry A Taber. Axons pull on the brain, but tension does not drive cortical folding. *Journal of biomechanical engineering*, 132(7):071013, July 2010.

[45] B M Chen and A D Grinnell. Integrins and modulation of transmitter release from motor nerve terminals by stretch. *Science (New York, N.Y.)*, 269(5230):1578–80, September 1995.

[46] Cecilia Conde and Alfredo Cáceres. Microtubule assembly, organization and dynamics in axons and dendrites. *Nature reviews. Neuroscience*, 10(5):319–32, May 2009.

[47] N Hirokawa. Cross-linker system between neurofilaments, microtubules, and membranous organelles in frog axons revealed by the quick-freeze, deep-etching method. *The Journal of cell biology*, 94(1):129–42, July 1982.

[48] Elisa D'Este, Dirk Kamin, Fabian Göttfert, Ahmed El-Hady, and Stefan W Hell. STED nanoscopy reveals the ubiquity of subcortical cytoskeleton periodicity in living neurons. *Cell reports*, 10(8):1246–51, March 2015.

[49] Sérgio Carvalho Leite and Mónica Mendes Sousa. The neuronal and actin commitment: Why do neurons need rings? *Cytoskeleton (Hoboken, N.J.)*, 73(9):424–34, September 2016.

[50] Josta T Kevenaar and Casper C Hoogenraad. The axonal cytoskeleton: from organization to function. *Frontiers in molecular neuroscience*, 8:44, January 2015.

[51] Sérgio Carvalho Leite, Paula Sampaio, Vera Filipe Sousa, Joana Nogueira-Rodrigues, Rita Pinto-Costa, Luanne Laurel Peters, Pedro Brites, and Mónica Mendes Sousa. The Actin-Binding Protein α-Adducin Is Required for Maintaining Axon Diameter. *Cell reports*, 15(3):490–8, April 2016.

[52] Thomas D Pollard and John A Cooper. Actin, a central player in cell shape and movement. *Science (New York, N.Y.)*, 326(5957):1208–12, November 2009.

[53] Viola Vogel and Michael Sheetz. Local force and geometry sensing regulate cell functions. *Nature reviews. Molecular cell biology*, 7(4):265–75, April 2006.

[54] P Lamoureux, R E Buxbaum, and S R Heidemann. Direct evidence that growth cones pull. *Nature*, 340(6229):159–62, July 1989.

[55] Alireza Tofangchi, Anthony Fan, and M Taher A Saif. Mechanism of Axonal Contractility in Embryonic Drosophila Motor Neurons In Vivo. *Biophysical journal*, 111(7):1519–1527, October 2016.

[56] D H Smith, J A Wolf, and D F Meaney. A new strategy to produce sustained growth of central nervous system axons: continuous mechanical tension. *Tissue engineering*, 7(2):131–9, April 2001.

[57] Phillip Lamoureux, Steven R Heidemann, Nathan R Martzke, and Kyle E Miller. Growth and elongation within and along the axon. *Developmental neurobiology*, 70(3):135–49, February 2010.

[58] David E Koser, Amelia J Thompson, Sarah K Foster, Asha Dwivedy, Eva K Pillai, Graham K Sheridan, Hanno Svoboda, Matheus Viana, Luciano F Da Costa, Jochen Guck, Christine E Holt, and Kristian Franze. Mechanosensing is critical for axon growth in the developing brain. *Nature neuroscience*, 19(12):1592–1598, December 2016.

[59] Zhuo Wang, Larry Millet, Mustafa Mir, Huafeng Ding, Sakulsuk Unarunotai, John Rogers, Martha U Gillette, and Gabriel Popescu. Spatial light interference microscopy (SLIM). *Optics express*, 19(2):1016–26, January 2011.

[60] Gabriel Popescu. *Quantitative Phase Imaging of Cells and Tissues*. McGraw Hill Professional, March 2011.

[61] Gabriel Popescu, Lauren P Deflores, Joshua C Vaughan, Kamran Badizadegan, Hidenao Iwai, Ramachandra R Dasari, and Michael S Feld. Fourier phase microscopy for investigation of biological structures and dynamics. *Optics letters*, 29(21):2503–5, November 2004.

[62] C Rotsch and M Radmacher. Drug-induced changes of cytoskeletal structure and mechanics in fibroblasts: an atomic force microscopy study. *Biophysical journal*, 78(1):520–35, January 2000.

[63] Gabriel Popescu, Youngkeun Park, Niyom Lue, Catherine Best-Popescu, Lauren Deflores, Ramachandra R Dasari, Michael S Feld, and Kamran Badizadegan. Optical imaging of cell mass and growth dynamics. *American journal of physiology. Cell physiology*, 295(2):C538–44, August 2008.

[64] Agustí Brugués, Ester Anon, Vito Conte, Jim H Veldhuis, Mukund Gupta, Julien Colombelli, José J Muñoz, G Wayne Brodl, G Wayne Brodland, Benoit Ladoux, and Xavier Trepat. Forces driving epithelial wound healing. *Nature physics*, 10(9):683–690, September 2014.

[65] Laure Saias, Jim Swoger, Arturo D'Angelo, Peran Hayes, Julien Colombelli, James Sharpe, Guillaume Salbreux, and Jérôme Solon. Decrease in Cell Volume Generates Contractile Forces Driving Dorsal Closure. *Developmental cell*, 33(5):611–21, June 2015.

[66] Robert J Pelham and Fred Chang. Actin dynamics in the contractile ring during cytokinesis in fission yeast. *Nature*, 419(6902):82–6, September 2002.

[67] Mithilesh Mishra, Jun Kashiwazaki, Tomoko Takagi, Ramanujam Srinivasan, Yinyi Huang, Mohan K Balasubramanian, and Issei Mabuchi. In vitro contraction of cytokinetic ring depends on myosin II but not on actin dynamics. *Nature cell biology*, 15(7):853–9, July 2013.

[68] Guisheng Zhong, Jiang He, Ruobo Zhou, Damaris Lorenzo, Hazen P Babcock, Vann Bennett, and Xiaowei Zhuang. Developmental mechanism of the periodic membrane skeleton in axons. *eLife*, 3, December 2014.

[69] N Hirokawa, K Sobue, K Kanda, A Harada, and H Yorifuji. The cytoskeletal architecture of the presynaptic terminal and molecular structure of synapsin 1. *The Journal of cell biology*, 108(1):111–26, January 1989.

[70] Peter J Wen, Staffan Grenklo, Gianvito Arpino, Xinyu Tan, Hsien-Shun Liao, Johanna Heureaux, Shi-Yong Peng, Hsueh-Cheng Chiang, Edaeni Hamid, Wei-Dong Zhao, Wonchul Shin, Tuomas Näreoja, Emma Evergren, Yinghui Jin, Roger Karlsson, Steven N Ebert, Albert Jin, Allen P Liu, Oleg Shupliakov, and Ling-Gang Wu. Actin dynamics provides membrane tension to merge fusing vesicles into the plasma membrane. *Nature communications*, 7:12604, August 2016.

[71] K K Pfister. Cytoplasmic dynein and microtubule transport in the axon: the action connection. *Molecular neurobiology*, 20(2-3):81–91, October 1999.

[72] J Zheng, R E Buxbaum, and S R Heidemann. Investigation of microtubule assembly and organization accompanying tension-induced neurite initiation. *Journal of cell science*, 104 (Pt 4):1239–50, April 1993.

[73] Ekaterina L Grishchuk, Maxim I Molodtsov, Fazly I Ataullakhanov, and J Richard McIntosh. Force production by disassembling microtubules. *Nature*, 438(7066):384–8, November 2005.

[74] M J Gillespie and R B Stein. The relationship between axon diameter, myelin thickness and conduction velocity during atrophy of mammalian peripheral nerves. *Brain research*, 259(1):41–56, January 1983.

[75] Daniel Liewald, Robert Miller, Nikos Logothetis, Hans-Joachim Wagner, and Almut Schüz. Distribution of axon diameters in cortical white matter: an electron-microscopic study on three human brains and a macaque. *Biological cybernetics*, 108(5):541–57, October 2014.

[76] Kouhei Kamiya, Masaaki Hori, Masakazu Miyajima, Madoka Nakajima, Yuriko Suzuki, Koji Kamagata, Michimasa Suzuki, Hajime Arai, Kuni Ohtomo, and Shigeki Aoki. Axon diameter and intra-axonal volume fraction of the corticospinal tract in idiopathic normal pressure hydrocephalus measured by q-space imaging. *PloS one*, 9(8):e103842, January 2014.

[77] Philippe Marmottant and Sascha Hilgenfeldt. A bubble-driven microfluidic transport element for bioengineering. *Proceedings of the National Academy of Sciences of the United States of America*, 101(26):9523–7, June 2004.

[78] Daniel R Gossett, Westbrook M Weaver, Albert J Mach, Soojung Claire Hur, Henry Tat Kwong Tse, Wonhee Lee, Hamed Amini, and Dino Di Carlo. Label-free cell separation and sorting in microfluidic systems. *Analytical and bioanalytical chemistry*, 397(8):3249–67, August 2010.

[79] Kwanghun Chung, Yoosik Kim, Jitendra S Kanodia, Emily Gong, Stanislav Y Shvartsman, and Hang Lu. A microfluidic array for large-scale ordering and orientation of embryos. *Nature methods*, 8(2):171–6, February 2011.

[80] Pavel Neuži, Stefan Giselbrecht, Kerstin Länge, Tony Jun Huang, and Andreas Manz. Revisiting lab-on-a-chip technology for drug discovery. *Nature reviews. Drug discovery*, 11(8):620–32, August 2012.

[81] Matthew R Bennett, Wyming Lee Pang, Natalie A Ostroff, Bridget L Baumgartner, Sujata Nayak, Lev S Tsimring, and Jeff Hasty. Metabolic gene regulation in a dynamically changing environment. *Nature*, 454(7208):1119–22, August 2008.

[82] Matthew M Crane, Jeffrey N Stirman, Chan-Yen Ou, Peri T Kurshan, James M Rehg, Kang Shen, and Hang Lu. Autonomous screening of C. elegans identifies genes implicated in synaptogenesis. *Nature methods*, 9(10):977–80, October 2012.

[83] Sunitha Nagrath, Lecia V Sequist, Shyamala Maheswaran, Daphne W Bell, Daniel Irimia, Lindsey Ulkus, Matthew R Smith, Eunice L Kwak, Subba Digumarthy, Alona Muzikansky, Paula Ryan, Ulysses J Balis, Ronald G Tompkins, Daniel A Haber, and Mehmet Toner. Isolation of rare circulating tumour cells in cancer patients by microchip technology. *Nature*, 450(7173):1235–9, December 2007.

[84] Axel Hochstetter, Eric Stellamanns, Siddharth Deshpande, Sravanti Uppaluri, Markus Engstler, and Thomas Pfohl. Microfluidics-based single cell analysis reveals drug-dependent motility changes in trypanosomes. *Lab on a chip*, 15(8):1961–8, April 2015.

[85] S Takayama, E Ostuni, P LeDuc, K Naruse, D E Ingber, and G M Whitesides. Subcellular positioning of small molecules. *Nature*, 411(6841):1016, June 2001.

[86] Elena M Lucchetta, Ji Hwan Lee, Lydia A Fu, Nipam H Patel, and Rustem F Ismagilov. Dynamics of Drosophila embryonic patterning network perturbed in space and time using microfluidics. *Nature*, 434(7037):1134–8, April 2005.

[87] Gregory J Gage, Daryl R Kipke, and William Shain. Whole animal perfusion fixation for rodents. *Journal of visualized experiments : JoVE*, (65):1–9, July 2012.

[88] David Dahlgren, Carl Roos, Erik Sjögren, and Hans Lennernäs. Direct In Vivo Human Intestinal Permeability (Peff) Determined with Different Clinical Perfusion and Intubation Methods. *Journal of pharmaceutical sciences*, 104(9):2702–26, September 2015.

[89] Bernard J Slater, Anthony Y Fan, Kevin A Stebbings, M Taher A Saif, and Daniel A Llano. Modification of a Colliculo-thalamocortical Mouse Brain Slice, Incorporating 3-D printing of Chamber Components and Multi-scale Optical Imaging. *Journal of visualized experiments : JoVE*, (103), January 2015.

[90] D C Duffy, J C McDonald, O J Schueller, and G M Whitesides. Rapid Prototyping of Microfluidic Systems in Poly(dimethylsiloxane). *Analytical chemistry*, 70(23):4974–84, December 1998.

[91] Chang Lu and Scott S. Verbridge. *Microfluidic Methods for Molecular Biology.* Springer, May 2016.

[92] S Takayama, J C McDonald, E Ostuni, M N Liang, P J Kenis, R F Ismagilov, and G M Whitesides. Patterning cells and their environments using multiple laminar fluid flows in capillary networks. *Proceedings of the National Academy of Sciences of the United States of America*, 96(10):5545–8, May 1999.

[93] Zhiqiang Li, Ying Zhang, Philip R LeDuc, and Kelvin B Gregory. Microbial electricity generation via microfluidic flow control. *Biotechnology and bioengineering*, 108(9):2061–9, September 2011.

[94] S G Knoll, W W Ahmed, and T A Saif. Contractile dynamics change before morphological cues during fluorescence [corrected] illumination. *Scientific reports*, 5:18513, December 2015.

[95] Jun Shintake, Samuel Rosset, Bryan Schubert, Dario Floreano, and Herbert Shea. Versatile Soft Grippers with Intrinsic Electroadhesion Based on Multifunctional Polymer Actuators. *Advanced materials (Deerfield Beach, Fla.)*, 28(2):231–8, January 2016.

[96] Aarash Sofla, Erkin Seker, James P. Landers, and Matthew R. Begley. PDMS-Glass Interface Adhesion Energy Determined Via Comprehensive Solutions for Thin Film Bulge/Blister Tests. *Journal Of Applied Mechanics-Transactions Of The Asme*, 77(3):ARTN 031007, May 2010.

[97] Anthony Fan, Alireza Tofangchi, Mikhail Kandel, Gabriel Popescu, and Taher Saif. Coupled circumferential and axial tension driven by actin and myosin influences in vivo axon diameter. *Scientific reports*, 7(1):14188, October 2017.

[98] Benjamin F Fosque, Yi Sun, Hod Dana, Chao-Tsung Yang, Tomoko Ohyama, Michael R Tadross, Ronak Patel, Marta Zlatic, Douglas S Kim, Misha B Ahrens, Vivek Jayaraman, Loren L Looger, and Eric R Schreiter. Neural circuits. Labeling of active neural circuits in vivo with designed calcium integrators. *Science (New York, N.Y.)*, 347(6223):755–60, February 2015.

[99] A Aubry, C Batini, J M Billard, R T Kado, and P Morain. Tetrodotoxin induced calcium spikes: in vitro and in vivo studies of normal and deafferented Purkinje cells. *Experimental brain research*, 84(2):297–302, January 1991.

[100] Lei Jin, Zhou Han, Jelena Platisa, Julian R A Wooltorton, Lawrence B Cohen, and Vincent A Pieribone. Single action potentials and subthreshold electrical events imaged in neurons with a fluorescent protein voltage probe. *Neuron*, 75(5):779–85, September 2012.

[101] Guan Cao, Jelena Platisa, Vincent A Pieribone, Davide Raccuglia, Michael Kunst, and Michael N Nitabach. Genetically targeted optical electrophysiology in intact neural circuits. *Cell*, 154(4):904–13, August 2013.

[102] A R Freeman. Electrophysiological activity of tetrodotoxin on the resting membrane of the squid giant axon. *Comparative biochemistry and physiology. A, Comparative physiology*, 40(1):71–82, September 1971.

[103] D C Chang and J Liu. A comparative study of the effects of tetrodotoxin and the removal of external Na+ on the resting potential: evidence of separate pathways for the resting and excitable Na currents in squid axon. *Cellular and molecular neurobiology*, 5(4):311–20, December 1985.

[104] Costantino Creton and Matteo Ciccotti. Fracture and adhesion of soft materials: a review. *Reports on progress in physics. Physical Society (Great Britain)*, 79(4):046601, April 2016.

[105] JG Williams. Energy release rates for the peeling of flexible membranes and the analysis of blister tests. *International Journal Of Fracture*, 87(3):265–288, 1997.

[106] Qiming Wang and Xuanhe Zhao. Phase Diagrams of Instabilities in Compressed Film-Substrate Systems. *Journal Of Applied Mechanics-Transactions Of The Asme*, 81(5):ARTN 051004, May 2014.

[107] JW HUTCHINSON and Z SUO. Mixed-Mode Cracking In Layered Materials. *Advances In Applied Mechanics, Vol 29*, 29:63–191, 1992.

[108] L. B. Freund and S. Suresh. *Thin Film Materials*. Cambridge University Press, January 2004.

[109] Steven P Koenig, Narasimha G Boddeti, Martin L Dunn, and J Scott Bunch. Ultrastrong adhesion of graphene membranes. *Nature nanotechnology*, 6(9):543–6, August 2011.

[110] Z. Cao, P. Wang, W. Gao, L. Tao, J. W. Suk, R. S. Ruoff, D. Akinwande, R. Huang, and K. M. Liechti. A blister test for interfacial adhesion of large-scale transferred graphene. *Carbon*, 69:390–400, April 2014.

[111] Zong Zong, Chia-Ling Chen, Mehmet R. Dokmeci, and Kai-tak Wan. Direct measurement of graphene adhesion on silicon surface by intercalation of nanoparticles. *Journal Of Applied Physics*, 107(2):ARTN 026104, 2010.

[112] JA HINKLEY. A Blister Test For Adhesion Of Polymer-Films To Sio2. *Journal Of Adhesion*, 16(2):115–125, 1983.

[113] P. Davies, L. Sohier, J. Y. Cognard, A. Bourmaud, D. Choqueuse, E. Rinnert, and R. Creac'hcadec. Influence of adhesive bond line thickness on joint strength. *International Journal Of Adhesion And Adhesives*, 29(7):724–736, October 2009.

[114] Anthony Fan, Alireza Tofangchi, Matthew de Venecia, and Taher Saif. A simple microfluidic platform for the partial treatment of insuspendable tissue samples with orientation control. *Lab on a chip*, 18(5):735–742, February 2018.

[115] Richard Budynas, Warren Young, and Ali Sadegh. *Roark's Formulas for Stress and Strain, 8th Edition*. McGraw-Hill Education, December 2011.

[116] KT WAN, RG HORN, S COURMONT, and BR LAWN. Pressurized Internal Lenticular Cracks At Healed Mica Interfaces. *Journal Of Materials Research*, 8(5):1128–1136, May 1993.

[117] C. M. Wang, J. N. Reddy, and K. H. Lee. *Shear Deformable Beams and Plates*. Elsevier, July 2000.

[118] CY Hui, A Jagota, SJ Bennison, and JD Londono. Crack blunting and the strength of soft elastic solids. *Proceedings Of The Royal Society A-Mathematical Physical And Engineering Sciences*, 459(2034):1489–1516, 2003.

[119] Haibing Zhang. The Permeability Characteristics of Silicone Rubber. *SAMPE Fall Technical Conference*, January 2006.

[120] Thomas C Sudhof. The synaptic vesicle cycle. *Annual review of neuroscience*, 27:509–47, January 2004.

[121] Silvio O Rizzoli and William J Betz. Synaptic vesicle pools. *Nature reviews. Neuroscience*, 6(1):57–69, January 2005.

[122] L Li, L S Chin, O Shupliakov, L Brodin, T S Sihra, O Hvalby, V Jensen, D Zheng, J O McNamara, and P Greengard. Impairment of synaptic vesicle clustering and of synaptic transmission, and increased seizure propensity, in synapsin I-deficient mice. *Proceedings of the National Academy of Sciences of the United States of America*, 92(20):9235–9, September 1995.

[123] D M Landis, A K Hall, L A Weinstein, and T S Reese. The organization of cytoplasm at the presynaptic active zone of a central nervous system synapse. *Neuron*, 1(3):201–9, May 1988.

[124] Giuliana Fusco, Tillmann Pape, Amberley D Stephens, Pierre Mahou, Ana Rita Costa, Clemens F Kaminski, Gabriele S Kaminski Schierle, Michele Vendruscolo, Gianluigi Veglia, Christopher M Dobson, and Alfonso de Simone. Structural basis of synaptic vesicle assembly promoted by α-synuclein. *Nature communications*, 7:12563, September 2016.

[125] Åsa M E Winther, Olga Vorontsova, Kathryn A Rees, Tuomas Näreoja, Elena Sopova, Wei Jiao, and Oleg Shupliakov. An Endocytic Scaffolding Protein together with Synapsin Regulates Synaptic Vesicle Clustering in the Drosophila Neuromuscular Junction. *The Journal of neuroscience : the official journal of the Society for Neuroscience*, 35(44):14756–70, November 2015.

[126] Paula Nunes, Nicola Haines, Venkat Kuppuswamy, David J Fleet, and Bryan A Stewart. Synaptic vesicle mobility and presynaptic F-actin are disrupted in a N-ethylmaleimide-sensitive factor allele of Drosophila. *Molecular biology of the cell*, 17(11):4709–19, November 2006.

[127] M Morales, M A Colicos, and Y Goda. Actin-dependent regulation of neurotransmitter release at central synapses. *Neuron*, 27(3):539–50, September 2000.

[128] Christian Dillon and Yukiko Goda. The actin cytoskeleton: integrating form and function at the synapse. *Annual review of neuroscience*, 28:25–55, January 2005.

[129] F Benfenati, F Valtorta, E Chieregatti, and P Greengard. Interaction of free and synaptic vesicle-bound synapsin I with F-actin. *Neuron*, 8(2):377–86, February 1992.

[130] J C Cole, B R Villa, and R S Wilkinson. Disruption of actin impedes transmitter release in snake motor terminals. *The Journal of physiology*, 525 Pt 3:579–86, June 2000.

[131] Menglong Rui, Jinjun Qian, Lijuan Liu, Yihan Cai, Huihui Lv, Junhai Han, Zhengping Jia, and Wei Xie. The neuronal protein Neurexin directly interacts with the Scribble-Pix complex to stimulate F-actin assembly for synaptic vesicle clustering. *Journal Of Biological Chemistry*, 292(35):14334–14348, 2017.

[132] Cho-yin Lee, Jizhong Lou, Kuo-kuang Wen, Melissa McKane, Suzanne G Eskin, Shoichiro Ono, Shu Chien, Peter A Rubenstein, Cheng Zhu, and Larry V McIntire. Actin depolymerization under force is governed by lysine 113:glutamic acid 195-mediated catch-slip bonds. *Proceedings of the National Academy of Sciences of the United States of America*, 110(13):5022–7, March 2013.

[133] Derek L Huang, Nicolas A Bax, Craig D Buckley, William I Weis, and Alexander R Dunn. Vinculin forms a directionally asymmetric catch bond with F-actin. *Science (New York, N.Y.)*, 357(6352):703–706, August 2017.

[134] Lorenzo A Cingolani and Yukiko Goda. Actin in action: the interplay between the actin cytoskeleton and synaptic efficacy. *Nature reviews. Neuroscience*, 9(5):344–56, May 2008.

[135] William J Tyler. The mechanobiology of brain function. *Nature reviews. Neuroscience*, 13(12):867–78, December 2012.

[136] Stephen L Berger, Alejandra Leo-Macias, Stephanie Yuen, Latika Khatri, Sylvia Pfennig, Yanqing Zhang, Esperanza Agullo-Pascual, Ghislaine Caillol, Min-Sheng Zhu, Eli Rothenberg, Carmen V Melendez-Vasquez, Mario Delmar, Christophe Leterrier, and James L Salzer. Localized Myosin II Activity Regulates Assembly and Plasticity of the Axon Initial Segment. *Neuron*, 97(3):555–570.e6, February 2018.

[137] Neil Billington, Aibing Wang, Jian Mao, Robert S Adelstein, and James R Sellers. Characterization of three full-length human nonmuscle myosin II paralogs. *The Journal of biological chemistry*, 288(46):33398–410, November 2013.

[138] Jordan R Beach, Lin Shao, Kirsten Remmert, Dong Li, Eric Betzig, and John A Hammer 3rd. Non-muscle myosin II isoforms coassemble in living cells. *Current biology : CB*, 24(10):1160–6, May 2014.

[139] Yingpei He, Yuan Ren, Bingbing Wu, Boris Decourt, Aih Cheun Lee, Aaron Taylor, and Daniel M Suter. Src and cortactin promote lamellipodia protrusion and filopodia formation and stability in growth cones. *Molecular biology of the cell*, 26(18):3229–44, September 2015.

[140] Sethuraman Sankaranarayanan, Pradeep P Atluri, and Timothy A Ryan. Actin has a molecular scaffolding, not propulsive, role in presynaptic function. *Nature neuroscience*, 6(2):127–35, February 2003.

[141] Mark Mayford, Steven A Siegelbaum, Eric R K, and Eric R Kandel. Synapses and memory storage. *Cold Spring Harbor perspectives in biology*, 4(6), June 2012.

[142] Harold L Atwood and Shanker Karunanithi. Diversification of synaptic strength: presynaptic elements. *Nature reviews. Neuroscience*, 3(7):497–516, July 2002.

[143] Robert C Malenka and Mark F Bear. LTP and LTD: an embarrassment of riches. *Neuron*, 44(1):5–21, September 2004.

[144] H Kuromi and Y Kidokoro. Tetanic stimulation recruits vesicles from reserve pool via a cAMP-mediated process in Drosophila synapses. *Neuron*, 27(1):133–43, July 2000.

[145] S S Zakharenko, L Zablow, and S A Siegelbaum. Visualization of changes in presynaptic function during long-term synaptic plasticity. *Nature neuroscience*, 4(7):711–7, July 2001.

[146] Ildar T Bayazitov, Robert J Richardson, Robert G Fricke, and Stanislav S Zakharenko. Slow presynaptic and fast postsynaptic components of compound long-term potentiation. *The Journal of neuroscience : the official journal of the Society for Neuroscience*, 27(43):11510–21, October 2007.

[147] T W Rosahl, M Geppert, D Spillane, J Herz, R E Hammer, R C Malenka, and T C Südhof. Short-term synaptic plasticity is altered in mice lacking synapsin I. *Cell*, 75(4):661–70, November 1993.

[148] V A Pieribone, O Shupliakov, L Brodin, S Hilfiker-Rothenfluh, A J Czernik, and P Greengard. Distinct pools of synaptic vesicles in neurotransmitter release. *Nature*, 375(6531):493–7, June 1995.

[149] Daniel Gitler, Yoshiko Takagishi, Jian Feng, Yong Ren, Ramona M Rodriguiz, William C Wetsel, Paul Greengard, and George J Augustine. Different presynaptic roles of synapsins at excitatory and inhibitory synapses. *The Journal of neuroscience : the official journal of the Society for Neuroscience*, 24(50):11368–80, December 2004.

[150] T C Südhof. The structure of the human synapsin I gene and protein. *The Journal of biological chemistry*, 265(14):7849–52, May 1990.

[151] W Schiebler, R Jahn, J P Doucet, J Rothlein, and P Greengard. Characterization of synapsin I binding to small synaptic vesicles. *The Journal of biological chemistry*, 261(18):8383–90, June 1986.

[152] M Bähler and P Greengard. Synapsin I bundles F-actin in a phosphorylation-dependent manner. *Nature*, 326(6114):704–7, April 1987.

[153] P E Ceccaldi, F Grohovaz, F Benfenati, E Chieregatti, P Greengard, and F Valtorta. Dephosphorylated synapsin I anchors synaptic vesicles to actin cytoskeleton: an analysis by videomicroscopy. *The Journal of cell biology*, 128(5):905–12, March 1995.

[154] Ona Bloom, Emma Evergren, Nikolay Tomilin, Ole Kjaerulff, Peter Löw, Lennart Brodin, Vincent A Pieribone, Paul Greengard, and Oleg Shupliakov. Colocalization of synapsin and actin during synaptic vesicle recycling. *The Journal of cell biology*, 161(4):737–47, May 2003.

[155] Michitoshi Watanabe, Kazushige Nomura, Akihiro Ohyama, Ryoki Ishikawa, Yoshiaki Komiya, Kohei Hosaka, Emiko Yamauchi, Hisaaki Taniguchi, Nobuyuki Sasakawa, Konosuke Kumakura, Tatsuo Ushiki, Osamu Sato, Mitsuo Ikebe, and Michihiro Igarashi. Myosin-Va regulates exocytosis through the submicromolar Ca2+-dependent binding of syntaxin-1A. *Molecular biology of the cell*, 16(10):4519–30, October 2005.

[156] Hiroko Yano, Ipe Ninan, Hong Zhang, Teresa A Milner, Ottavio Arancio, and Moses V Chao. BDNF-mediated neurotransmission relies upon a myosin VI motor complex. *Nature neuroscience*, 9(8):1009–18, August 2006.

[157] Michael A Gaffield, Silvio O Rizzoli, and William J Betz. Mobility of synaptic vesicles in different pools in resting and stimulated frog motor nerve terminals. *Neuron*, 51(3):317–25, August 2006.

[158] Michael A Gaffield and William J Betz. Synaptic vesicle mobility in mouse motor nerve terminals with and without synapsin. *The Journal of neuroscience : the official journal of the Society for Neuroscience*, 27(50):13691–700, December 2007.

[159] Arndt Pechstein and Oleg Shupliakov. Taking a back seat: synaptic vesicle clustering in presynaptic terminals. *Frontiers in synaptic neuroscience*, 2:143, January 2010.

[160] Simen G Owe, Vidar Jensen, Emma Evergren, Arnaud Ruiz, Oleg Shupliakov, Dimitri M Kullmann, Jon Storm-Mathisen, S Ivar Walaas, Øivind Hvalby, and Linda H Bergersen. Synapsin- and actin-dependent frequency enhancement in mouse hippocampal mossy fiber synapses. *Cerebral cortex (New York, N.Y. : 1991)*, 19(3):511–23, March 2009.

[161] Oliver Kann and Richard Kovács. Mitochondria and neuronal activity. *American journal of physiology. Cell physiology*, 292(2):C641–57, February 2007.

[162] Roberto Bernal, Pramod A Pullarkat, and Francisco Melo. Mechanical properties of axons. *Physical review letters*, 99(1):018301, July 2007.

[163] L D Landau and E. M. Lifshitz. *Fluid Mechanics*. Elsevier, October 2013.